ENVIRONMENTAL ANALYSIS AT THE NANOSCALE: FROM SENSOR DEVELOPMENT TO FULL SCALE DATA PROCESSING

Marjorie R. Willner

Dissertation Submitted to the faculty of the Virginia Polytechnic Institute and State University in partial fulfillment of the requirements for the degree of

Doctor of Philosophy in Civil Engineering

Peter J. Vikesland, Chair

Linsey C. Marr

Amy Pruden

Michele Zagnoni

March 14th, 2018

Blacksburg, VA

Keywords: Surface-enhanced Raman spectroscopy, Microfluidics, Raman spectroscopy, Plasmonics

Abstract (academic)

Environmental Analysis at the Nanoscale: From Sensor Development to Full Scale Data Processing

Marjorie R. Willner

Raman spectroscopy is an extremely versatile technique with molecular sensitivity and fingerprint specificity. However, the translation of this tool into a deployable technology has been stymied by the irreproducibility of sample preparation and the lack of complex data analysis tools. In this dissertation, a droplet microfluidic platform was prototyped to address both sample-to-sample variation and to introduce a level of quantitation to surface enhanced Raman spectroscopy (SERS). Shifting the SERS workflow from a cell-to-cell mapping routine to the mapping of tens to hundreds of cells demands the development of an automated processing tool to perform basic SERS analyses such as baseline correction, peak feature selection, and SERS map generation. The prototype analysis tool was subsequently expanded for use with a multitude of diverse SERS applications. Specifically, a two-dimensional SERS assay for the detection of sialic acid residues on the cell membrane was translated into a live cell assay by utilizing a droplet microfluidic device. Combining single-cell encapsulation with a chamber array to hold and immobilize droplets allowed for the interrogation of hundreds of droplets. Our novel application of computer vision algorithms to SERS maps revealed that sialic sugars on cancer cell membranes are found in small clusters, or islands, and that these islands typically occupy less than 30% of the cell surface area. Employing an opportunistic mindset for the application of the data processing platform, a number of smaller projects were pursued. Biodegradable aliphatic-aromatic copolyesters of varying aromatic content were characterized using Raman spectroscopy and principal component analysis (PCA). The six different samples could successfully be distinguished from one another and the tool was able to identify spectral feature changes resulting from an increasing number of aryl esters.

Uniquely, PCA was performed on the 3,125 spectra collected from each sample to investigate point-to-point heterogeneities. A third set of projects evaluated the ability of the data processing tool to calculate spectral ratios in an automated fashion and were exploited for use with nano-pH probes and Rayleigh hot-spot normalization.

Abstract (general audience)

Environmental Analysis at the Nanoscale: From Sensor Development to Full Scale Data Processing

Marjorie R. Willner

How can we understand the dynamic behavior of the cell membrane? Do certain polymeric structures in biodegradable plastic favor bacterial growth and subsequent degradation? To answer these and other intriguing scientific questions, techniques and technologies must be borrowed from a diverse array of fields and combined with fundamental understanding to create innovative solutions. In this dissertation, a two-dimensional surface enhanced Raman spectroscopy (SERS) assay was translated into a live cell assay by utilizing a droplet microfluidic device. Combining single-cell encapsulation with a chamber array to hold and immobilize droplets allowed for the interrogation of hundreds of droplets. Shifting the SERS workflow from a manual cell-to-cell mapping routine to the mapping of tens to hundreds of cells demanded the development of an automated processing tool to perform basic SERS analyses such as baseline correction, peak feature selection, and SERS map generation. Our novel application of computer vision algorithms to SERS maps was able to reveal that sialic sugars on cancer cell membranes are found in small clusters, or islands, and that these islands typically occupy less than 30% of the cell surface area. With an opportunistic mindset, several smaller projects that combine Raman and SERS with extensive data analysis were also pursued. Biodegradable plastics of varying content were studied with Raman spectroscopy. The aliphatic and aromatic polymeric units within these plastics both contain esters, but it is hypothesized that enzymatic hydrolysis occurs at the units asymmetrically. For each of six different samples, five maps were collected, processed using the analysis tool, and then analyzed using a multivariate analysis toolbox. Principal component analysis (PCA) was used to distinguish the polymers and to identify spectral feature changes resulting from an increasing

number of aryl esters. Uniquely, PCA was performed on the 3,125 spectra collected from each sample to investigate point-to-point heterogeneities. A third set of projects evaluated the ability of the data processing tool to calculate spectral ratios in an automated fashion and it was exploited for use with nano-pH probes and Rayleigh hot-spot normalization

Acknowledgements

First, I would like to thank my advisor, Dr. Peter J. Vikesland, for his support and encouragement over the last 5.25 years. He has provided me with countless opportunities to grow as a scientist and a person and his mentorship throughout these experiences has been invaluable. Pete's unwavering patience and positivity have helped me get through some trying times with my research and I feel honored to be a member of his group.

I would like to thank my committee members, Dr. Marr, Dr. Pruden and Dr. Zagnoni for their insights and contributions throughout this process. I would especially like to thank Michele for hosting me in his laboratory and teaching me about microfluidics and image processing. For my time in Scotland, I must also thank Dr. Duncan Graham, whose crazy, fun and rambunctious lab kept both day-to-day lab work and many conferences entertaining.

A big thank you goes out to my labmates past and present! Dr. Weinan Leng's help with instrumentation, nanoparticle synthesis and everything else was fundamental to the success of my research. Thanks to Dr. Kay McMillian for teaching me everything about microfluidics. Thank you to Dr. Haoran Wei for allowing me to contribute to exciting SERS experiments.

I would like to thank my Mom, Dad and Sister! I could not have made it to this point without their continued support! I am glad they could share in all the highs and lows of this adventure. Finally, thank you to my girlfriend, Yen, who motivates me to continually strive to be the best version of me.

Table of Contents

Table of Figures

List of Tables

List of Equations

Chapter 1 Introduction

1.1 Introduction

Water and water technology have fascinated individuals for millennia with Vitruvius providing one of the first written accounts of civil engineering in his 1st century BC treatise, *De Architectura*. In addition to his description of the surveying and construction of the Roman aqueducts[1], one whole section, 8.3, is dedicated to "Of the Nature of Various Waters" and "Of the Qualities of Waters in Certain Places." In our modern era we are acutely aware of the importance of water quality, with approximately 35% of the global population lacking access to improved sanitation[2] and no guarantees that improved water sources are not inadvertently poisoning us (e.g., Flint Water Crisis[3, 4]). A cornucopia of actions are required to address this growing water burden, with the development of rapid sensors for contaminant detection being just one of the many avenues of research that needs to be pursued.

Nanotechnology enabled sensors hold major promise as low-cost, easy-to-use, point-of-care, sensors for contaminant detection. One of the major drivers behind the application of nanotechnology for the detection of molecules, such as pesticides, or pathogens, (e.g., Methicillin-resistant *Staphylococcus aureus* or MRSA), is that nanoprobes are on the same size scale as these analytes of interest. Unlike previous detection techniques that were focused on groping for a needle in a haystack, nanotechnology allows for the development of needle-sized highly specific probes. The term nanotechnology describes a broad range of materials and applications, but plasmonic nanoparticles, especially gold nanoparticle (AuNP), have been a major focus of nanosensor development because upon aggregation the colloidal suspension changes color. Nanosensors, described in **Chapter 2**, typically utilize one of three main transduction methods, but visible observable color changes often serve as the simplest mode of communication. However, there are many applications where nanotechnology is used to answer more complex questions than if an analyte of interest is present in a solution and in these cases, nanotechnology is often combined with instrumentation to track this more complex behavior.

Raman Spectroscopy is powerful molecular fingerprinting technique that allows for the identification of various chemical motifs and their local binding environments and the method has been used extensively for contaminant detection. A benefit of using Raman spectroscopy for environmental samples is that there is no signature from water because the method is based on the polarizability of the molecule. In Raman spectroscopy, a monochromatic laser is used to excite a sample and only the photons that are inelastically (Raman) scattered are collected. The difference in energy between the excitation laser and the wavelength of the scattered photons is called the Raman shift or wavenumber and is denoted in units of cm^{-1}. Raman spectroscopy is used extensively with plasmonic nanoparticles because it allows for rapid (minutes), non-destructive interrogation of samples. Moreover, the introduction of nanoparticles can enhance the inherent Raman scattering by up to 10^9 with the best enhancement arising from small gaps between adjacent nanoparticles, or hotspots[5]. In this dissertation both Raman spectroscopy and nanomaterial-enabled Raman spectroscopy, known as surface enhanced Raman spectroscopy (SERS), were used to explore questions of environmental relevance.

In **Chapter 3**, Raman spectroscopy was used to characterize a suite of biodegradable aromatic-aliphatic polymers. The accumulation of persistent polymers in aqueous and terrestrial systems is increasingly recognized as a major environmental threat[6-8]. One strategy to mitigate further accumulation is to embrace the use of biodegradable polymers, many of which are already commercially available. Numerous end-of-life options exist for biodegradable polyesters ranging from composting and depolymerization for monomer recycling to biodegradation in the soil following agricultural application. In many cases, the hydrolysis of ester bonds in the polyester is considered to be the rate-limiting step in the overall biodegradation process[9]. However, the specific mechanisms and locations of hydrolysis remain an area of active research because both polymeric units, the aromatic and aliphatic mers, contain ester bonds and the polymer is not ordered, e.g., there are a multitude of combinations of the units. Using Raman spectroscopy it is possible to monitor diversification in the ester bonds because the polarization, and thus the Raman shift, of bonds changes depending on the local molecular structure.

In **Chapter 4**, SERS was used synergistically with microfluidics to create a platform for single-cell analysis. The development of this optofluidic platform is part of a new nanosensor paradigm, where detailed detection is deployed with a comprehensive sample preparation platform. Single-cell screening has extensive potential applications in environmental monitoring, where the emergence of antibiotic resistant bacteria has led to questions about how environmental stress leads to phenotypic variation in a homogenous genotypic population. The novel integration of SERS, microfluidics, and computer vision analysis was prototyped using prostate cancer cells (PC3) because PC3 cells are well defined and are an order of magnitude larger in size than bacteria. The now functioning platform is currently being translated for use for bacteria detection.

The appendices contain two works related to the development of SERS nano-pH probes to study the pH inside aerosols and in confined spaces. Appendix A discusses the initial development of the probes and their use to measure the intracellular pH of PC3 cells. For this work the data processing tool described in **Chapter 4** was expanded to automatically calculate the ratio between a pH sensitive and a pH intensive Raman peak to ultimately render pH maps. As in **Chapter 4**, statistical analysis was performed on the dataset to draw conclusions, such as the distribution of intracellular pH values matched those reported in the literature. Appendix B contains the application of the nano-pH probes to determine the pH inside aerosol droplets. In this work, the data processing tool was utilized to rapidly determine the pH distribution in over 33 individual droplets. It was found that there is a stable pH gradient in the droplets and that the pH in the core of a droplet is higher than that of bulk water by up to 3.6 pH units.

1.2 Attribution

Marjorie R. Willner, Department of Civil and Environmental Engineering, Virginia Tech

Primary author of this dissertation

Peter J. Vikesland, Ph.D., Professor of Civil and Environmental Engineering, Virginia Tech

Principal Investigator and coauthor of Chapters 2- 4 and Appendix A & B

Michael Sander, Ph.D., Institute of Biogeochemistry and Pollutant Dynamics, ETH Zurich

Coauthor of Chapter 3

Kristopher McNeill, Ph.D., Institute of Biogeochemistry and Pollutant Dynamics, ETH Zurich

Coauthor of Chapter 3

Michael Thomas Zumstein, Ph.D., Institute of Biogeochemistry and Pollutant Dynamics, ETH Zurich

Coauthor of Chapter 3

Michele Zagnoni, Ph.D., Senior Lecturer, Centre for Microsystems and Photonics, Dept. Electronic & Electrical Engineering, University of Strathclyde

Coauthor of Chapter 4

Duncan Graham, Ph.D., Professor, Centre for Molecular Nanometrology, Department of Pure and Applied Chemistry, WestCHEM, University of Strathclyde, Glasgow

Coauthor of Chapter 4

Kay McMillian, Ph.D, Centre for Microsystems and Photonics, Dept. Electronic & Electrical Engineering, University of Strathclyde

Coauthor of Chapter 4

Linsey C. Marr, Ph.D., Professor of Civil and Environmental Engineering, Virginia Tech

Coauthor of Appendix A & B

Haoran Wei, Ph.D., Department of Civil and Environmental Engineering, Virginia Tech

Coauthor of Appendix A & B

Weinan Leng, Ph.D., Department of Civil and Environmental Engineering, Virginia Tech

Coauthor of Appendix B

Eric Vejerano, Ph.D., Professor of Public Health, University of South Carolina

Coauthor of Appendix B

Qishen Huang, Department of Civil and Environmental Engineering, Virginia Tech

Coauthor of Appendix B

1.3 References

1. Rowland, I. D.; Howe, T. N., *Vitruvius:'Ten Books on Architecture'*. Cambridge University Press: 2001.
2. Pruss-Ustun, A.; Organization, W. H., Safer water, better health: costs, benefits and sustainability of interventions to protect and promote health. **2008**.
3. Bellinger, D. C., Lead Contamination in Flint — An Abject Failure to Protect Public Health. *New England Journal of Medicine* **2016,** *374*, (12), 1101-1103.
4. Hanna-Attisha, M.; LaChance, J.; Sadler, R. C.; Schnepp, A. C., Elevated Blood Lead Levels in Children Associated With the Flint Drinking Water Crisis: A Spatial Analysis of Risk and Public Health Response. *American Journal of Public Health* **2016,** *106*, (2), 283-290.
5. Lim, D.-K.; Jeon, K.-S.; Hwang, J.-H.; Kim, H.; Kwon, S.; Suh, Y. D.; Nam, J.-M., Highly uniform and reproducible surface-enhanced Raman scattering from DNA-tailorable nanoparticles with 1-nm interior gap. *Nature Nanotechnology* **2011,** *6*, 452.
6. Rillig, M. C., Microplastic in Terrestrial Ecosystems and the Soil? *Environmental science & technology* **2012,** *46*, (12), 6453-6454.
7. Browne, M. A.; Crump, P.; Niven, S. J.; Teuten, E.; Tonkin, A.; Galloway, T.; Thompson, R., Accumulation of Microplastic on Shorelines Woldwide: Sources and Sinks. *Environmental science & technology* **2011,** *45*, (21), 9175-9179.
8. Thompson, R. C.; Olsen, Y.; Mitchell, R. P.; Davis, A.; Rowland, S. J.; John, A. W. G.; McGonigle, D.; Russell, A. E., Lost at Sea: Where Is All the Plastic? *Science* **2004,** *304*, (5672), 838-838.
9. Mueller, R.-J., Biological degradation of synthetic polyesters—Enzymes as potential catalysts for polyester recycling. *Process Biochemistry* **2006,** *41*, (10), 2124-2128.

Chapter 2 Nanomaterial Enabled Sensors for Environmental Contaminants

(This chapter will be submitted as an invited nanosensor review to the *Journal of Nanobiotechnology*)

2.1 Abstract

The need and desire to understand the environment, especially the quality of one's local water and air, has continued to expand with the emergence of the digital age. The bottleneck in understanding the environment has switched from being able to store all of the data collected to collecting enough data on a broad range of contaminants. Nanomaterial enabled sensors represent a suite of technologies developed over the last ten years for the highly specific and sensitive detection of environmental contaminants. Moreover, the development of nanomaterial enabled sensors promises the introduction of cheap and easy-to-use sensors that are integrated with emerging digital technologies. In this review, we provide an introduction to nanosensor design and then highlight key findings from the literature with respect to key contaminants of interest: heavy metals, pesticides, and pathogens.

2.2 Introduction

Nanomaterial enabled sensors are an exciting emerging technology that enable nanomolar to sub-picomolar detection of environmental contaminants [2-6]. Interest in these sensors stems from their potential for facile, in-field contaminant detection without the need for expensive lab equipment. Many past reviews in this area have grouped sensors based on the signal transduction method[3-6], nanoparticle backbone [10-13], or contaminant class [2, 14, 15], thus leaving one important paradigm virtually untouched: classifying sensors based on the analyte(s) of interest. Because environmental scientists and engineers are often interested in determining if a specific contaminant exists at a field site and if its concentration is above the regulatory limit, there was a need to organize a review based upon the detection of specific contaminants. This review has been developed to address these concerns. First, we summarize

the general concepts underlying a nano-enabled sensor and then discuss recent developments in nanomaterial enabled detection of metals, pesticides, and pathogens.

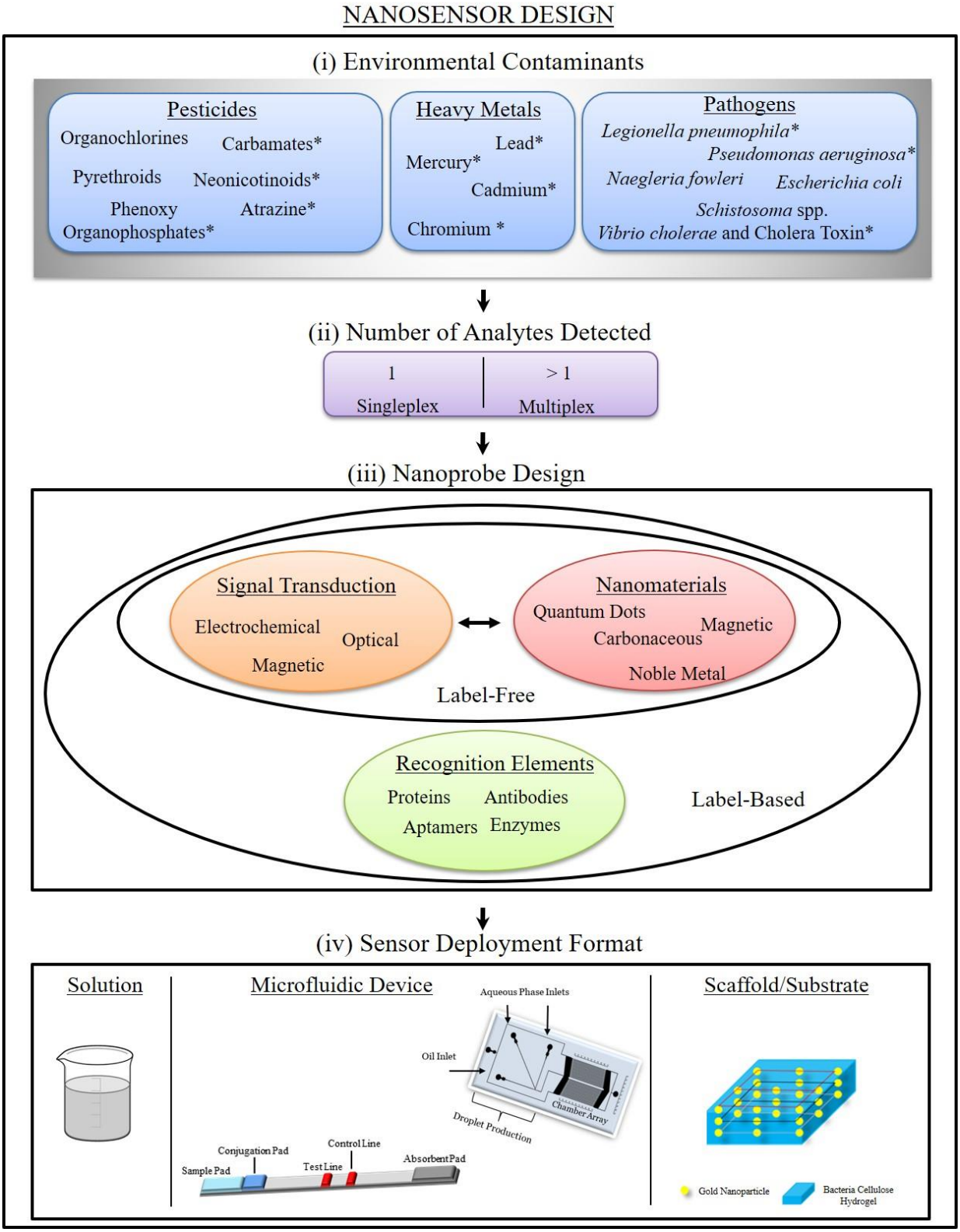

Figure 2.1. Nanosensor design schematic. First, a class and subsequently a specific contaminant of interest is selected (i). The contaminants discussed in this review are denoted with an asterisk. Next, the number of analytes to be detected by the sensor is chosen (ii) and then the probe is designed. A nanoprobe consists of two core elements, a signal transduction method and at least one nanomaterial, and may also include a recognition element (iii). Ultimately, the sensor deployment format is selected (iv).

2.3 Background

Nanomaterial enabled sensors consist of three components: the nanomaterial, a recognition element that provides specificity, and a signal transduction method, a way of relaying the presence of the analyte (**Figure 2.1)**. These components are not necessarily distinct entities within a sensor, but every nanosensor can be characterized on the basis of these three divisions. Sensors can be designed to detect a single analyte or multiple analytes, termed multiplex detection. In addition, to detecting an analyte by producing a signal, a 'turn-on' sensor, some of the sensors described below are based on a 'turn-off' mechanism, where-by a decrease in signal indicates the presence of an analyte.

2.3.1 Nanomaterials

Nanomaterials have enabled advances in sensor design such as miniaturization, portability, and rapid signal response times. High surface area to volume ratios and facile surface functionalization make nanomaterials highly sensitive to changes in surface chemistry thus enabling nanosensors to achieve extremely low detection limits. In some cases, the enhanced sensitivity of nano-enabled sensors is due to the fact that nanomaterials are of a similar size as the analyte of interest (e.g., metal ions, pathogens, biomolecules, antibodies, DNA) and are thus capable of interrogating previously unreachable matrices [5]. We briefly introduce three different general nanomaterial classes: quantum dots (QDs), metal nanoparticles, and carbonaceous nanomaterials.

Quantum Dots. Quantum dots (QDs) are semiconductor nanocrystals with a typical composition *MX* where *M* is commonly Cd or Zn and *X* is Se, S, or Te. QDs are often coated by a second MX alloy, a shell, to create core/shell QDs with highly tuned properties. Common QDs employed in sensor applications include: CdSe [17], CdSe/ZnS [18-20], CdTe [21-26], CdTe/CdS [23], ZnS [27], and ZnSe/ZnS [28]. QDs have characteristically narrow fluorescence emission bands, yet broad absorption bands, thus making them excellent optical transducers. Moreover, QD emission wavelengths can be readily adjusted by changing the size, shape or composition of the QD. Accordingly, QDs are ideal for multiplex detection of a number of

different analytes. QDs diverse in shape, size, and composition can be excited by a single energy source because they have broad absorption spectra.

Metal and Metal Oxide Nanoparticles. Because of their capacity to be produced in a wide variety of shapes, their high extinction coefficients ($\varepsilon > 3\times10^{11}$ $M^{-1}cm^{-1}$) [29], and their facile surface functionalization, noble metal nanoparticles (NP) have been extensively used in a number of sensor applications. Colloidal solutions of gold and silver nanoparticles, AuNP and AgNP respectively, exhibit unique colors based on the size of the colloidal nanomaterial. For example, AuNP spheres in the ~5 to ~50 nm diameter range appear red in color but become more purple in hue as they increase in size towards ~100 nm. This color change can be exploited for use in visual colorimetric sensors where the presence of an analyte causes small nanoparticles to aggregate and the solution to change color. Gold and silver nanoparticle excitation can lead to the uniform oscillation of conduction electrons. This uniform oscillation gives rise to localized surface plasmon resonance (LSPR) [30] based spectroscopies such as surface plasmon resonance (SPR) and surface enhanced Raman spectroscopy (SERS). Plasmon based spectroscopies are discussed in greater detail below and elsewhere [29-31].

The chemistry of metal NPs, particularly AuNPs, has been exploited for use in highly selective sensors [32, 33]. We note that although it is possible to use AgNPs for sensor applications, the anti-microbial activity of silver [34] and its propensity to dissolve often limits the utility of such sensors. Gold NPs are stable and biocompatible and have been extensively explored for use in sensing applications [10]. Surface coatings can be used to modify the particles and facilitate the attachment of recognition elements. Thiol capping agents provide colloidal stability and chemical functionality. Two commonly used thiols are thioglycolic acid (TGA) and 3-mercaptopropionic acid (MPA). These two agents impart a negative surface charge and create nanoparticles with an extremely high colloidal stability [35]. The choice of capping agent depends on the desired function and nanoparticle composition. The interested reader is referred to recent reviews by Saha [10] and Wei et al. [36] for additional details on gold enabled sensors.

A range of nanostructured metal oxides (NMOs) have been explored for sensing applications. NMOs include: iron oxides, titanium oxides, zirconium oxides, cerium oxides, zinc oxides, and tin oxides. Magnetic iron oxides, such as magnetite (Fe_3O_4) and maghemite (γ-Fe_3O_4), have low toxicity, are economically friendly and can be easily functionalized with ligands, antibodies, and other capping agents [37]. One important allure of magnetic NPs arises from their use in facilitated separation processes and remediation applications [15]. TiO_2 has also been embraced in nano-sensor design [38, 39], but it is most typically used and studied for its photocatalytic properties.

Carbon-based Nanomaterials. Carbon nanotubes (CNTs) and graphene are often employed in nano-enabled sensors because of their large surface area, excellent electrical conductivity, high thermal conductivity and mechanical strength [40]. One recent application of these nanomaterials has been their use to increase the sensitivity of glassy carbon electrodes (GCE) for electrochemical sensing [41, 42]. Other sensor designs have exploited the electronic properties of graphene for fluorescence quenching. In such a design, as discussed later in this review, a QD with a recognition element is conjugated to a graphene sheet and in the presence of the analyte the sensor undergoes a conformational change that separates the QD from the graphene and "turns-on" the sensor.

2.3.2 Recognition Elements

Selectivity is an extremely important facet in the design of a successful biosensor. A diverse array of recognition elements have been implemented in nanosensor design including antibodies [43-47], aptamers [48-53], enzymes [54], and functional proteins [55]. The two most widely used agents, antibodies and aptamers, are described here in detail.

Antibodies. Antibodies (Abs) are proteins produced by the immune system in response to foreign agents [56]. They exhibit highly specific binding to a single antigen and are widely used in the capture and labeling of microorganisms and other materials that elicit an immune response [57]. Three types of antibodies have been used for analyte recognition: polyclonal (pAbs), monoclonal (mAbs) and engineered antibody fragments [58]. While antibodies are widely used in biosensors, there are a number of drawbacks to

antibody use that include: high development costs, temperature and pH sensitivity, batch-to-batch variation, and short shelf-lives [45, 59]. Despite these disadvantages, for immunogenic analytes (i.e., those that elicit an immune response) Abs are often the most selective recognition agent [60]. Sensors that incorporate antibodies, either one type or multiple, are commonly referred to as immunosensors or immunoassays. A common descriptor of an electrochemical immunosensor is "label-free" because changes in the properties of the transducer surface owing to the antibody-antigen interaction can be directly measured [61].

Aptamers. Aptamers are flexible short oligonucleotide strands, either RNA or single stranded DNA (ssDNA), used to bind specific molecules. Produced both naturally and synthetically, aptamers have been designed to recognize toxic and non-immunogenic substances [62]. Aptamer production is estimated to cost approximately 10–50× less than antibody production [63]. Additionally, aptamers have low batch-to-batch variability, long shelf-lives, and are thermally stable [64]. Nucleic acid aptamers can be synthesized *de novo* with high specificity due either to the use of the systematic evolution of ligands by exponential enrichment (SELEX) process [65] or other newer isolation and synthesis approaches [66]. The SELEX process starts out by exposing a large library ($> 10^{14}$ strands) of random oligonucleotide sequences to the target sequence. Through affinity testing and PCR amplification the oligonucleotide sequences with the tightest binding are isolated, their sequences determined, and following *de novo* synthesis can be incorporated into biosensors.

2.3.3 Signal Transduction

The three major signal transduction methods employed in nano-enabled sensors are optical, electrochemical, and magnetic. Optical techniques, particularly colorimetric sensors that report a signal in the visible spectrum, are desirable for wide-scale use by the general public. A well-known example of a colorimetric biosensor is the home pregnancy test. Electrochemical sensing methods have high specificity and can be simplistic and facile to miniaturize [3]. Compared with optical and electrochemical methods, magnetic transduction methods exhibit minimal background signal thus making them ideal for low

concentration samples. Other sensor designs use magnetic materials to pre-concentrate the analyte prior to use of an optical or electrochemical transduction method.

Optical. Optical transduction is based on the interaction of a sensing element with electromagnetic radiation. Analytical techniques monitor emission or absorption of a sample under irradiation by ultraviolet, visible, or infrared light [67]. Two common optical methods utilized in nanosensor design are fluorescence and surface plasmon resonance enabled spectroscopies.

Fluorescence spectroscopy is based upon measurement of the emission of a fluorophore as it returns to its ground state following excitation. Fluorescent nanosensor applications often employ QDs or dye-doped silicon or polymer nanoparticle probes because they are photostable and are generally more robust than traditional fluorescent dyes [68, 69]. Designs are described by the change in the fluorescence signal upon interaction with an analyte of interest as either "turn-off" or "turn-on". Quenching or restoration of the fluorescence signal may be a result of a direct interaction between the analyte and the nanoparticle or a conformational change in the sensor.

Surface plasmon resonance enabled spectroscopies are an optical transduction technique based on the localized surface plasmon resonance (LSPR) of noble metal nanomaterials [4, 36]. The LSPR band is sensitive to the mean interparticle distance and therefore can be used to observe changes from a dispersed to an aggregated system or vice versa. Commonly, the LSPR is used in conjugation with a secondary spectroscopy technique to create a surface enhanced spectroscopy: surface enhanced fluorescence (SEF) or surface enhanced Raman spectroscopy (SERS) [68].

Electrochemical. Electrochemical detection methods measure the change in current or potential that result from the interaction between an analyte and an electrode. A multitude of techniques have been used to observe these changes and include cyclic voltammetry, chronoamperometry, chronopotentiometry, impedance spectroscopy, and various field-effect transistor based methods [5]. Nano-enabled sensor designs can involve modification of the solid electrode (e.g., Pt, Au, Ag, graphite) with nano-carbons (e.g., carbon nanotubes, graphene) or functionalization with recognition elements (e.g., antibodies, aptamers) [3].

Direct spatial contact between the nanoscale architecture of the electrode and the recognition element gives rise to large signal amplification and improved signal to noise ratios compared to traditional electrochemical techniques [3, 5, 70]. In addition to the electrode properties, the size and morphology of the analyte of interest has been shown to affect sensor function. Improved detection limits have been shown for smaller particles due to their higher diffusivity and lower steric hindrance [71].

Magnetic. Magnetic transduction has been embraced for detection in biological samples because of the low background magnetic signal [72] and the fact that magnetic nanoparticles (MNP) can be collected under an applied magnetic field regardless of the optical properties of the solution [68]. Often, the use of magnetic nanoparticles to concentrate, separate and purify the analyte of interest in the detection zone is termed magnetic transduction [72]. However, a secondary transduction method, such as electrochemical stripping, can often be employed and therefore use of the term magnetic transduction can be a misnomer.

Magnetic-relaxation switches that incorporate superparamagnetic iron oxide nanoparticles are a pure form of magnetic transduction. The principle underlying this detection mechanism is the clustering of individual nanomagnetic probes into larger assemblies following interaction with a target. Analyte binding results in the formation of NP clusters and enhanced dephasing of the spins of the surrounding water protons. The subsequent change in the spin–spin (T2) relaxation can be detected by magnetic resonance relaxometry [12, 73]. Magnetic relaxation switches have been used to detect nucleic acids (DNA and mRNA), proteins [74] and viruses [75] among other targets.

2.4 Analytes

As defined at the outset of this review, a wide variety of different analytes can be detected by nanomaterial-based sensors. In this portion of the review, we focus explicitly on the applications of nanosensors towards detection of pesticides and metals.

2.4.1 Pesticides

There is great interest in detection of pesticides given their widespread use, their toxicity, and their proclivity for bioaccumulation. Currently, over 800 active ingredients, in 100 different substance classes are present in commercial pesticides [76]; we summarize the major pesticide classes in **Table 2-1**. Organophosphorus (OP), carbamates, neonicotinoids, and triazines are the dominant classes and to date have been the focus of nano-enabled pesticide detection. Liu et al. [76], Verma et al. [77], Aragay et al. [2], Evtugyn et al. [61] and Pang et al. [78] , provide detailed reviews of pesticide detection techniques. In this section, a brief background on pesticide detection will be followed by a discussion of recent advances.

Table 2-1: Common Pesticide Classes

Class of Chemical Pesticides	Examples	Types	Effects
Carbamates	Carbaryl; methomyl; propoxur; aldicarb	fungicide, insecticide, acaricide	Non-persistent, cholinesterase-inhibiting, not very selective, toxic to birds and fish
Neonicotinoids	Acetamiprid; clothianidin; imidacloprid; nitenpyram; nithiazine; thiacloprid; thiamethoxam	insecticide	Water soluble; concern regarding persistence and bioaccumulation
Organochlorines	Aldrin; chlordane; dieldrin; endrin; heptachlor; lindane; methoxychlor; toxaphene; hexachlorobenzene (HCB); pentachlorophenol (PCP); DDT	insecticide, acaricide, fungicide	Persistent, bioaccumulative, affect the ability to reproduce, develop, and to withstand environmental stress by depressing the nervous, endocrine and immune systems
Organophosphates	Schradan; parathion; malathion	insecticide, acaricide	Non-persistent, systemic (cholinesterase-inhibiting), not very selective, toxic to human
Phenoxy	2,4-D 2,4,5-T	herbicide	Selective effects on humans and mammals are not well known 2,4-D: potential to cause cancer in laboratory animals 2,4,5-T: is the source of a toxic contaminant dioxin
Pyrethroids	Fenpropanthrin; deltamethrin; cypermethrin	insecticide	Target-specific: more selective than the organophosphates or carbamates, generally not acutely toxic to birds or mammals but particularly toxic to aquatic species
Triazines	Atrazine, cyanazine, and simazine	herbicides	Persistent, binds to the plastoquinone-binding protein in photosystem II; endocrine disruptor in humans

Organophosphates. Pesticides are often designed to impact a specific enzyme; many forms of pesticide detection are based on observing and monitoring this enzyme either directly or indirectly. Organophosphate

and carbamate pesticides inhibit the production of acetylcholinesterase (AChE) an enzyme that catalyzes the hydrolysis of acetylcholine, a neurotransmitter [79, 80]. The fundamental reaction is shown in Equation 2-1;

$$acetycholine + H_2O \xrightarrow{AChE} choline + acetate \qquad \text{Equation 2-1}$$

A class of rapid and sensitive electrochemical sensors has been developed around the immobilization of AChE on a solid electrode surface [42, 81-83]. The products of Equation 2-1 are not electroactive and thus to detect the inhibition of AChE an analogous reaction based on the hydrolysis of acetylthiocholine is typically used [84].

For example, Yang et al. [8] combined two different types of nanomaterials, reduced graphene oxide (rGO) and gold nanoparticles, to achieve a detection limit of 0.5 nM for the model organophosphate paraoxon-ethyl (**Figure 2.2**). Reduced graphene oxide sheets provide an increased surface area for AChE immobilization and were deposited with polypyrrole (PPy) to prevent aggregation. Gold nanoparticles (~20 nm) were then electrodeposited onto the PPy-rGO surface to further increase both the surface area and the conductivity of the electrode. The final step was co-deposition of AChE and a silica matrix, $(NH_4)_2SiF_6$. The biocompatible silica matrix prevented the AChE from leaking out of the electrode and ensured that the enzymes maintained their bioactivity. The completed sensor was tested using cyclic voltammetry and AChE inhibition was defined based on the peak experimental current and control current.

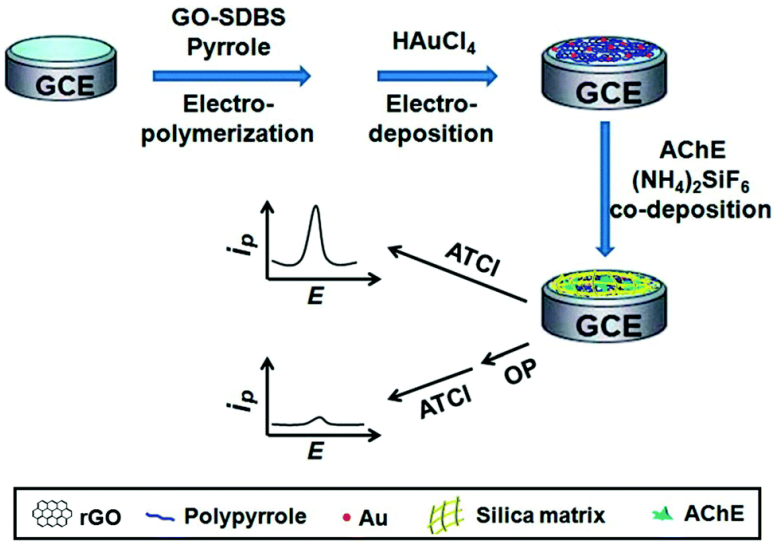

Figure 2.2. Illustration of the preparation of the Au–PPy–rGO nanocomposite-based AChE biosensor and its application for the electrochemical detection of organophosphorus pesticides. Reproduced from Yang et al. [8] with permission of The Royal Society of Chemistry.

Similarly, Yu et al. [85] used the large surface area of a carbon nanomaterial to create a sensitive organophosphorus pesticide (OP) biosensor. Amino functionalized carbon nanotubes (CNT–NH_2) were dried on the surface of a standard glassy carbon electrode (GCE) and subsequently incubated with AChE. Using differential pulse voltammetry (DPV), the limit of detection of the CNT decorated GCE was 0.08 nM.

Recently, Cui et al. [86] reported the use of a nanocomposite to improve the stability of AChE electrochemical biosensors. A layer of reduced graphene oxide (rGO) was introduced onto a glassy carbon electrode, followed by deposition of a titanium dioxide (TiO_2) porous sol-gel film mixed with chitosan (CS), a bio-compatible polymer. The stability of the matrix was further improved by the electro-deposition of a second layer of CS to yield a multi-layer mesoporous nanostructure. Total detection time required approximately 25 min and the limit of detection of dichlorvos, a model OP, was 29 nM. Although, the limit of detection of the sensor described in Yu et al. was better, without a side-to-side comparison of the sensors using the sample test matrix no conclusion can be drawn with regard to sensor performance.

Pang et al. [87] explored the application of an aptamer SERS sensor in complex food samples. The assay utilized a unique aptamer developed by Zhang et al. [88] that can detect four distinct organophosporous pesticides: phorate, profenofos, isocarbophos, and omethoate. Dendritic silver, an organized nanostructure, was selected as the SERS substrate because it provides locally consistent SERS enhancement factors [89]. The surface was decorated with aptamers and also a blocking agent, 6-mercaptohexanol (MH), to eliminate non-specific binding on the silver surface. Probes were incubated with the pesticides, removed from solution via centrifuge and dried prior to Raman interrogation. Analysis of each molecule's unique Raman fingerprint led to the determination of four distinct limits of detection: phorate 0.4 μM, isocarbophos 3.5 μM, omethoate 24 μM, and profenofos 14 μM.

Recently, Nie et al. [90] reported a similar SERS-aptamer sensor, but with aqueous sample detection. Unlike Pang et al.'s requirement to wash and drop-dry the sensors onto a glass slide, Nie et al. mixed a malathion (OP) specific antibody with positive charged spermine coated silver nanoparticles and directly collected SERS spectra from the suspension. The phosphate backbone of the aptamer is negatively charged and electrostatic interactions led the aptamer complex to attach to the silver nanoprobes. Nie et al. describe their sensor as label free; however, in our paradigm the use of a recognition agent albeit not attached to the nanoparticle leads to classification under the aptasensor title.

Fewer reports have described traditional optical immunoassays, such as the lateral flow immunoassay (LFIA), for OP detection. Wang et al. [91] developed a "bare-eye" assay with antibody functionalized gold nanoparticles that enabled the user to visually verify the presence or absence of three pesticides of interest: imidacloprid, chlorpyrifos-methyl (OP) and isocarbophos (OP). Of the three antibodies used, the antibody for isocarbophos (neonicotinoid) had to be developed in-house because it had not previously been reported in the literature. In fact, antibodies exist for only about ~10% of the 800 active pesticide ingredients [76]. The production of a large library of pesticide antibodies has been stymied by the costs and difficulties in creating antibodies for these low molecular weight and non-rigid molecules [2]. For this reason, aptamers have recently been explored for selective pesticide detection.

Neonicotinoids. A class of neuro-active insecticides, neonicotinoids were first introduced in the 1980s and are currently the largest class of insecticides in use [92]. However, there are growing concerns regarding the impact of neonicotinoid to human health [93]. Nanosensors for neonicotinoid detection have focused specifically on the detection of acetamiprid with aptamers being the prefer recognition element as underscored by Verdian's recent review paper [94]. For example, Weerathunge et al. exploited standard aptamer functionality to create a novel sensor based on the peroxidase-like activity of gold nanoparticles [95]. As shown in **Figure 2.3**, the colorless reporter molecule 3,3,5,5-tetramethylbenzidine (TMB), which turns purplish-blue upon oxidation, was used to create an off/on sensor with a signal observable via UV-visible absorbance. In the presence of an acetamiprid-specific aptamer, the oxidation of TMB is blocked. The introduction of the target molecule led to the desorption of the aptamer and restoration of TMB oxidation within 10 minutes. The authors reported a limit of detection of 0.1 ppm (450 nM) with a dynamic linear detection range of 0.1 to 10 ppm.

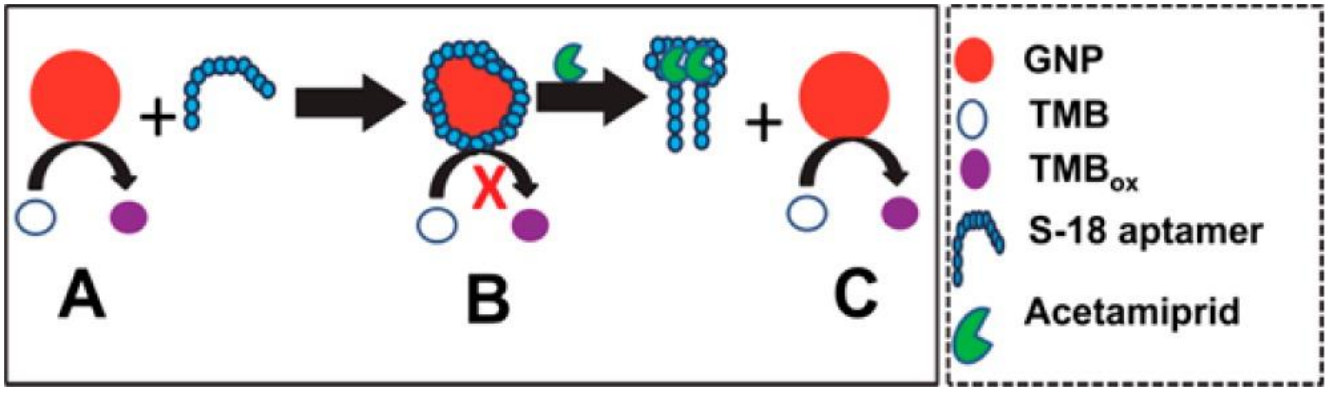

Figure 2.3. Schematic representation of the reversible inhibition of the nanozyme activity of GNPs using an acetamiprid-specific S-18 ssDNA aptamer. Step A shows intrinsic peroxidase-like activity of GNPs that gets inhibited after shielding of the GNP surface through conjugation of S-18 aptamer molecules (step B). In the presence of acetamiprid target, the aptamer undergoes target-responsive structural changes and forms a supramolecular complex with acetamiprid resulting in free GNP to resume its peroxidase like activity (step C). Reprinted with permission from Weerathunge et al. [95]. Copyright 2014 American Chemical Society.

Triazine. A class of nitrogen heterocycles, triazines detection is typical defined by atrazine detection because, as of 2014, atrazine was the second most used herbicide in the United States [96]. A range of label-based [97, 98] and label-free [7, 99, 100] designs have been embraced for the detection of atrazine. For example, Liu et al. [97] a competitive electrochemical immunoassay. A gold electrode decorated with gold nanoparticles was functionalized with anti-atrazine monoclonal antibodies. Differential pulse voltammetry measurements were then used to directly measure changes in the electrode surface resulting from the antibody-antigen interaction. The sensor was determined to be highly sensitive with a limit of detection of 74 pM.

A unique substrate deployed sensor was introduced by Wei and Vikesland [7] for the detection of atrazine. A gold nanoparticle/bacteria cellulose (AuNP/BC) plasmonic nanocomposite was synthesized by the *in-situ* reduction of gold salt in the presence of bacteria cellulose. As shown in **Figure 2.4**, pH-triggered attachment of atrazine to the nanocomposite was achieved by lowering the pH of the solution below atrazine's pK_a of 1.7 and was confirmed by an increase in the SERS signal in the AuNP/BC. Ultimately, the group was able to achieve a limit of detection of 11nM (2.3), which is below the EPA's maximum concentration of 3μg/L for drinking water but three orders of magnitude greater than the label-based detection.

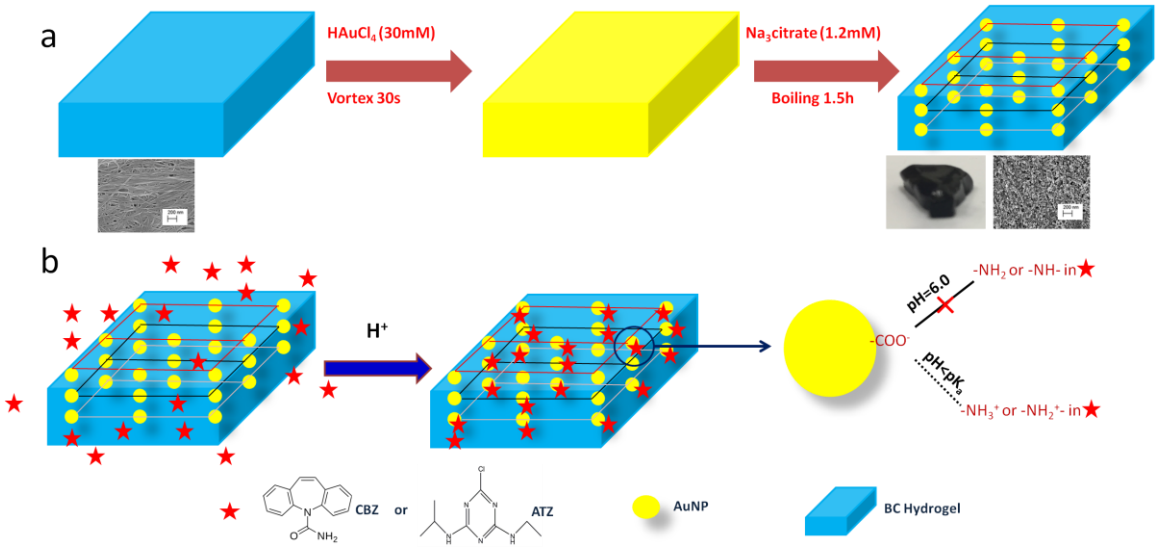

Figure 2.4. Schematic of synthesis of gold nanoparticle/bacteria cellulose nanocomposites (a). Schematic of pH-induced adsorption of carbamazepine (CBZ) and atrazine (ATZ) on AuNP/BC (b). Reprinted with permission from Wei and Vikesland [7] from Springer Nature.

2.4.2 Metals

Nano-enabled sensors have been successfully developed for a number of heavy metals and in this section, we review mercury, lead, cadmium, and chromium detection. A diverse array of transducers and nanoparticles are used to detect these environmentally relevant contaminants with the aim of developing sensitive and selective sensors. Readers interested in additional information about nanosensors for heavy metal detection are directed to the reviews of Li et al. [14] and Ullah et al. [101].

Mercury. The negative neurological effects of mercury exposure to humans have driven extensive investigation into the geochemical cycling and detection of this element [102]. A major focus of mercury ($Hg^{(II)}$) nanosensor development has been the production of DNA-based probes [19, 53-55, 103-105]. Thymine-thymine (T-T) base-mismatches in DNA are significantly stabilized in the presence of $Hg^{(II)}$ [103] due to the formation of metal base pairs [106]. Two major types of oligonucleotide mercury probes have been reported in the literature: G-quadruplexes [54, 55], which unfold, and nearly complementary single strands, which hybridize [105]. A growing number of mercury sensors are being constructed using multiple nano-elements, such as the mercury sandwich assay described by Liu et al.[19]. In this assay, magnetic silica spheres encapsulated in a gold shell and Raman labeled gold nanoparticles were functionalized with

complementary DNA sequences that contained five mismatched thymine sites, Figure 2.5. The DNA sequences were chosen such that the binding energy between the complementary aspects of the strands was insufficient to allow them to fully hybridize. In the presence of mercury, full hybridization occurred thus decreasing the inter-probe spacing and creating a plasmonic hotspot. Owing to the magnetic particle cores, the nanoprobes could be easily recovered with an external magnet and subsequently recycled, **Figure 2.5**.

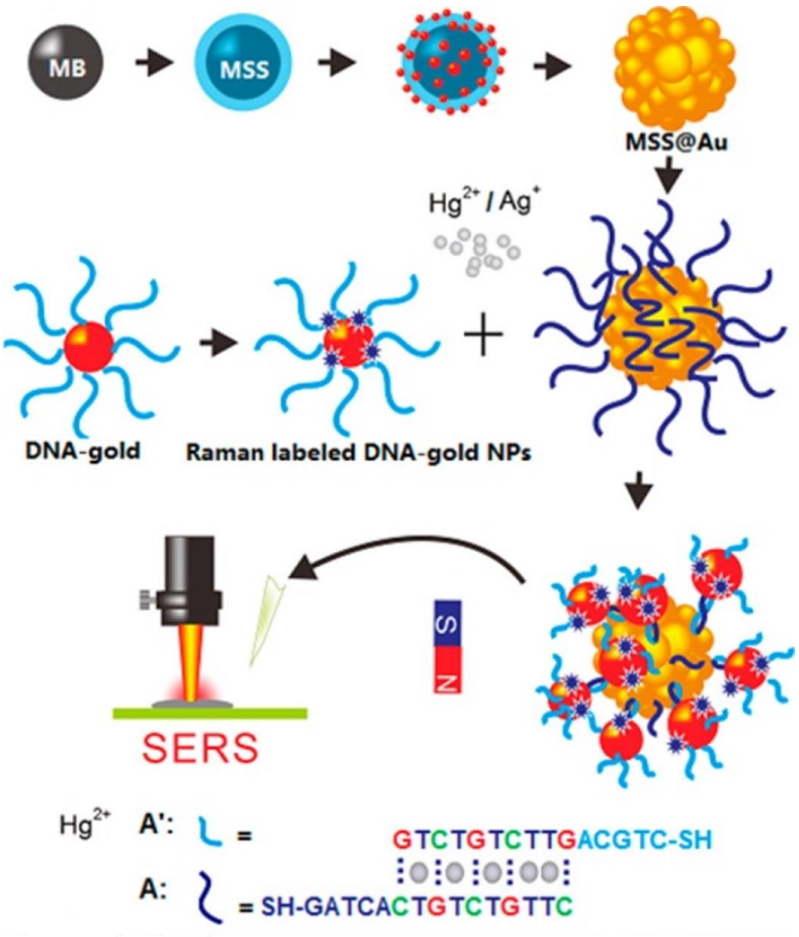

Figure 2.5. Schematic illustration of the SERS-active system for $Hg^{(II)}$ ion detection based on T−Hg−T bridges using DNA-Au NPs and DNA-MSS@Au NPs. Reprinted from Reprinted with permission from Liu et al. [51]. Copyright 2014 American Chemical Society.

Thiol mediated assays for mercury detection have been described in the literature for a variety of nanoparticles such as gold [107-110], silver [111] or quantum dots[28]. Aggregation[107] or disaggregation [108] are typically utilized to provide a colorimetric response. Reaction based competition assays in which $Hg^{(II)}$ replaces a surface coating have also been described in the literature [33, 109]. Huang and Chang

created an on-sensor that emitted a fluorescence signal in the presence of mercury due to the displacement of rhodamine 6G (R6G) from the nanoparticle surface [109]. In the process of iterating through three sensor designs to create a sensitive and selective assay, the authors found that thiol coatings increased the specificity of the assay for mercury. The final sensor was reported to have a limit of detection of 2.0 ppb and a rapid analysis time (<10 min).

Lead. Associated with increased risk of cancer and subtle cognitive and neurological deficits[112], lead (Pb) is a heavy metal contaminant of major concern. Labeled and label-free nanosensors have both been reported for sensitive $Pb^{(II)}$ detection. For label-based detection, the recognition element 8–17 DNAzyme, a catalytic nucleic acid, has been used [113, 114] as well as a class of oligonucleotides that form G-quadruplexes in the presence of lead [18, 49, 115].

Tang et al. [114] combined 8-17 DNAzyme with rolling circle amplification (RCA) and quantum dots to develop an electrochemical sensor with a lead limit of detection of 7.8 pM. In this assay, DNAzyme catalytic strands were immobilized onto a magnetic bead (MB) and then hybridized with a substrate strand containing a single sessile ribonucleoside adenosine (rA) to form double stranded DNA with a single stranded loop to accommodate $Pb^{(II)}$ ion. In the presence of $Pb^{(II)}$, the DNAzyme was activated to cleave the substrate strand at the rA group. The exposed single DNA strand, tethered to the MB, then hybridizes with the RCA template. Polymerase and dNTPs were then added to trigger the RCA process and yield a long single stranded product with repeating sequence units. The complement of the RCA sequence was functionalized to CdS quantum dots leading to the hybridization of multiple QDs in a periodic arrangement. QD rich DNA duplexes were then magnetically separated from the solution and dissolved in nitric acid. The released cadmium cations were quantified via square wave voltammetry.

Gao et al. developed an AlOOH-graphene oxide nanocomposite for the detection of lead and cadmium by square wave anodic stripping voltammetry (SWASV) [116]. In this assay, the fast electron transfer kinetics achieved with graphene oxide were coupled to the high adsorption capacity of AlOOH to create a nanocomposite with a LOD of 76 pM. Unlike the RCA method, the AlOOH was not selective for a single

metal. However, since each metal has a unique stripping peak the AlOOH-graphene oxide nanocomposite could be used for multiplex detection.

Cadmium. The body of work on nano-enabled sensors for cadmium (Cd) detection is less robust than that for mercury and lead, but detection limits on the order of nano-molar have been reported. A variety of nanomaterials have been explored including QDs [23, 117], SWCNT[118], and antimony nanoparticles [119].

Gui et al.[23] described an off/on-sensor fluorescence sensor for $Cd^{(II)}$ detection. Photoluminescent CdTe/CdS QDs were first quenched (i.e., turned-off), by ammonium pyrrolidine dithiocarbamate (APDC) due to the partial loss of the Cd–thiol surface layer and subsequent surface passivation. Introduced cadmium ions displaced the APDC from the QD surface and restored the photoluminescence; thus, turning the sensor on. The sensor was highly selective for $Cd^{(II)}$, a threefold increase was seen in the PL intensity, and a limit of detection of 6 nM was determined.

Gui et al. [117] enhanced the accuracy of their $Cd^{(II)}$ detection device by creating a ratiometric sensor. In this sensor, the fluorescence of two different chromophores was measured in order to minimize the error introduced by fluctuation in the photoluminescence of the QDs. To limit interactions between the QDs and the secondary dye, the CdTe QD cores were coated with a polymer, polyethylenimine (PEI), prior to conjugation with fluorescein isothiocyanate (FITC). The QDs were then quenched using sulfur (S^{2-}) while the FITC signal was maintained. Again, upon introduction of cadmium the sensor was turned on and the photoluminescence was restored. The limit of detection was slightly higher for this sensor compared to the same groups initial report, 12 nM vs. 6 nM, but was linear across a much larger range of 0.1 to 15 μM compared with 0.1 to 2 μM.

Chromium. High chromium (Cr) absorption *in vivo* can result in various diseases, including fibro-proliferative diseases, airway hypersensitivity, lung cancer, nasal cancer, and other types of tumors. Multiple immunoassays have been described for the detection of chromium [46, 47], but they are all based on the work of Liu et al. [47]. In pursuit of an immunochromatographic assay (ICA), Liu et al. developed

novel anti-$Cr^{(III)}$-EDTA monoclonal antibodies (McAb). Chromium ions are too small to elicit an immune response and thus they were mixed with the highly effective bifunctional chelating agent, isothiocyanobenzyl-EDTA, iEDTA, and conjugated to the carrier protein bovine serum albumin (BSA) before being introduced to mice. The three main components of the assay are the conjugation pad, the t-line, and the c-line. The probes, gold-labeled anti-Cr-EDTA McAb, were loaded onto the conjugation pad. The test line, t-line, is made of the analytes of interest (Cr-EDTA) and the control line, c-line, contains goat- anti-mouse antibodies. The control line is used to verify that the antibodies in the conjugation pad have indeed traveled the length of the dipstick. A sample is introduced at the bottom of the dipstick, as it travels through the conjugation pad the antibody probes are introduced to the solution. The probes interact with their specific target, if it is present in the sample, as capillary action draws the whole solution towards the t-line. For a negative sample, the free antibody probes can bind to the test line, whereas in a positive sample no probes will bind as all antibody sites are already occupied. The antibodies at the c-line will capture any probes in the solution even those that are bound to the target of interest. The ultimate result of Liu et al. was an assay with a visual limit of detection of 50 ng/mL and an analysis time of less than 5 minutes.

2.4.3 Pathogens

Ever since John Snow's 1854 revelation that cholera was spread through the consumption of contaminated water, waterborne pathogen detection has been a key area of research. The World Health Organization (WHO) recognizes twelve bacteria, eight viruses, seven protozoa, and two helminths as pathogens of significance in drinking water supplies, as outlined in **Table 2-2** [1]. Pathogen detection methods typically focus on: i) whole analyte (cell) detection or detection of a representative epitope on the cell membrane; ii) genetic material detection; or iii) pathogenic product (e.g., toxin) detection. For the sake of brevity, herein we confine our discussion to the detection of *Vibrio cholerae* and the toxin it produces, cholera toxin, *Legionella pneumophila*, which was responsible for greater than 50% of the waterborne disease outbreaks between 2011 and 2012 [120], and *Pseudomonas aeruginosa,* which the WHO recently

classified as a critical pathogen in light of the proliferation of antimicrobial resistant species [121] . For expanded reviews we refer the reader to the works of Kumar et al. [122] and Mocan et al. [123].

Table 2-2: Waterborne Pathogens and Their Significance in Water Supplies[a]

Pathogen	Health Significance	Persistence in Water Supplies
Bacteria		
Burkholderia pseudomallei	High	May multiply
Campylobacter jejuni, C. coli	High	Moderate
Escherichia coli – Pathogenic	High	Moderate
E. coli – Enterohaemorrhagic	High	Moderate
Legionella spp.	High	May multiply
Non-tuberculous mycobacteria	Low	May multiply
Pseudomonas aeruginosa	Moderate	May multiply
Salmonella typhi	High	Moderate
Other salmonellae	High	May multiply
Shigella spp.	High	Short
Vibrio cholerae	High	Short to long
Yersinia enterocolitica	Moderate	Long
Viruses		
Adenoviruses	Moderate	Long
Enteroviruses	High	Long
Astroviruses	Moderate	Long
Hepatitis A virus	High	Long
Hepatitis E virus	High	Long
Noroviruses	High	Long
Sapoviruses	High	Long
Rotavirus	High	Long
Protozoa		
Acanthamoeba spp.	High	May multiply
Cryptosporidium parvum	High	Long
Cyclospora cayetanensis	High	Long
Entamoeba histolytica	High	Moderate
Giardia intestinalis	High	Moderate
Naegleria fowleri	High	May multiply
Toxoplasma gondii	High	Long
Helminths		
Dracunculus medinensis	High	Moderate
Schistosoma spp.	High	Short

a) Adapted from WHO Table 7.1 Waterborne pathogens and their significance in water supplies [1]

Vibrio cholerae and Cholera Toxin. Cholera, the infamous disease that spawned germ theory is now virtually unknown in the United States, but it continues to pose a major disease burden around the world with an estimated 1.3 to 4.0 million cases of cholera a year leading to between 21,000 to 143,000 deaths [124]. Cholera is an acute diarrhoeal disease caused by the ingestion of contaminated water or food

containing the bacterium *Vibrio cholerae.* In the intestines, the bacteria colonize the mucosa and begin to secrete cholera toxin (CT), which initiates the disease symptoms[125]. Nanosensors have been fabricated to detect both *Vibrio cholerae [126, 127]* and CT, but the majority of the literature has focused on detection of CT subunit B (CT-B) [128-132] because the subunit induces cellular uptake of the toxin and not all *V. cholerae* isolates are toxigenic[133]. Label-based detection of CT can be achieved using antibodies, Ganglioside GM1 (the binding site of CT), or β-galactose, a sugar with strong affinity towards CT. Ahn et al. [128] provide a nice summary of CT-B detection and reported a fluorescence resonance energy transfer (FRET) based method with a theoretical detection limit of 280 pM. In FRET, fluorescence from QDs is quenched, and the energy is transferred by another particle such as a gold nanoparticle. The quenching is inhibited in the presence of the target. Specifically, the cholera toxin binds to the β-galactose modified gold nanoparticles prohibiting the binding of the QDs.

Legionella pneumophila. Named for the famous 1976 outbreak at the American Legion, Legionnaires' disease is a pneumonia like disease caused by the bacterium *Legionella pneumophila*. Under specific conditions, the bacterium can flourish in building (premise) plumping and infect people when they inhale aerosols containing the infective agent. Two approaches have been presented in the literature for nano-enabled *Legionella* detection: whole organism detection [134, 135] and DNA detection [16, 136, 137].

Martin el al. developed on a whole organism sensor [134] that combined a sandwich immunoassay for bacterial capture with amperometric transduction. Magnetic nanoparticles (MNP) were modified with poly(dopamine) (pDA) and ultimately functionalized with specific capture antibodies (C-Ab) to create MNPs@pDA-C-Ab probes. After incubation with the sample, a second detector antibody (D-Ap) labeled with horseradish peroxidase (HRP-D-Ab) was introduced and a magnetic field was used to capture the immunocomplexes on a screen-printed carbon electrode (SPCE). The authors found the assay to be specific for *Legionella,* but that they needed a preconcentration step in order to achieve a limit of detection (LOD) below the reference of 100 CFU L^{-1}. However, with a runtime of < 3 hour, compared to 10 days for the

gold standard approach, and a LOD of 10 CFU $mL^{-1,}$ the sensor has the potential to be used as a rapid first screening method for highly contaminated water systems.

In a recent report, Melaine et al. [16] described the multiplex detection of 16S rRNA from *Legionella*, *Pseudomonas aeruginosa* (discussed below) and *Salmonella typhimurium*. A DNA microarray with capture DNA specific for each target was assembled on a surface plasmon resonance imaging (SPRi) substrate, e.g., gold coated nanoprisms. Upon hybridization of the DNA with isolated 16S rRNA a change in the reflectivity signal was observed, as shown in the bottom of **Figure 2.6**. To extend the dynamic range of detection and enhance sensitivity, gold nanoparticles functionalized with a detection probe were introduced to the sample and ultimately RNA at concentrations as low as 10 pg mL^{-1} were detected.

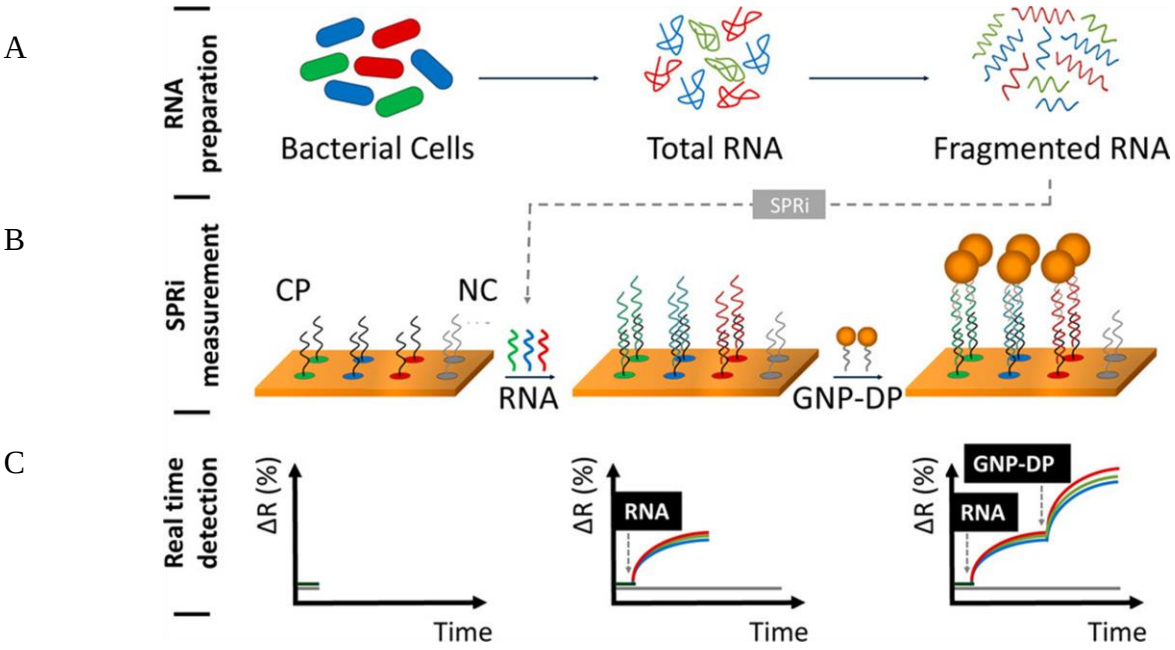

Figure 2.6. A schematic of multiplex RNA detection using surface plasmon resonance imaging (SPRi). RNA fragments are first extracted from bacteria of interest (A). A biochip functionalized with three specific capture probes (CP) and a negative control probe (NP), each demarcated in a unique color (Bi) is shown to exhibit no change in reflectivity (Ci). Upon introduction to the RNA (Bii), there is an increase in single (Cii). Finally, gold nanoparticles functionalized with the detection probe (GNP-DP) are introduced and shown to enhance the change in reflectivity. Adapted with permission from Melaine et al. [16]. Copyright 2017 American Chemical Society.

Pseudomonas aeruginosa. An opportunistic pathogen, *Pseudomonas aeruginosa* can be found in sources such as faces, soil, water, and sewage with the most important route of exposure being skin (dermal) contact with contaminated water or tools. Similar to *Legionella, P. aeruginosa* can colonize premise plumbing and has been associated with outbreaks of nosocomial infections in hospitals[138]. Most of the detection schemes reported for *P. aeruginosa* focus on whole pathogen detection[9, 139-142] with the work of Melanie et al. [16], discussed above, on 16s rRNA detection being an outlier. In addition, to oligonucleotide recognition elements [9, 16, 139, 140], antibodies [141, 143] and bacteriophages [142] have also been used for specific detection of *P. aeruginosa*.

The first *P. aeruginosa* aptamer was discovered by Wang et al. [144] in 2011 and subsequently has been used in a range of sensors. The discussion that follows highlights two sensors that utilize optical transduction. Yoo et al. [139] and Hu et al. [9] fabricated nano-textured substrates to produce localized surface plasmon resonance (LSPR) chips. Yoo et al. choose a three-step fabrication approach, first gold was deposited on a glass slide, silica nanoparticles were then deposited and then followed by the deposition of a second gold layer whereas Hu et al. opted for standard nanosphere lithography. The two groups also chose different methods to functionalize the sensor with Yoo et al. attaching the aptamers directly to the sensor surface via a gold-thiol bond. In contrast, Hu et al. used a polyethylene glycol (PEG) spacer to minimize steric hindrance for the aptamers with the goal of achieving a lower detection level, **Figure 2.7**. Hu et al. were successful at developing a sensor with a linear response at low concentrations and a lower limit of detection, 10 colony forming unit (CFU) mL^{-1} vs. Yoo et al.'s 10^4 CFU mL^{-1}. It should be noted that one of Yoo et al.'s goals was to create a low volume sensor and that their LOD was obtained in a 3 µL sample.

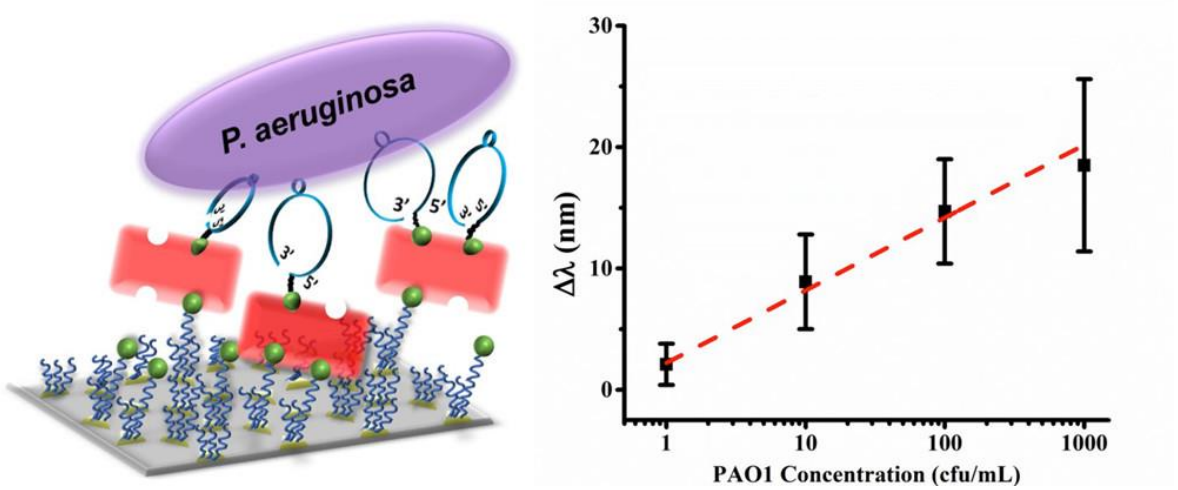

Figure 2.7. Schematic illustration of LSPR sensor chip (left) with legend (right) (a). Representative SEM images of Au nanotriangle arrays before (b), and after (c), exposure of the sensor surface to *P. aeruginosa* strain PAO1. Reprinted with permission from Hu et al. [9]. Copyright 2018 American Chemical Society.

2.5 Conclusions

Nanosensor development for environmental contaminants is growing rapidly and as described throughout this review nanomaterials and recognition agents are continuously being combined in new and creative ways. The recent developments in sensor design aim to overcome the shortcomings of first generation sensors such as nonspecific binding, particle size variation, nanoparticle aggregation, and nanoparticle stability. Questions of assay selectivity and sensitive in complex environmental matrices remains but a growing number of reports are using representative matrices to demonstrate the stability and selectivity of their sensors. The robustness of field deployable sensors is a must if individuals are going to be empowered to analyze their environment.

2.6 References

1. **World Health Organization. Guidelines for Drinking-Water Quality - Volume 1 Recommendations.** 2008.
2. Aragay G, Pino F, Merkoci A: **Nanomaterials for sensing and destroying pesticides.** *Chem Rev* 2012, **112:**5317-5338.
3. Sadik OA, Aluoch AO, Zhou A: **Status of biomolecular recognition using electrochemical techniques.** *Biosens Bioelectron* 2009, **24:**2749-2765.
4. Bănică F-G: **Nanomaterial Applications in Optical Transduction.** In
5. Grieshaber D, MacKenzie R, Vörös J, Reimhult E: **Electrochemical Biosensors - Sensor Principles and Architectures.** *Sensors* 2008, **8:**1400-1458.
6. Liu G, Lin Y: **Nanomaterial labels in electrochemical immunosensors and immunoassays.** *Talanta* 2007, **74:**308-317.
7. Wei H, Vikesland PJ: **pH-Triggered Molecular Alignment for Reproducible SERS Detection via an AuNP/Nanocellulose Platform.** *Scientific Reports* 2015, **5:**18131.
8. Yang Y, Asiri AM, Du D, Lin Y: **Acetylcholinesterase biosensor based on a gold nanoparticle-polypyrrole-reduced graphene oxide nanocomposite modified electrode for the amperometric detection of organophosphorus pesticides.** *Analyst* 2014, **139:**3055-3060.
9. Hu J, Fu K, Bohn PW: **Whole-Cell Pseudomonas aeruginosa Localized Surface Plasmon Resonance Aptasensor.** *Anal Chem* 2018.
10. Saha K, Agasti SS, Kim C, Li X, Rotello VM: **Gold nanoparticles in chemical and biological sensing.** *Chem Rev* 2012, **112:**2739-2779.
11. Lu AH, Salabas EL, Schuth F: **Magnetic nanoparticles: synthesis, protection, functionalization, and application.** *Angew Chem Int Ed Engl* 2007, **46:**1222-1244.
12. Reddy LH, Arias JL, Nicolas J, Couvreur P: **Magnetic Nanoparticles: Design and Characterization, Toxicity and Biocompatibility, Pharmaceutical and Biomedical Applications.** *Chemical Reviews* 2012, **112:**5818-5878.
13. Xu Z, Dong J: **Synthesis, Characterization, and Application of Magnetic Nanocomposites for the Removal of Heavy Metals from Industrial Effluents.** In *Emerging Environmental Technologies.* Edited by Shah V: Springer Netherlands; 2008: 105-148
14. Li M, Gou H, Al-Ogaidi I, Wu N: **Nanostructured Sensors for Detection of Heavy Metals: A Review.** *ACS Sustainable Chemistry & Engineering* 2013, **1:**713-723.
15. Mohmood I, Lopes C, Lopes I, Ahmad I, Duarte A, Pereira E: **Nanoscale materials and their use in water contaminants removal—a review.** *Environmental Science and Pollution Research* 2013, **20:**1239-1260.
16. Melaine F, Saad M, Faucher S, Tabrizian M: **Selective and High Dynamic Range Assay Format for Multiplex Detection of Pathogenic Pseudomonas aeruginosa, Salmonella typhimurium, and Legionella pneumophila RNAs Using Surface Plasmon Resonance Imaging.** *Analytical Chemistry* 2017, **89:**7802-7807.
17. Algarra M, Campos BB, Alonso B, Miranda MS, Martínez ÁM, Casado CM, Esteves da Silva JCG: **Thiolated DAB dendrimers and CdSe quantum dots nanocomposites for Cd(II) or Pb(II) sensing.** *Talanta* 2012, **88:**403-407.
18. Li M, Zhou X, Guo S, Wu N: **Detection of lead (II) with a "turn-on" fluorescent biosensor based on energy transfer from CdSe/ZnS quantum dots to graphene oxide.** *Biosens Bioelectron* 2013, **43:**69-74.
19. Luan W, Yang H, Wan Z, Yuan B, Yu X, Tu S-t: **Mercaptopropionic acid capped CdSe/ZnS quantum dots as fluorescence probe for lead(II).** *Journal of Nanoparticle Research* 2012, **14:**1-8.

20. Sung T-W, Lo Y-L: **Highly sensitive and selective sensor based on silica-coated CdSe/ZnS nanoparticles for Cu2+ ion detection.** *Sensors and Actuators B: Chemical* 2012, **165:**119-125.
21. Chao MR, Chang YZ, Chen JL: **Hydrophilic ionic liquid-passivated CdTe quantum dots for mercury ion detection.** *Biosens Bioelectron* 2013, **42:**397-402.
22. Gan TT, Zhang YJ, Zhao NJ, Xiao X, Yin GF, Yu SH, Wang HB, Duan JB, Shi CY, Liu WQ: **Hydrothermal synthetic mercaptopropionic acid stabled CdTe quantum dots as fluorescent probes for detection of Ag(+).** *Spectrochim Acta A Mol Biomol Spectrosc* 2012, **99:**62-68.
23. Gui R, An X, Su H, Shen W, Chen Z, Wang X: **A near-infrared-emitting CdTe/CdS core/shell quantum dots-based OFF-ON fluorescence sensor for highly selective and sensitive detection of Cd2+.** *Talanta* 2012, **94:**257-262.
24. Liu X-Q, Liu Q, Cao S-H, Cai W-P, Weng Y-H, Xie K-X, Li Y-Q: **Directional surface plasmon-coupled emission of CdTe quantum dots and its application in Hg(ii) sensing.** *Analytical Methods* 2012, **4:**3956.
25. Wu H, Liang J, Han H: **A novel method for the determination of Pb2+ based on the quenching of the fluorescence of CdTe quantum dots.** *Microchimica Acta* 2007, **161:**81-86.
26. Wang YQ, Liu Y, He XW, Li WY, Zhang YK: **Highly sensitive synchronous fluorescence determination of mercury (II) based on the denatured ovalbumin coated CdTe QDs.** *Talanta* 2012, **99:**69-74.
27. Koneswaran M, Narayanaswamy R: **l-Cysteine-capped ZnS quantum dots based fluorescence sensor for Cu2+ ion.** *Sensors and Actuators B: Chemical* 2009, **139:**104-109.
28. Ke J, Li X, Shi Y, Zhao Q, Jiang X: **A facile and highly sensitive probe for Hg(II) based on metal-induced aggregation of ZnSe/ZnS quantum dots.** *Nanoscale* 2012, **4:**4996-5001.
29. Link S, El-Sayed MA: **Spectral Properties and Relaxation Dynamics of Surface Plasmon Electronic Oscillations in Gold and Silver Nanodots and Nanorods.** *The Journal of Physical Chemistry B* 1999, **103:**8410-8426.
30. Romo-Herrera JM, Alvarez-Puebla RA, Liz-Marzan LM: **Controlled assembly of plasmonic colloidal nanoparticle clusters.** *Nanoscale* 2011, **3:**1304-1315.
31. Sonntag MD, Klingsporn JM, Zrimsek AB, Sharma B, Ruvuna LK, Van Duyne RP: **Molecular plasmonics for nanoscale spectroscopy.** *Chemical Society Reviews* 2014, **43:**1230-1247.
32. Chen Y-Y, Chang H-T, Shiang Y-C, Hung Y-L, Chiang C-K, Huang C-C: **Colorimetric Assay for Lead Ions Based on the Leaching of Gold Nanoparticles.** *Analytical Chemistry* 2009, **81:**9433-9439.
33. Lee Y-F, Nan F-H, Chen M-J, Wu H-Y, Ho C-W, Chen Y-Y, Huang C-C: **Detection and removal of mercury and lead ions by using gold nanoparticle-based gel membrane.** *Analytical Methods* 2012, **4:**1709.
34. Lok C-N, Ho C-M, Chen R, He Q-Y, Yu W-Y, Sun H, Tam P-H, Chiu J-F, Che C-M: **Silver nanoparticles: partial oxidation and antibacterial activities.** *JBIC Journal of Biological Inorganic Chemistry* 2007, **12:**527-534.
35. Daniel M-C, Astruc D: **Gold nanoparticles: assembly, supramolecular chemistry, quantum-size-related properties, and applications toward biology, catalysis, and nanotechnology.** *Chemical reviews* 2004, **104:**293-346.
36. Wei H, Abtahi SH, Vikesland PJ: **LSPR-based Colorimetric and SERS Sensors for Environmental Analysis.** *ES: Nano* 2015, **In Press**.
37. Hnaiein M, Hassen WM, Abdelghani A, Fournier-Wirth C, Coste J, Bessueille F, Leonard D, Jaffrezic-Renault N: **A conductometric immunosensor based on functionalized magnetite nanoparticles for E. coli detection.** *Electrochemistry Communications* 2008, **10:**1152-1154.
38. Filanovsky B, Markovsky B, Bourenko T, Perkas N, Persky R, Gedanken A, Aurbach D: **Carbon Electrodes Modified with TiO2/Metal Nanoparticles and Their Application for the Detection of Trinitrotoluene.** *Advanced Functional Materials* 2007, **17:**1487-1492.

39. Li H, Li J, Xu Q, Yang Z, Hu X: **A derivative photoelectrochemical sensing platform for 4-nitrophenolate contained organophosphates pesticide based on carboxylated perylene sensitized nano-TiO2.** *Anal Chim Acta* 2013, **766:**47-52.
40. Yang W, Ratinac KR, Ringer SP, Thordarson P, Gooding JJ, Braet F: **Carbon nanomaterials in biosensors: should you use nanotubes or graphene?** *Angew Chem Int Ed Engl* 2010, **49:**2114-2138.
41. Fan H, Li Y, Wu D, Ma H, Mao K, Fan D, Du B, Li H, Wei Q: **Electrochemical bisphenol A sensor based on N-doped graphene sheets.** *Anal Chim Acta* 2012, **711:**24-28.
42. Dong J, Fan X, Qiao F, Ai S, Xin H: **A novel protocol for ultra-trace detection of pesticides: combined electrochemical reduction of Ellman's reagent with acetylcholinesterase inhibition.** *Anal Chim Acta* 2013, **761:**78-83.
43. Kim YA, Lee E-H, Kim K-O, Lee YT, Hammock BD, Lee H-S: **Competitive immunochromatographic assay for the detection of the organophosphorus pesticide chlorpyrifos.** *Analytica chimica acta* 2011, **693:**106-113.
44. Zhao WW, Ma ZY, Yu PP, Dong XY, Xu JJ, Chen HY: **Highly sensitive photoelectrochemical immunoassay with enhanced amplification using horseradish peroxidase induced biocatalytic precipitation on a CdS quantum dots multilayer electrode.** *Anal Chem* 2012, **84:**917-923.
45. Trilling AK, Beekwilder J, Zuilhof H: **Antibody orientation on biosensor surfaces: a minireview.** *Analyst* 2013, **138:**1619-1627.
46. Jiajie L, Hongwu L, Caifeng L, Qiangqiang F, Caihong H, Zhi L, Tianjiu J, Yong T: **Silver nanoparticle enhanced Raman scattering-based lateral flow immunoassays for ultra-sensitive detection of the heavy metal chromium.** *Nanotechnology* 2014, **25:**495501.
47. Liu X, Xiang JJ, Tang Y, Zhang XL, Fu QQ, Zou JH, Lin Y: **Colloidal gold nanoparticle probe-based immunochromatographic assay for the rapid detection of chromium ions in water and serum samples.** *Anal Chim Acta* 2012, **745:**99-105.
48. Li M, Wang Q, Shi X, Hornak LA, Wu N: **Detection of mercury(II) by quantum dot/DNA/gold nanoparticle ensemble based nanosensor via nanometal surface energy transfer.** *Anal Chem* 2011, **83:**7061-7065.
49. Li T, Li B, Wang E, Dong S: **G-quadruplex-based DNAzyme for sensitive mercury detection with the naked eye.** *Chemical Communications* 2009**:**3551-3553.
50. Long F, Zhu A, Shi H, Wang H, Liu J: *Sci Rep* 2013, **3**.
51. Liu M, Wang Z, Zong S, Chen H, Zhu D, Wu L, Hu G, Cui Y: **SERS Detection and Removal of Mercury(II)/Silver(I) using Oligonucleotide-Functionalized Core/Shell Magnetic Silica Sphere@Au Nanoparticles.** *ACS Applied Materials & Interfaces* 2014, **6:**7371-7379.
52. Ma J, Chen Y, Hou Z, Jiang W, Wang L: **Selective and sensitive mercuric (ii) ion detection based on quantum dots and nicking endonuclease assisted signal amplification.** *Biosens Bioelectron* 2013, **43:**84-87.
53. Zhang M, Yin BC, Tan W, Ye BC: **A versatile graphene-based fluorescence "on/off" switch for multiplex detection of various targets.** *Biosens Bioelectron* 2011, **26:**3260-3265.
54. Evtugyn GA, Budnikov HC, Nikolskaya EB: **Sensitivity and selectivity of electrochemical enzyme sensors for inhibitor determination.** *Talanta* 1998, **46:**465-484.
55. Bies C, Lehr CM, Woodley JF: **Lectin-mediated drug targeting: history and applications.** *Adv Drug Deliv Rev* 2004, **56:**425-435.
56. Rhoades RA, Pflanzer RG: *Human Physiology.* Thomson Learning; 2002.
57. Ellington AA, Kullo IJ, Bailey KR, Klee GG: **Antibody-Based Protein Multiplex Platforms: Technical and Operational Challenges.** *Clinical Chemistry* 2010, **56:**186-193.
58. Engvall E, Perlmann P: **Enzyme-Linked Immunosorbent Assay, Elisa.** *III Quantitation of Specific Antibodies by Enzyme-Labeled Anti-Immunoglobulin in Antigen-Coated Tubes* 1972, **109:**129-135.

59. Bordeaux J, Welsh AW, Agarwal S, Killiam E, Baquero MT, Hanna JA, Anagnostou VK, Rimm DL: **Antibody validation.** *BioTechniques* 2010, **48:**197-209.
60. Huang CC, Huang YF, Cao Z, Tan W, Chang HT: **Aptamer-modified gold nanoparticles for colorimetric determination of platelet-derived growth factors and their receptors.** *Anal Chem* 2005, **77:**5735-5741.
61. Evtugyn GA: **Biosensors for Pesticides and Foodborne Pathogens.** In *Portable Biosensing of Food Toxicants and Environmental Pollutants.* CRC Press; 2013: 605-680: *Series in Sensors*].
62. Famulok M, Mayer G: **Aptamer modules as sensors and detectors.** *Acc Chem Res* 2011, **44:**1349-1358.
63. Low SY, Hill JE, Peccia J: **DNA aptamers bind specifically and selectively to (1 → 3)-β-d-glucans.** *Biochemical and Biophysical Research Communications* 2009, **378:**701-705.
64. Hamula CLA, Zhang H, Li F, Wang Z, Chris Le X, Li X-F: **Selection and analytical applications of aptamers binding microbial pathogens.** *TrAC Trends in Analytical Chemistry* 2011, **30:**1587-1597.
65. Stoltenburg R, Reinemann C, Strehlitz B: **SELEX—A (r)evolutionary method to generate high-affinity nucleic acid ligands.** *Biomolecular Engineering* 2007, **24:**381-403.
66. Hoinka J, Berezhnoy A, Dao P, Sauna ZE, Gilboa E, Przytycka TM: **Large scale analysis of the mutational landscape in HT-SELEX improves aptamer discovery.** *Nucleic Acids Research* 2015, **43:**5699-5707.
67. Bănică: **What are Chemical Sensors.** In; 2012
68. Vikesland PJ, Wigginton KR: **Nanomaterial enabled biosensors for pathogen monitoring - a review.** *Environ Sci Technol* 2010, **44:**3656-3669.
69. Bae SW, Tan W, Hong J-I: **Fluorescent dye-doped silica nanoparticles: new tools for bioapplications.** *Chemical Communications* 2012, **48:**2270-2282.
70. Sanvicens N, Pastells C, Pascual N, Marco MP: **Nanoparticle-based biosensors for detection of pathogenic bacteria.** *TrAC Trends in Analytical Chemistry* 2009, **28:**1243-1252.
71. Garcia-Aljaro C, Cella LN, Shirale DJ, Park M, Munoz FJ, Yates MV, Mulchandani A: **Carbon nanotubes-based chemiresistive biosensors for detection of microorganisms.** *Biosens Bioelectron* 2010, **26:**1437-1441.
72. Koets M, van der Wijk T, van Eemeren JTWM, van Amerongen A, Prins MWJ: **Rapid DNA multi-analyte immunoassay on a magneto-resistance biosensor.** *Biosensors and Bioelectronics* 2009, **24:**1893-1898.
73. Kaittanis C, Naser SA, Perez JM: **One-Step, Nanoparticle-Mediated Bacterial Detection with Magnetic Relaxation.** *Nano Letters* 2006, **7:**380-383.
74. Zhang Y, Yang Y, Ma W, Guo J, Lin Y, Wang C: **Uniform Magnetic Core/Shell Microspheres Functionalized with Ni2+–Iminodiacetic Acid for One Step Purification and Immobilization of His-Tagged Enzymes.** *ACS Applied Materials & Interfaces* 2013, **5:**2626-2633.
75. Perez JM, Simeone FJ, Saeki Y, Josephson L, Weissleder R: **Viral-Induced Self-Assembly of Magnetic Nanoparticles Allows the Detection of Viral Particles in Biological Media.** *Journal of the American Chemical Society* 2003, **125:**10192-10193.
76. Liu S, Zheng Z, Li X: **Advances in pesticide biosensors: current status, challenges, and future perspectives.** *Anal Bioanal Chem* 2013, **405:**63-90.
77. Verma N, Bhardwaj A: **Biosensor Technology for Pesticides—A review.** *Applied Biochemistry and Biotechnology* 2015**:**1-27.
78. Pang S, Yang T, He L: **Review of surface enhanced Raman spectroscopic (SERS) detection of synthetic chemical pesticides.** *TrAC Trends in Analytical Chemistry* 2016, **85:**73-82.
79. Fukuto TR: **Mechanism of action of organophosphorus and carbamate insecticides.** *Environmental Health Perspectives* 1990, **87:**245-254.
80. Stenersen J: *Chemical Pesticides Mode of Action and Toxicology.* CRC Press; 2004.

81. Du D, Ye X, Cai J, Liu J, Zhang A: **Acetylcholinesterase biosensor design based on carbon nanotube-encapsulated polypyrrole and polyaniline copolymer for amperometric detection of organophosphates.** *Biosens Bioelectron* 2010, **25:**2503-2508.
82. Amine A, Mohammadi H, Bourais I, Palleschi G: **Enzyme inhibition-based biosensors for food safety and environmental monitoring.** *Biosensors and Bioelectronics* 2006, **21:**1405-1423.
83. Yadavalli VK, Koh W-G, Lazur GJ, Pishko MV: **Microfabricated protein-containing poly(ethylene glycol) hydrogel arrays for biosensing.** *Sensors and Actuators B: Chemical* 2004, **97:**290-297.
84. Nikolelis DP: *Portable Chemical Sensors: Weapons Against Bioterrorism.* Springer Netherlands.
85. Yu G, Wu W, Zhao Q, Wei X, Lu Q: **Efficient immobilization of acetylcholinesterase onto amino functionalized carbon nanotubes for the fabrication of high sensitive organophosphorus pesticides biosensors.** *Biosensors and Bioelectronics* 2015, **68:**288-294.
86. Cui H-F, Wu W-W, Li M-M, Song X, Lv Y, Zhang T-T: **A highly stable acetylcholinesterase biosensor based on chitosan-TiO2-graphene nanocomposites for detection of organophosphate pesticides.** *Biosensors and Bioelectronics* 2018, **99:**223-229.
87. Pang S, Labuza TP, He L: **Development of a single aptamer-based surface enhanced Raman scattering method for rapid detection of multiple pesticides.** *Analyst* 2014, **139:**1895-1901.
88. Zhang C, Wang L, Tu Z, Sun X, He Q, Lei Z, Xu C, Liu Y, Zhang X, Yang J, et al: **Organophosphorus pesticides detection using broad-specific single-stranded DNA based fluorescence polarization aptamer assay.** *Biosensors and Bioelectronics* 2014, **55:**216-219.
89. Laurier KGM, Poets M, Vermoortele F, Cremer GD, Martens JA, Uji-i H, De Vos DE, Hofkens J, Roeffaers MBJ: **Photocatalytic growth of dendritic silver nanostructures as SERS substrates.** *Chemical Communications* 2012, **48:**1559-1561.
90. Nie Y, Teng Y, Li P, Liu W, Shi Q, Zhang Y: **Label-free aptamer-based sensor for specific detection of malathion residues by surface-enhanced Raman scattering.** *Spectrochimica Acta Part A: Molecular and Biomolecular Spectroscopy* 2018, **191:**271-276.
91. Wang LM, Cai J, Wang YL, Fang QK, Wang SY, Cheng Q, Du D, Lin YH, Liu FQ: **A bare-eye-based lateral flow immunoassay based on the use of gold nanoparticles for simultaneous detection of three pesticides.** *Microchimica Acta* 2014, **181:**1565-1572.
92. Jeschke P, Nauen R, Schindler M, Elbert A: **Overview of the Status and Global Strategy for Neonicotinoids.** *Journal of Agricultural and Food Chemistry* 2011, **59:**2897-2908.
93. Simon-Delso N, Amaral-Rogers V, Belzunces LP, Bonmatin JM, Chagnon M, Downs C, Furlan L, Gibbons DW, Giorio C, Girolami V, et al: **Systemic insecticides (neonicotinoids and fipronil): trends, uses, mode of action and metabolites.** *Environmental Science and Pollution Research International* 2015, **22:**5-34.
94. Verdian A: **Apta-nanosensors for detection and quantitative determination of acetamiprid – A pesticide residue in food and environment.** *Talanta* 2018, **176:**456-464.
95. Weerathunge P, Ramanathan R, Shukla R, Sharma TK, Bansal V: **Aptamer-Controlled Reversible Inhibition of Gold Nanozyme Activity for Pesticide Sensing.** *Analytical Chemistry* 2014, **86:**11937-11941.
96. Aviv R: **A valuable reputation.** *The New Yorker* 2014, **10**.
97. Liu X, Li W-J, Li L, Yang Y, Mao L-G, Peng Z: **A label-free electrochemical immunosensor based on gold nanoparticles for direct detection of atrazine.** *Sensors and Actuators B: Chemical* 2014, **191:**408-414.
98. Yılmaz E, Özgür E, Bereli N, Türkmen D, Denizli A: **Plastic antibody based surface plasmon resonance nanosensors for selective atrazine detection.** *Materials Science and Engineering: C* 2017, **73:**603-610.
99. Yang S, Wu T, Zhao X, Li X, Tan W: **The Optical Property of Core-Shell Nanosensors and Detection of Atrazine Based on Localized Surface Plasmon Resonance (LSPR) Sensing.** *Sensors* 2014, **14:**13273.

100. Mohapatra S, Bera MK, Das RK: **Rapid “turn-on” detection of atrazine using highly luminescent N-doped carbon quantum dot.** *Sensors and Actuators B: Chemical* 2018, **263:**459-468.
101. Ullah N, Mansha M, Khan I, Qurashi A: **Nanomaterial-based optical chemical sensors for the detection of heavy metals in water: Recent advances and challenges.** *TrAC Trends in Analytical Chemistry* 2018.
102. Selid P, Xu H, Collins EM, Striped Face-Collins M, Zhao JX: **Sensing Mercury for Biomedical and Environmental Monitoring.** *Sensors* 2009, **9:**5446-5459.
103. Miyake Y, Togashi H, Tashiro M, Yamaguchi H, Oda S, Kudo M, Tanaka Y, Kondo Y, Sawa R, Fujimoto T, et al: **MercuryII-Mediated Formation of Thymine−HgII−Thymine Base Pairs in DNA Duplexes.** *Journal of the American Chemical Society* 2006, **128:**2172-2173.
104. Gao ZF, Song WW, Luo HQ, Li NB: **Detection of mercury ions (II) based on non-cross-linking aggregation of double-stranded DNA modified gold nanoparticles by resonance Rayleigh scattering method.** *Biosensors and Bioelectronics* 2015, **65:**360-365.
105. Ono A, Togashi H: **Highly Selective Oligonucleotide-Based Sensor for Mercury(II) in Aqueous Solutions.** *Angewandte Chemie International Edition* 2004, **43:**4300-4302.
106. Clever GH, Kaul C, Carell T: **DNA--metal base pairs.** *Angew Chem Int Ed Engl* 2007, **46:**6226-6236.
107. Kim Y-R, Mahajan RK, Kim JS, Kim H: **Highly Sensitive Gold Nanoparticle-Based Colorimetric Sensing of Mercury(II) through Simple Ligand Exchange Reaction in Aqueous Media.** *ACS Applied Materials & Interfaces* 2009, **2:**292-295.
108. Xiaorong Y, Huixiang L, Juan X, Xuemei T, He H, Danbi T: **A simple and cost-effective sensing strategy of mercury (II) based on analyte-inhibited aggregation of gold nanoparticles.** *Nanotechnology* 2011, **22:**275503.
109. Huang CC, Chang HT: **Selective gold-nanoparticle-based "turn-on" fluorescent sensors for detection of mercury(II) in aqueous solution.** *Anal Chem* 2006, **78:**8332-8338.
110. Chansuvarn W, Tuntulani T, Imyim A: **Colorimetric detection of mercury(II) based on gold nanoparticles, fluorescent gold nanoclusters and other gold-based nanomaterials.** *TrAC Trends in Analytical Chemistry* 2015, **65:**83-96.
111. Alam A, Ravindran A, Chandran P, Sudheer Khan S: **Highly selective colorimetric detection and estimation of Hg2+ at nano-molar concentration by silver nanoparticles in the presence of glutathione.** *Spectrochimica Acta Part A: Molecular and Biomolecular Spectroscopy* 2015, **137:**503-508.
112. Goyer RA: **Lead toxicity: from overt to subclinical to subtle health effects.** *Environmental Health Perspectives* 1990, **86:**177-181.
113. Kim H-K, Liu J, Li J, Nagraj N, Li M, Pavot CMB, Lu Y: **Metal-Dependent Global Folding and Activity of the 8-17 DNAzyme Studied by Fluorescence Resonance Energy Transfer.** *Journal of the American Chemical Society* 2007, **129:**6896-6902.
114. Tang S, Tong P, Li H, Tang J, Zhang L: **Ultrasensitive electrochemical detection of Pb(2)(+) based on rolling circle amplification and quantum dots tagging.** *Biosens Bioelectron* 2013, **42:**608-611.
115. Li T, Wang E, Dong S: **Lead(II)-Induced Allosteric G-Quadruplex DNAzyme as a Colorimetric and Chemiluminescence Sensor for Highly Sensitive and Selective Pb2+ Detection.** *Analytical Chemistry* 2010, **82:**1515-1520.
116. Gao C, Yu XY, Xu RX, Liu JH, Huang XJ: **AlOOH-reduced graphene oxide nanocomposites: one-pot hydrothermal synthesis and their enhanced electrochemical activity for heavy metal ions.** *ACS Appl Mater Interfaces* 2012, **4:**4672-4682.
117. Gui R, An X, Huang W: **An improved method for ratiometric fluorescence detection of pH and Cd2+ using fluorescein isothiocyanate-quantum dots conjugates.** *Anal Chim Acta* 2013, **767:**134-140.

118. Sun D, Xie X, Cai Y, Zhang H, Wu K: **Voltammetric determination of Cd2+ based on the bifunctionality of single-walled carbon nanotubes-Nafion film.** *Anal Chim Acta* 2007, **581:**27-31.
119. Toghill KE, Xiao L, Wildgoose GG, Compton RG: **Electroanalytical Determination of Cadmium(II) and Lead(II) Using an Antimony Nanoparticle Modified Boron-Doped Diamond Electrode.** *Electroanalysis* 2009, **21:**1113-1118.
120. Beer KD, Gargano JW, Roberts VA, Hill VR, Garrison LE, Kutty PK, Hilborn ED, Wade TJ, Fullerton KE, Yoder JS: **Surveillance for Waterborne Disease Outbreaks Associated with Drinking Water-United States, 2011-2012.** *MMWR Morbidity and mortality weekly report* 2015, **64:**842-848.
121. Organization WH: **WHO publishes list of bacteria for which new antibiotics are urgently needed.** *WHO: Geneva, Switzerland* 2017.
122. Kumar N, Hu Y, Singh S, Mizaikoff B: **Emerging biosensor platforms for the assessment of water-borne pathogens.** *Analyst* 2018, **143:**359-373.
123. Mocan T, Matea CT, Pop T, Mosteanu O, Buzoianu AD, Puia C, Iancu C, Mocan L: **Development of nanoparticle-based optical sensors for pathogenic bacterial detection.** *J Nanobiotechnology* 2017, **15:**25.
124. Ali M, Nelson AR, Lopez AL, Sack DA: **Updated Global Burden of Cholera in Endemic Countries.** *PLoS Neglected Tropical Diseases* 2015, **9:**e0003832.
125. Finkelstein RA: **Cholera, Vibrio cholerae O1 and O139, and other pathogenic vibrios.** 1996.
126. Yu CY, Ang GY, Chua AL, Tan EH, Lee SY, Falero-Diaz G, Otero O, Rodríguez I, Reyes F, Acosta A, et al: **Dry-reagent gold nanoparticle-based lateral flow biosensor for the simultaneous detection of Vibrio cholerae serogroups O1 and O139.** *Journal of Microbiological Methods* 2011, **86:**277-282.
127. Tam PD, Thang CX: **Label-free electrochemical immunosensor based on cerium oxide nanowires for Vibrio cholerae O1 detection.** *Materials Science and Engineering: C* 2016, **58:**953-959.
128. Ahn K-S, Lim KR, Jeong D, Lee BY, Kim KS, Lee W-Y: **Fluorescence energy transfer inhibition bioassay for cholera toxin based on galactose-stabilized gold nanoparticles and amine-terminated quantum dots.** *Microchemical Journal* 2016, **124:**9-14.
129. Khan SA, DeGrasse JA, Yakes BJ, Croley TR: **Rapid and sensitive detection of cholera toxin using gold nanoparticle-based simple colorimetric and dynamic light scattering assay.** *Analytica Chimica Acta* 2015, **892:**167-174.
130. Zhang C-H, Liu L-W, Liang P, Tang L-J, Yu R-Q, Jiang J-H: **Plasmon Coupling Enhanced Raman Scattering Nanobeacon for Single-Step, Ultrasensitive Detection of Cholera Toxin.** *Analytical Chemistry* 2016, **88:**7447-7452.
131. Goldman ER, Clapp AR, Anderson GP, Uyeda HT, Mauro JM, Medintz IL, Mattoussi H: **Multiplexed toxin analysis using four colors of quantum dot fluororeagents.** *Anal Chem* 2004, **76:**684-688.
132. Schofield CL, Field RA, Russell DA: **Glyconanoparticles for the Colorimetric Detection of Cholera Toxin.** *Analytical Chemistry* 2007, **79:**1356-1361.
133. Azarian T, Ali A, Johnson JA, Jubair M, Cella E, Ciccozzi M, Nolan DJ, Farmerie W, Rashid MH, Sinha-Ray S, et al: **Non-toxigenic environmental Vibrio cholerae O1 strain from Haiti provides evidence of pre-pandemic cholera in Hispaniola.** *Scientific Reports* 2016, **6:**36115.
134. Martín M, Salazar P, Jiménez C, Lecuona M, Ramos MJ, Ode J, Alcoba J, Roche R, Villalonga R, Campuzano S, et al: **Rapid Legionella pneumophila determination based on a disposable core–shell Fe3O4@poly(dopamine) magnetic nanoparticles immunoplatform.** *Analytica Chimica Acta* 2015, **887:**51-58.

135. Park J, You X, Jang Y, Nam Y, Kim MJ, Min NK, Pak JJ: **ZnO nanorod matrix based electrochemical immunosensors for sensitivity enhanced detection of Legionella pneumophila.** *Sensors and Actuators B: Chemical* 2014, **200:**173-180.
136. Wu T-Y, Su Y-Y, Shu W-H, Mercado AT, Wang S-K, Hsu L-Y, Tsai Y-F, Chen C-Y: **A novel sensitive pathogen detection system based on Microbead Quantum Dot System.** *Biosensors and Bioelectronics* 2016, **78:**37-44.
137. Foudeh AM, Daoud JT, Faucher SP, Veres T, Tabrizian M: **Sub-femtomole detection of 16s rRNA from Legionella pneumophila using surface plasmon resonance imaging.** *Biosensors and Bioelectronics* 2014, **52:**129-135.
138. Falkinham III JO, Hilborn ED, Arduino MJ, Pruden A, Edwards MA: **Epidemiology and ecology of opportunistic premise plumbing pathogens: Legionella pneumophila, Mycobacterium avium, and Pseudomonas aeruginosa.** *Environmental health perspectives* 2015, **123:**749.
139. Yoo SM, Kim D-K, Lee SY: **Aptamer-functionalized localized surface plasmon resonance sensor for the multiplexed detection of different bacterial species.** *Talanta* 2015, **132:**112-117.
140. Jia F, Xu L, Yan W, Wu W, Yu Q, Tian X, Dai R, Li X: **A magnetic relaxation switch aptasensor for the rapid detection of Pseudomonas aeruginosa using superparamagnetic nanoparticles.** *Microchimica Acta* 2017, **184:**1539-1545.
141. Krithiga N, Viswanath KB, Vasantha VS, Jayachitra A: **Specific and selective electrochemical immunoassay for Pseudomonas aeruginosa based on pectin–gold nano composite.** *Biosensors and Bioelectronics* 2016, **79:**121-129.
142. He Y, Wang M, Fan E, Ouyang H, Yue H, Su X, Liao G, Wang L, Lu S, Fu Z: **Highly Specific Bacteriophage-Affinity Strategy for Rapid Separation and Sensitive Detection of Viable Pseudomonas aeruginosa.** *Analytical Chemistry* 2017, **89:**1916-1921.
143. Ellairaja S, Krithiga N, Ponmariappan S, Vasantha VS: **Novel Pyrimidine Tagged Silver Nanoparticle Based Fluorescent Immunoassay for the Detection of Pseudomonas aeruginosa.** *Journal of Agricultural and Food Chemistry* 2017, **65:**1802-1812.
144. Wang K-Y, Zeng Y-L, Yang X-Y, Li W-B, Lan X-P: **Utility of aptamer-fluorescence in situ hybridization for rapid detection of Pseudomonas aeruginosa.** *European Journal of Clinical Microbiology & Infectious Diseases* 2011, **30:**273-278.

Chapter 3 Raman Spectroscopic Investigation of Poly (butylene adipate-co-terephthalate) Polymers

3.1 Abstract

The accumulation of persistent polymers in aqueous and terrestrial systems is increasingly recognized as a major environmental threat. One strategy to mitigate further accumulation is to embrace the use of biodegradable polymers, many of which are already commercially available. Numerous end-of-life options exist for biodegradable polyesters ranging from composting and depolymerization for monomer recycling to biodegradation in the soil following agricultural application. In many cases, the hydrolysis of ester bonds in the polyester is considered to be the rate-limiting step in the overall biodegradation process. However, the specific mechanisms of hydrolysis remain an area of active research. Recent work suggested that the chemical structure of biodegradable polymers plays a key role in determining hydrolysis. In this contribution, we characterize a suite of polymers using the finger print technique of Raman spectroscopy. This technique is sensitive to both the chemical structure and the orientation of the molecules in a given chemical bond. Six aliphatic-aromatic copolyesters of poly(butylene adipate-co-terephthalate) (PBAT), with increasing aromatic content were studied in both bulk pellet form and as thin films. Principal component analysis (PCA) was used to demonstrate that the diversification of polyesters bonds, which accompanies the increase in aromatic polyester, could be identified using Raman spectroscopy. Additionally, we performed the first assignment of the Raman structure of PBAT in the low wavenumber, sub 1600 cm^{-1}, region.

3.2 Introduction

The accumulation of persistent polymers in aqueous and terrestrial systems is increasingly recognized as a major environmental threat[1-3]. One strategy to mitigate further accumulation is to embrace the use of biodegradable polymers. Of particular interest are aliphatic-aromatic copolyesters-synthesized from aliphatic and aromatic dicarboxylic acids and aliphatic diols because their physicochemical properties can

be adjusted by changing the ratio of aliphatic to aromatic diacid components. Numerous end-of-life options exist for biodegradable polyesters from composting and depolymerization for monomer recycling to biodegradation in the soil in agricultural applications. In all of these cases, the hydrolysis of ester bonds in the polyester is considered to be the rate-limiting step in the overall biodegradation process[4]. The pioneering work of Tokiwa et al. demonstrated that extracellular microbial carboxylesterases catalyze the hydrolysis of synthetic polyesters,[5] but the specific mechanisms of hydrolysis remain an area of active research.

In our previous studies, we introduced two complementary approaches to monitor hydrolysis: a high-throughput microplate method that is based on monitoring the co-hydrolysis of a fluorogenic ester probe embedded into the polyester[6] and an approach based on quartz-crystal microbalance with dissipation monitoring (QCM-D) that allows real-time monitoring of the hydrolytic mass loss from polyester thin films[7]. The QCM-D technique was then employed to show that the physicochemical and structural properties of both the polyester, poly(butylene adipate-co-terephthalate) (PBAT), and the carboxylesterase determine the rate and extent of enzymatic polyester hydrolysis[8]. However, complementary methods must be employed to determine which of the structural properties play a key role in the hydrolysis.

Raman spectroscopy is an ideal method for observing the chemical structure and local environment of individual polyester bonds. The inelastic scattering measured via Raman spectroscopy is sensitive to both the chemical structure and the orientation of the molecules in a given chemical bond and has been extensively used to distinguish and characterize polymers. With regards to PBAT characterization, Cai et. al[9] used Raman to distinguish PBAT from the polymer it aims to replace, poly(ethylene terephthalate) (PET). Chen et. al[10] used Raman spectroscopy to study blends of biodegradable polymers containing PBAT. Herein we were interested in studying different blends of PBAT in order to understand the origin of the polyester peaks observed in the Raman signal. Specifically, we studied six different blends of PBAT, with varying ratios of aromatic (i.e., terephthalate) to aliphatic (i.e., adipate) content. The naming convention for the samples is PBATx with x denoting the percentage of aromatic content. First the bulk samples were characterized and the intra-sample variation explored using principal component analysis (PCA). Next,

thin-films of the polymers were produced and studied because they closely mimic commercially available PBAT products. Finally, we compare the Raman spectra collected from solid polymers to that from spin-coated samples to determine if spin-coating leads to a significant change in polymer ordering.

3.3 Materials and Methods

3.3.1 Chemicals

Anhydrous chloroform (≥99%) and standard 25 mm by 75 mm glass microscope slides were purchased from Sigma-Aldrich. Aluminum foil was purchased from a Kroger supermarket.

3.3.2 Polyesters

Table 3-1 shows the general chemical structure and physicochemical properties of the studied aliphatic-aromatic copolyesters (PBATx). Each of the polyester samples were provided by BASF SE and were synthesized as previously described. All of the aliphatic-aromatic copolyesters contained butanediol (B)

Table 3-1: Generalized Structural Formula and Key Physicochemical Properties of the Studied Aliphatic Polyesters[a].

Aliphatic-aromatic co-polyester (PBATx)				
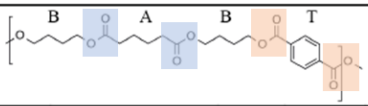				
Abbreviation	Fraction (%) of aromatic diacids (T/(A+T)) • 100	T_m (°C)	M_n (g/mol)	M_w (g/mol)
PBAT0	0	58.7	19800	52100
PBAT10	9.6	49.1	15600	51000
PBAT20	19.6	43.2	18400	56000
PBAT29	29.0	58.0	15900	48400
PBAT42	42.0	101.0	17600	52200
PBAT50	50.1	126.0	18300	56100

[a]T_m, M_n, M_w, and n refer to the melting temperature, the number average molecular weight, the weight average molecular weight, and the number of carbon atoms in the diacid component in the polyester, respectively.

but were synthesized to have varying relative amounts of terephthalate (T) to adipate (A). As shown in Equation 3-1, this ratio is expressed as the molar fraction of terephthalate to total diacid x (%):

$$x = T/(T + A) \cdot 100 \qquad \text{Equation 3-1}$$

3.3.3 Formation of polyester thin films

Polyester thin films were prepared by spin coating. Samples were dissolved in chloroform (10% (w/w)) and a 3 µL aliquot was pipetted onto an aluminum foil covered glass slide spinning at 4000 rpm. The samples were spun for 1 minute using a WS-400B-6NPP/LITE (Laurell Technologies) spin coater.

3.3.4 Raman Instrumentation

A WITec Alpha 300R confocal microscope (WITec, Ulm, Germany) employing a 785 nm wavelength excitation laser and a 300 g/mm grating with a 10× objective (0.3 N.A.) was used to collect Raman spectra. A collection time of 0.5 seconds and a step size of 1.6 µm/pixel was used for all samples. Spectra were collected from five distinct regions on each sample for a total of 3,125 spectra per sample.

3.3.5 Data Analysis

Raw Raman spectra were imported into Matlab and preprocessed using in house algorithms[11-13]. In brief, the spectra were baseline corrected and then the location of the polyester peak was determined by searching within a wavenumber range of interest for the most intense peak. The processed spectra were then scaled, the minimum and maximum intensity set between 0 and 1, and principal component analysis (PCA) was performed using a slight modification of the spectral analysis platform of Goodacre et al[14].

3.4 Results and Discussion

A detailed spectroscopic study of PBAT was conducted in order to identify the Raman peaks that changed, developed, or shifted in wavenumber with an increase in T content. In addition to altering the aromatic content in the polymers, bulk samples were compared to spin coated thin films. Thin-films serve as better mimics of plastic products (i.e., plastic bags) than bulk pellets and they are often used, such as in QCM-D measurements, to access nanoscale phenomena. For all six PBAT samples, a piece of the bulk sample was cut off and dissolved in 10% (w/w) chloroform solution that was used to spin coat aluminum foil. Five maps, each with 625 spectra, were collected from every sample as illustrated in **Figure 3.1**. An

average spectrum was calculated for each map, before baseline correction, and the map averages were averaged to generate a reference spectrum for each sample.

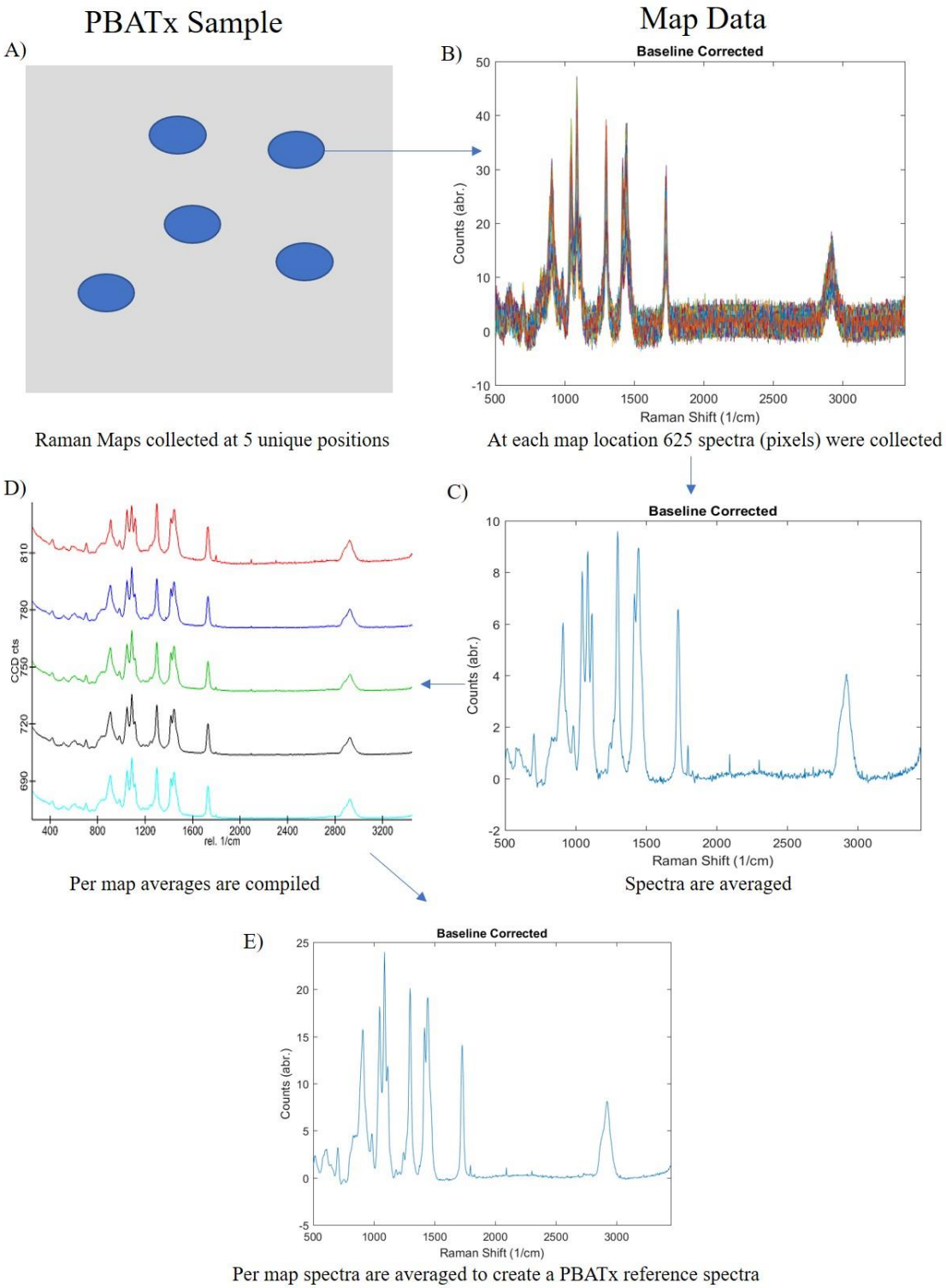

Figure 3.1. Data collection and processing workflow. Maps of 40µm by 40µm are collected from five unique locations on each sample (A). The 625 spectra collected from each map are baseline corrected and manipulation of this data is termed per pixel (B). An average spectrum is generated for each map (C) and the per map averages from each PBATx sample are compiled (D). The per map averages are averaged to generate a per sample reference spectrum (E).

3.4.1 Peaks of Interests

Previous efforts to characterize PBAT via Raman spectroscopy have focused on the differentiation of PBAT from other polymers. Chen et al. used the 1600 cm^{-1} benzene ring stretch, to distinguish PBAT from the biodegradable polymers poly(lactic acid) (PLA) and poly(propylene carbonate) (PPC)[10]. In contrast, Cai et al. investigated the Raman spectra of PBAT and poly(ethylene terephthalate) (PET) and found only slight differences in the spectra[9]. In these prior efforts, the molar fraction of terephthalate (T) to total diacid (T + adipate (A)), was not considered and was likely unknown. Herein, systematic study of the Raman spectra of PBAT enables identification of key Raman bands that change in intensity or location as a function of an increase in terephthalate content (Figure 3.2A). Our assignment of the aromatic ring stretch (C=C) at 1609 cm^{-1} and the polyester stretch (C=O) in the 1713-1726 cm^{-1} spectral range is consistent with Chen, Cai and the literature[15-19].

Polyester hydrolysis is believed to be the rate limiting step in PBAT biodegradation. Therefore, we were specifically interested in understanding the polyester stretches in the Raman spectra. Raman spectroscopy is uniquely suited to detect differences between the aliphatic esters and aryl esters because it is sensitive to differences in molecular and lattice vibrations. As evident in Figure 3.2B, the location of the polyester peak at 1726 cm^{-1} shifts to lower wavenumbers as the T content of the PBAT increases. This result reflects the increasing number of polyesters adjacent to the aromatic ring. Aryl esters withdraw electrons away from the aromatic structure leading to a change in the molecular vibration compared to the aliphatic esters. The shift in the C=O polyester peak position, due to the increasing number of aryl esters, is shown in **Figure 3.2C** by comparing the position to the polymer containing only aliphatic esters (PBAT00). Additional, contributions of the polyester structure to the Raman spectra can be found at ~1273 cm^{-1}, the C-O stretch, and 1442 cm^{-1}, methyl group symmetric stretch next to electronegative atom.

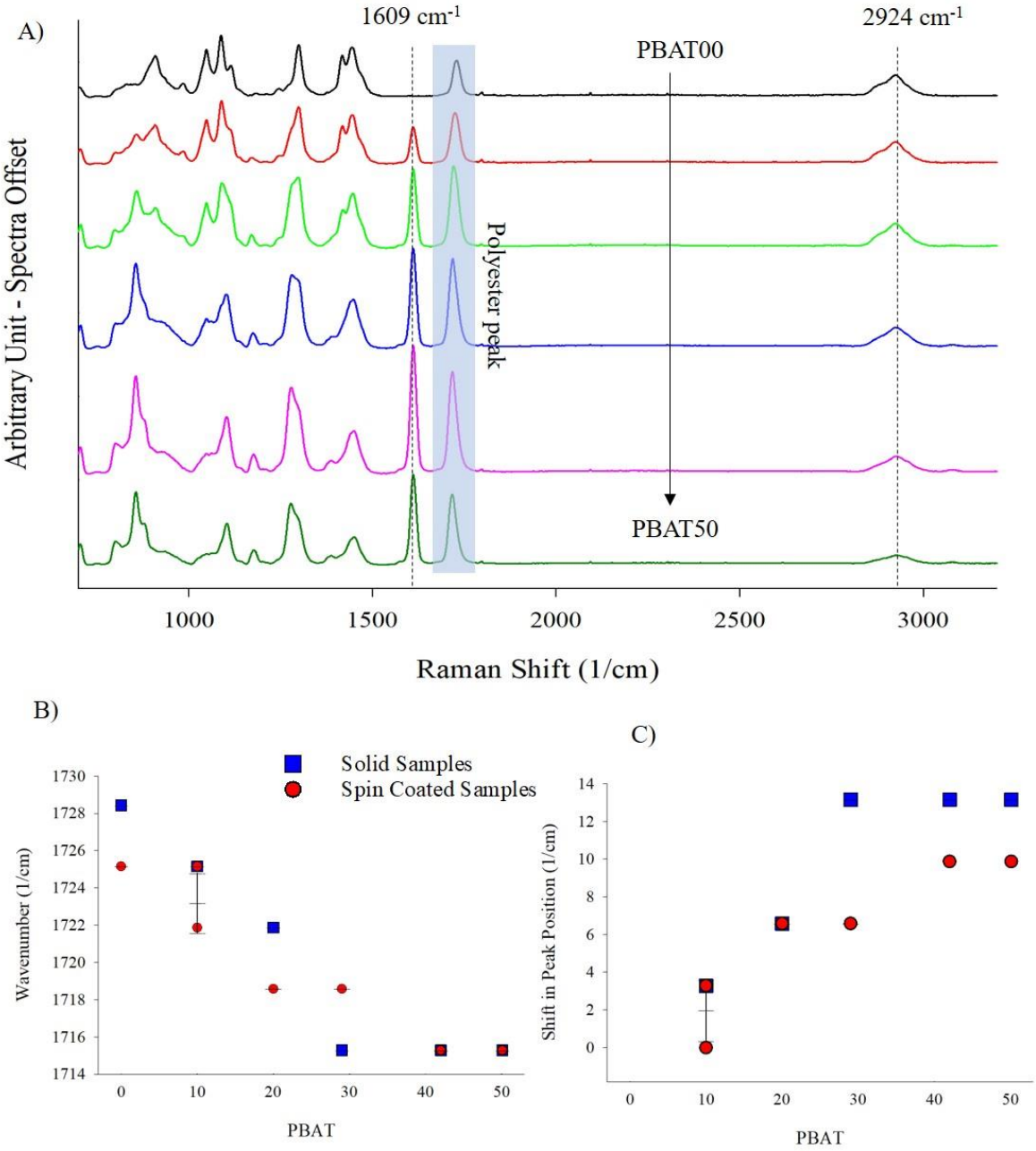

Figure 3.2. Baseline corrected Raman PBAT spectra with molar fraction increasing from 0% to 50%. Spectra were collected with a 785nm laser and are offset for ease of interpretation (A). Location, wavenumber, of the polyester peak as a function of PBAT (B) and shift in the polyester peak as compared to the PBAT00 sample (C). The mean and one standard deviation are plotted for all samples; only PBAT10 exhibited significant variation.

PCA was employed to better identify the features in the PBAT spectra that strongly or subtly vary with T content. In PCA, an orthogonal transformation is used to generate new variables, principal components, that capture the maximum variance in the data[20]. The weighting, or importance, of each wavenumber relative to any given principal component is shown in the loading plot (**Figure 3.2**A) and the distance between the samples can be visualized in the scores plot (**Figure 3.2**B). Only the score plot showing principal components (PCs) 1 and 2 is presented because these two components explain the majority of the variance, 82% and 99% respectively. The PCA results shown in **Figure 3.2**A & **3.2**B were collected using the reference spectra collected from the PBAT solid samples. The assignment of the key peaks in the loadings plot are listed in **Figure 3.2**C and can be associated with the ring structure of the terephthalate (purple), the polyester (orange), or the aliphatic backbone (green). Assigning the Raman peaks in the region below 1600 cm^{-1} is complex because many of the peaks arise from carbon-carbon bonds in the aliphatic backbone and, as a random copolymer, PBAT contains aliphatic chains of various lengths. **Figure 3.2**C presents the first comprehensive, albeit tentative, assignment of the peaks in the PBAT Raman spectra.

A)

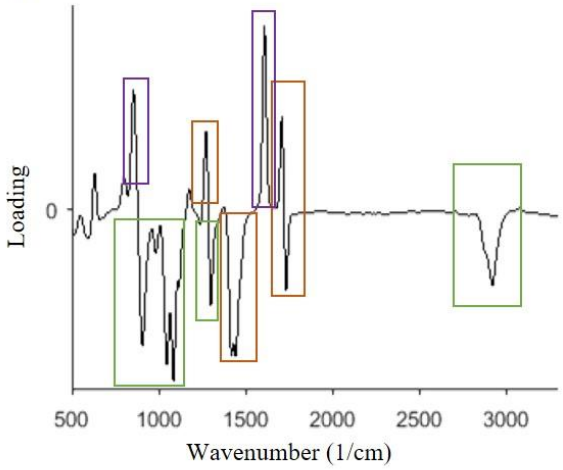

B)

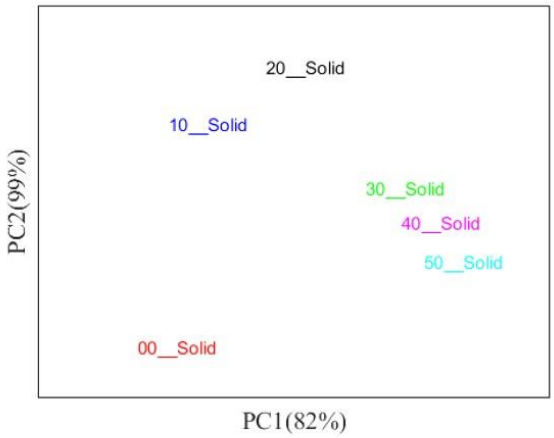

C)

Peak Range (cm^{-1})	Stretch	Assignment
857	Strong out-of-plane deformation characteristic of para-disubstituted	Benzene Ring
1609	C-C	
1273	C-O stretch from alkyl esters	Polyesters
1442	Methyl group symmetric stretch next to electronegative atom ($O-CH_3$)	
1715/1726	C=O stretch	
2924	Antisymmetric $C-H_2$	Aliphatic Backbone
1047	Various CCCC	
1084	Antisymmetrical CCC	
907	Symmetrical CCC	
1302	$-(CH_2)_n-$ in-phase twisting	
1422	CH_2 Bending – rocking/bending/twisting	

Figure 3.3. Results from PCA performed on reference Raman spectra from solid PBAT samples. The loadings plot with peaks of interest are outlined (A). Scores plot of the data showing principal component 2 (PC2) vs. principal component 1 (PC1) with explained variance contained in the axis labels. Each PBAT sample is depicted using a unique color (B). The color-coded table containing the key Raman peaks as determined from the loadings plot (A) with proposed assignments (C).

3.4.2 Point-to-Point Variability

With any sample, especially a random co-polymer, there is an interest in determining the homogeneity of the material. Understanding the importance of intra-sample variability compared to inter-sample variability was especially important for this experiment where subtle changes in the Raman spectra will ultimately be used to understand the role of the aliphatic and aromatic subunits in enzymatic hydrolysis. As noted in **Figure 3.1**, five Raman maps, each 40 µm by 40 µm, were collected from every PBATx sample. All the spectra, 3,125 in total for each sample, were averaged together to create the reference spectra shown in **Figure 3.2**A and these reference spectra were used for the PCA analysis shown in **Figure 3.3**B.

The first step to identifying heterogeneities was to compare the average spectra from each map location using PCA. **Figure 3.4**A shows the resulting PCA scores plot and that although there is a small amount of variation between the different map locations, the PBATx-to-PBATx variation is the most significant. Breaking the data down even further, PCA was performed on all the data points collected and the scores plot is shown in **Figure 3.4**B. The separation between the samples is again obvious and it is also apparent that there is significant variation in the PBAT00 data, shown in red. Replotting only the PBAT00 data, **Figure 3.4**C, and representing each map in a unique color, it can easily be identified that all the variation in the sample is arising from a single map shown in purple. To better understand the intrasample variation of PBAT00, the sample was analyzed on its own and the scores plot is shown in **Figure 3.4**D with the same color-coding as **Figure 3.4**C. The difference between map E, shown in purple, and the other four maps is a strong function of PC1 because the samples are separated in the x-ordinate. The loadings graph, **Figure 3.4**D inset, shows that the stretch around 1000 cm^{-1} is a major contributor to the separation in PC1 and looking at the scaled spectra, Figure 3E, the peak around 1000 cm^{-1} is nosiest in map E. The traces in **Figure 3.4**E show all the Raman spectra collected from the PBAT00 and were the input data for the PCA algorithm. To identify the origin of the noise it is best to look at the baseline corrected unscaled data and it can be seen from **Figure 3.4**F that the average signal intensity in map E was two to four times less than the other four maps. The findings suggested that: i) a signal-to-noise filter should be applied before using PCA to analyze

Raman the per pixel data; ii) the point-to-point variability is a function of intensity and not of spectral differences.

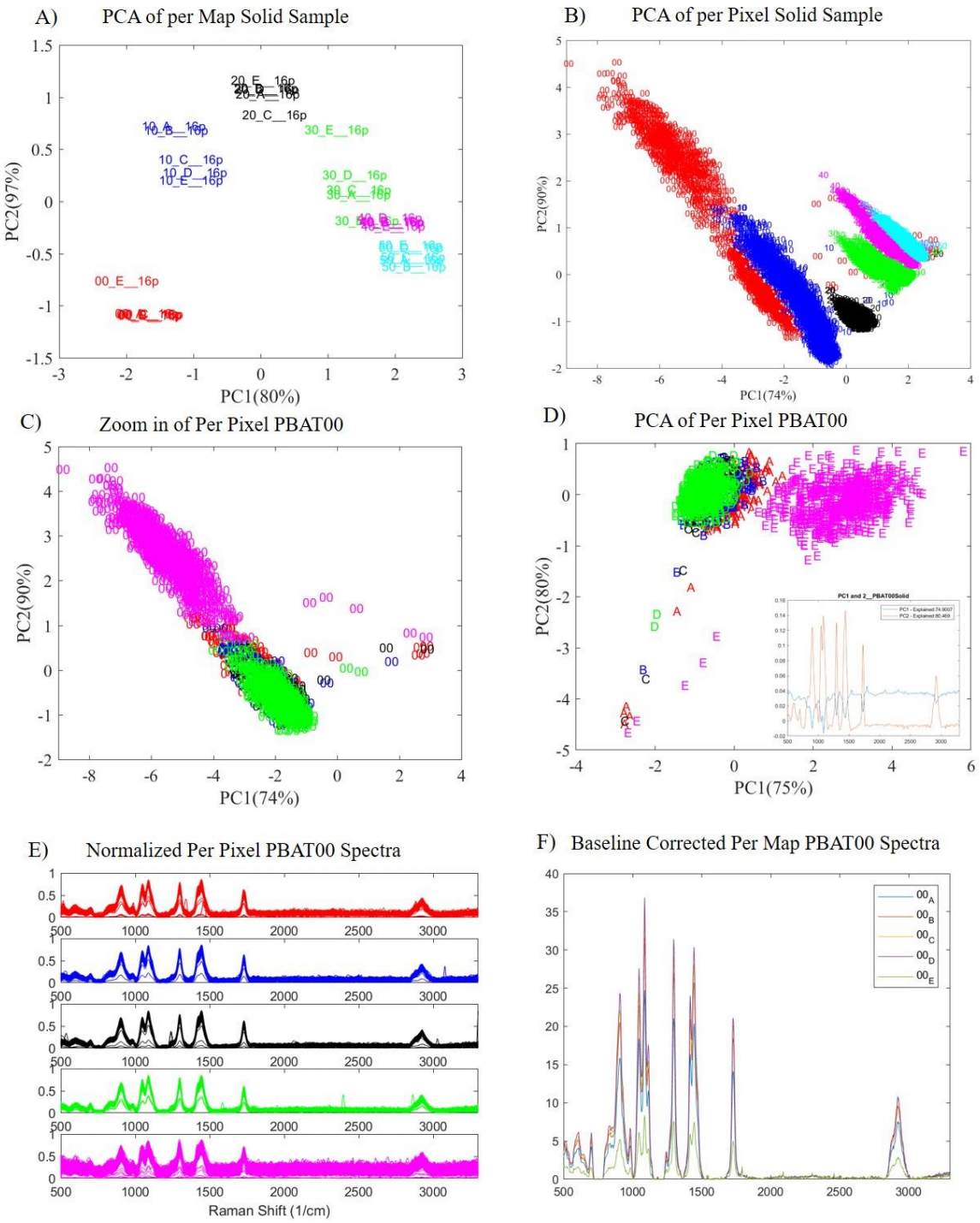

Figure 3.4. Results from the PCA performed on the per map Raman spectra from solid PBATx samples with each PBATx sample in a unique color (A). PCA performed on the per pixel solid PBATx data; color coding matches that of the per map and per sample PCA (B). Zoom in of the PBAT00 data from the per pixel PCA (B) with the pixel data from each map shown in a unique color (C). The results of a PCA performed only on the per pixel PBAT00 data with a color scheme matching (C) and an inset showing the principal components (D). The normalized per pixel traces of PBAT00 separated by map (E). The baseline corrected per map averages of PBAT00 (F).

3.4.3 Spin coating

Polymer thin-films are often employed to study the mechanisms of hydrolysis because degradation of the polymer occurs at the material surface and thin-films contain polymeric content analogues to real-world samples. Films can be prepared by a number of routes such as spin-coating, dip-coating and flow coating, with spin-coating being the most commonly employed method for planar substances because of the excellent control over lateral and vertical polymer distribution[21]. Thin-films were prepared from each PBATx sample using a 10% (w/w) digestion in chloroform. As with the solid samples, five maps were collected from each sample for a total of 3,125 spectra per sample.

Baseline corrected reference spectra for the spin coated samples are depicted in **Figure 3.5**A. The PCA scores plot for this data is shown in **Figure 3.5**B and shows a good separation between the PBATx samples. Comparing the reference spectra for the spin-coated and solid samples, **Figure 3.5**C, the PCA scores plot shows that the PBATx samples separate along PC1 and within each pair the spin coated samples are separated from the solid samples along PC2. The loadings plot, **Figure 3.5**D, show that PC1 arises from PBATx-to-PBATx differences because there are loadings in the negative and positive directions with jump at ~1720 cm^{-1}, the location of the polyester peak. PC2 looks very similar to the traces in **Figure 3.5**A, suggesting that the differences in PC2 arise from variation in spectra intensity. In **Figure 3.5**E and 3.5F, the per map averages for the spin coated and solid samples are plotted with **Figure 3.5**E showing each PBATx in a unique color and **Figure 3.5**F showing the spin coated samples in blue and solid samples in red. The overlap of the PBAT30 solid sample with the PBAT40 and PBAT50 samples further supports the importance of the shift in the polyester peak. Looking at **Figure 3.2**B, the polyester stretch for all five samples is found at 1715 cm^{-1} whereas the peak for PBAT30 spin coated samples is found at 1718 cm^{-1}. The separation of the high aromatic content samples from the more aliphatic rich samples is dominated by the backbone stretches at ~1000 cm^{-1}, which can be seen in the loadings plot, **Figure 3.5**D. The variation in this region can also be seen in the reference spectra traces, **Figure 3.5**A, where a triplet peak is seen in

PBAT00 and the CCC symmetrical stretch at 907 cm^{-1} morphs into a single peak with a shoulder at 1084 cm^{-1}, indicating the presence of asymmetrical CCC stretching.

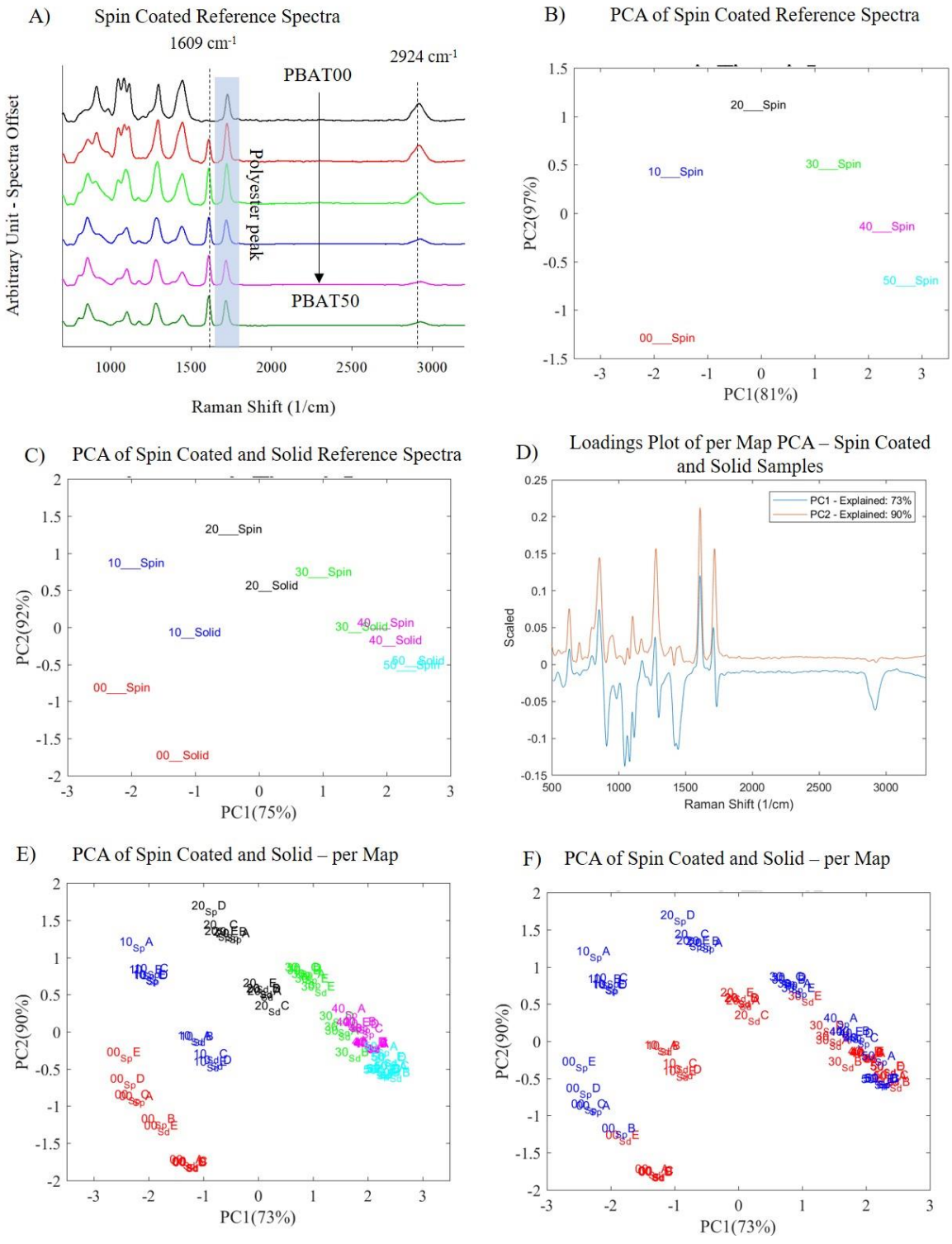

Figure 3.5. Baseline corrected Raman PBATx reference spectra from spin coated samples (A). Scores plot from PCA of the spin coated reference spectra each PBATx sample in a unique color (B). PCA analysis of the spin coated and solid references spectra (C). Loadings plot from the combine spin coated and solid per map PCA shown in the bottom two panels (D). Scores plot from the combined PCA of the spin coated and solid per map samples with each PBATx sample in a unique color (E). The per map data shown in panel E but re-colored to show the spin coated samples in blue and solid samples in red (F).

3.5 Conclusions

In this paper, we present the first systematic Raman spectroscopy study of PBAT. Six samples of an aliphatic-aromatic copolyester with varying aromatic content were studied in both bulk pellets and as spin coated thin-films. Using PCA, key peaks that varied as a function of aromatic content were identified and the first tentative assignment of PBAT stretches at wavenumbers less than 1600cm^{-1} was performed. PCA could be used to accurately discern the PBATx samples from one another at the pixel, map and sample level. The pixel data suggests that point-to-point variation is dominated by differences in signal intensity opposed to structural differences. The map and sample level data were used to compare the bulk solid samples with the thin films and the PCA was again able to differentiate between the PBATx samples. The spin-coated samples and bulk samples for each PBATx pair could be distinguished from each other based on signal intensity. The combined PCA also demonstrated the importance of the low wavenumber aliphatic backbone stretches in distinguishing the samples with low aromatic, <30%, and high aromatic content.

3.6 References

1. Rillig, M. C., Microplastic in Terrestrial Ecosystems and the Soil? *Environmental science & technology* **2012,** *46*, (12), 6453-6454.
2. Browne, M. A.; Crump, P.; Niven, S. J.; Teuten, E.; Tonkin, A.; Galloway, T.; Thompson, R., Accumulation of Microplastic on Shorelines Woldwide: Sources and Sinks. *Environmental science & technology* **2011,** *45*, (21), 9175-9179.
3. Thompson, R. C.; Olsen, Y.; Mitchell, R. P.; Davis, A.; Rowland, S. J.; John, A. W. G.; McGonigle, D.; Russell, A. E., Lost at Sea: Where Is All the Plastic? *Science* **2004,** *304*, (5672), 838-838.
4. Mueller, R.-J., Biological degradation of synthetic polyesters—Enzymes as potential catalysts for polyester recycling. *Process Biochemistry* **2006,** *41*, (10), 2124-2128.
5. Tokiwa, Y.; Suzuki, T., Hydrolysis of polyesters by lipases. *Nature* **1977,** *270*, 76.
6. Zumstein, M. T.; Kohler, H.-P. E.; McNeill, K.; Sander, M., High-Throughput Analysis of Enzymatic Hydrolysis of Biodegradable Polyesters by Monitoring Cohydrolysis of a Polyester-Embedded Fluorogenic Probe. *Environmental science & technology* **2017**.
7. Zumstein, M. T.; Kohler, H.-P. E.; McNeill, K.; Sander, M., Enzymatic Hydrolysis of Polyester Thin Films: Real-Time Analysis of Film Mass Changes and Dissipation Dynamics. *Environmental science & technology* **2016,** *50*, (1), 197-206.
8. Zumstein, M. T.; Rechsteiner, D.; Roduner, N.; Perz, V.; Ribitsch, D.; Guebitz, G. M.; Kohler, H.-P. E.; McNeill, K.; Sander, M., Enzymatic Hydrolysis of Polyester Thin Films at the Nanoscale: Effects of Polyester Structure and Enzyme Active-Site Accessibility. *Environmental science & technology* **2017,** *51*, (13), 7476-7485.
9. Cai, Y.; Lv, J.; Feng, J.; Liu, Y.; Wang, Z.; Zhao, M.; Shi, R., Discrimination of Poly(butylenes adipate-co-terephthalate) and Poly(ethylene terephthalate) with Fourier Transform Infrared Microscope and Raman Spectroscope. *Spectroscopy Letters* **2012,** *45*, (4), 280-284.
10. Chen, R.; Huang, X.; Wang, M.; Jin, G., Evaluation and comparison of mid-infrared, Raman and near-infrared spectroscopies for characterization and determination of the compositions in fully biodegradable poly(lactic acid)/poly(propylene carbonate)/poly(butylene adipate-co-terephthalate) blends combined with chemometrics. *Journal of Macromolecular Science, Part A* **2016,** *53*, (6), 354-361.
11. Willner, M. R. *Raman-and-SERS-Processing 1.0.1*, Zenodo, 2017.
12. Willner, M. R., *Chapter 4* **2018**.
13. Willner, M. R.; McMillian, K.; Graham, D.; Zagnoni, M.; Vikesland, P. J., Surface Enhanced Raman Scattering (SERS) Based Optofluidics for Multiple Single Cell Analysis. *The Analyst - Submitted* **2018**.
14. Gracie, K.; Correa, E.; Mabbott, S.; Dougan, J. A.; Graham, D.; Goodacre, R.; Faulds, K., Simultaneous detection and quantification of three bacterial meningitis pathogens by SERS. *Chemical Science* **2014,** *5*, (3), 1030-1040.
15. Socrates, G., *Infrared and Raman Characteristic Group Frequencies: Tables and Charts*. Wiley: 2004.
16. Suzuki, M.; Shimanouchi, T., Infrared and Raman spectra of adipic acid crystal. *Journal of Molecular Spectroscopy* **1969,** *29*, (1), 415-425.
17. Berg, R. W.; Otero, A. D., Analysis of adipate ester contents in poly(vinyl chloride) plastics by means of FT-Raman spectroscopy. *Vibrational Spectroscopy* **2006,** *42*, (2), 222-225.
18. Nørbygaard, T.; Berg, R. W., Analysis of Phthalate Ester Content in Poly(Vinyl Chloride) Plastics by Means of Fourier Transform Raman Spectroscopy. *Applied Spectroscopy* **2004,** *58*, (4), 410-413.
19. Nyquist, R. A., Raman Group Frequency Correlations: Phthalate Esters. *Applied Spectroscopy* **1972,** *26*, (1), 81-85.
20. Smith, L. I. *A tutorial on principal components analysis*; 2002.

21. Norrman, K.; Ghanbari-Siahkali, A.; Larsen, N. B., 6 Studies of spin-coated polymer films. *Annual Reports Section "C" (Physical Chemistry)* **2005,** *101*, (0), 174.

Chapter 4 Surface Enhanced Raman Scattering (SERS) Based Optofluidics for Multiple Single Cell Analysis

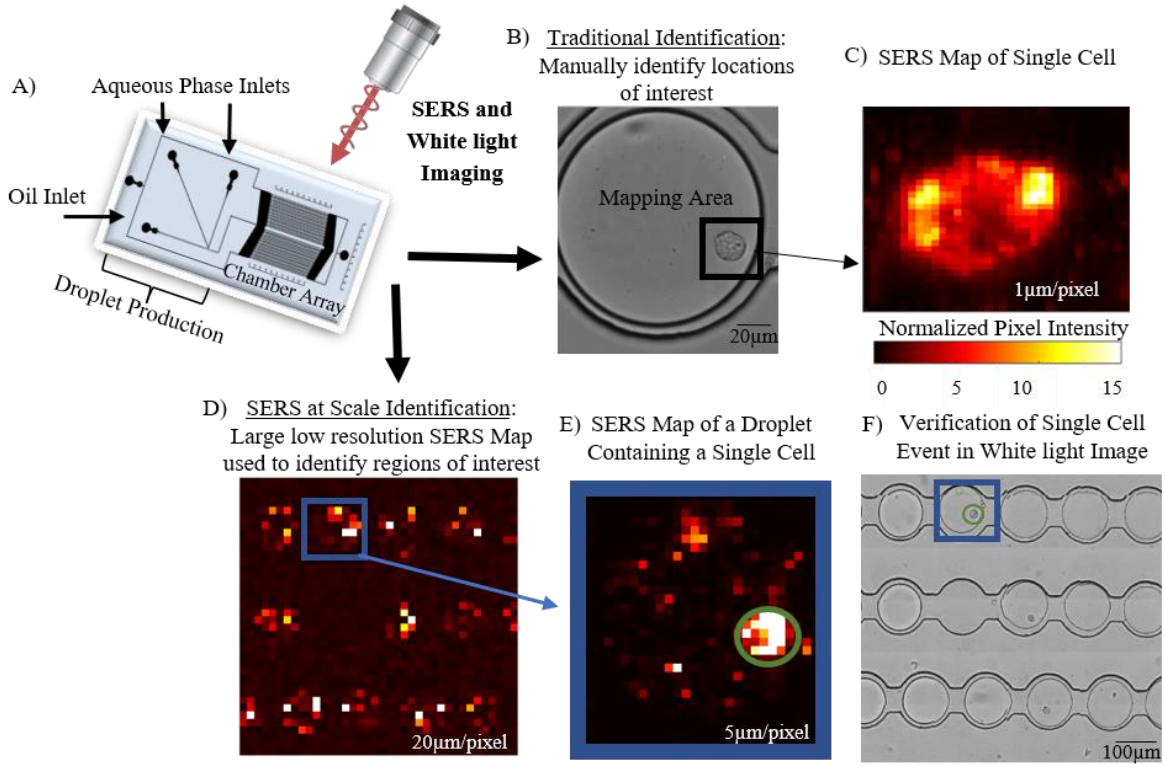

4.1 Abstract

The integration of surface enhanced Raman scattering (SERS) with droplet microfluidics has the potential to improve our understanding of cellular dynamics. Herein, we present the first application of SERS droplet microfluidics for single cell analysis. A microfluidic device was used to encapsulate single cells in water-in-oil droplets that were subsequently locked into a storage droplet array for spectroscopic investigation. The stationary droplets enabled the rapid identification of SERS regions of interest in live cells by allowing collection of "fast" coarse maps over an area of several mm^2 followed by "slower" detailed interrogation of the identified hotspots. We demonstrate SERS at cellular resolution via a proof-of-concept assay that detects glycan expression on the surface of prostate cancer cells using lectin modified metallic

nanoparticles. The data illustrates the potential of SERS optofluidic systems for high-throughput cell screening and illustrates a previously unobserved high degree of cell-to-cell variability in the size and number of glycan islands.

4.2 Introduction

Over the past decade, it has become increasingly clear that the genetic and phenotypic characterization of cell populations at the single cell level is a key consideration of fundamental biology research and cell screening. Single-cell droplet optofluidics, combining microfluidic technologies with analytical spectroscopies, presents an exciting opportunity to understand cell-to-cell variability. Significant developments have been made in single-cell -omics[1-3] to the point that digital droplet polymerase chain reaction (ddPCR) instruments are now commercially available. A smaller fraction of the literature has focused on analyzing the behavior of single cells encapsulated in droplets, from metabolite profiling[4] to growth monitoring.[5] Droplet microfluidics enables the production of thousands of individual microreactors in the form of surfactant stabilized emulsions, which are not subject to 'memory effects' or the adhesion of colloid/analyte conjugates within the microfluidic device.[6] The generation of nano- to femto-liter droplets for live cell studies is typically achieved by entraining aqueous droplets in perfluorochemical (PFC) oils that have a very high gas solubility and thus allow for oxygen exchange.[7] Past studies have shown that organisms can be kept alive in droplets for several days.[8]

The ability to homogenously introduce material into each droplet has wide reaching benefits including enabling the development of quantitative surface enhanced Raman scattering (SERS). Until recently, quantitative *in situ* SERS detection has been challenging due to the difficulty associated with reproducing gold (Au) and silver (Ag) colloid distributions and maintaining consistent analyte-nanoparticle interactions across experiments.[9] SERS is a well-established technique that can be used for the detection of trace levels of metals, toxins, pesticides, DNA, proteins, pathogens, and eukaryotic cells.[10-17] SERS is particularly well suited for bioanalytical applications because it is non-destructive and non-invasive and it provides high

molecular specificity and spatial resolution.[18] Importantly, fresh tissues and cells can be interrogated with minimal prior preparation because of the weak Raman signal of water molecules.[19] To date, label-free Raman/SERS optofluidic detection has been reported in the literature for crystal violet,[9] potassium ferricyanide,[20] the pharmaceuticals promethazine and mitoxantrone,[21] *Escherichia coli*,[22] and *Staphylococcus aureus*.[23] Recently, the first work on SERS optofluidics for eukaryotic cell lysate analysis was published,[24] however the use of this approach for investigating cellular properties at the single cell level and in a throughput format is currently under studied.

In this study, we combine droplet microfluidics with SERS to study cell-to-cell and intracellular variability in the expression of glycans on the cell membrane. Cell membrane carbohydrates are an important oncology target[25] because their overexpression by cancerous cells, relative to healthy cells, can provide an early indication of cancer. Previously, we demonstrated that the glycan N-acetyl neuraminic (sialic) acid expressed by cancerous prostate (PC3) cells can be targeted using the lectin wheat germ agglutinin (WGA).[11] This glycan detection assay was selected for three main reasons: first, the sialic acid residues (target) are abundant on the cell membrane; second, the attachment of the recognition element (lectin) to gold nanoparticles via streptavidin-biotin chemistry is a robust and rapid functionalization method; and, finally, the ability to introduce a reporter molecule with a large Raman cross section ensured that the SERS signal could be detected through the four interfaces of the device. The use of an established assay allowed us to focus this study on the development of an integrated optofluidic system and the associated analysis algorithms. The two major outcomes are demonstration of the capacity to probe the content of stationary droplets on a variety of scales and the first application of whole cell imaging using SERS optofluidics.

4.3 Materials and Methods

4.3.1 Device Design and Preparation

Microfluidic devices were fabricated using standard photo- and soft-lithography techniques, as previously described.[26] Briefly, master templates were produced on silicon wafers using SU8 photoresist (3000 series, MicroChem, US) following the manufacturer's protocol and achieving a final resist thickness of 50 μm. The resist was exposed through a photomask (JD Photo-Tools, UK) to UV light and was developed in Micro-Posit EC solvent (Rohm and Haas, US). Finally, the wafer surface was silanized by vapor deposition of 1H,1H,2H,2H-perfluorooctyltrichlorosilane (Sigma Aldrich, UK) for 1 hour. Polydimethylsiloxane (PDMS) was poured onto the silicon master at a 10:1 (w:w) ratio of base to curing agent, degassed in a vacuum desiccator chamber, and cured at 80 °C for at least 2 hours. The PDMS devices were then peeled from the mold, cut to the desired size, and holes were punched using 1 mm biopsy punches to obtain inlet and outlet ports. Devices were cleaned and irreversibly bonded to glass microscope slides using oxygen plasma and subsequently treated with undiluted Aquapel (PPG Industries) to obtain fluorophilic microchannel surfaces.

4.3.2 Nanoparticle Synthesis and Functionalization

Sodium citrate (final concentration 3.88 mM) was added to 100 mL of boiling 1 mM tetrachloroauric acid under vigorous mixing conditions. The reaction was allowed to run until the solution color changed to wine red, indicating completion. Gold nanoparticles were functionalized in 5 mL batches and were pH adjusted to circumneutral using 0.1 M potassium carbonate. Next, 2 μM of malachite green isothiocyanate (MGITC), a strong SERS dye with a distinct finger print, was used to pre-aggregate gold colloid. The colloid was coated with 0.1 mg/mL streptavidin, and it was then mixed with 2% BSA to quench further aggregation. After >30 minutes, the colloid was centrifuged and biotin functionalized wheat germ agglutinin (WGA; Sigma-Aldrich, UK) was added to the nanoparticle pellet at a concentration of 0.17 mg per mL colloid. Following overnight incubation, the nanoprobes were washed three times with 1% BSA in PBS. The local surface plasmon resonance (LSPR) of the probes was between 530 nm and 533 nm as

determined by UV-vis and the particle size (z-average) of the probes in 1% BSA was ~130 nm with a polydispersity index between 0.5 and 0.6 as determined by dynamic light scattering (Malvern Nano-ZS, Malvern, UK).

4.3.3 Cell Preparation

Tumourigenic (PC-3) human prostate epithelial cell lines were cultured in RPMI 1640 Medium supplemented with HEPES, 10% fetal calf serum, 1% penicillin, 1% streptomycin, and 1% fungizone (Gibco, UK). Cells were grown to confluence in an incubator at 37 °C with 5% CO_2 and then harvested with trypsin/EDTA. Solutions containing 10^6 cells/mL were used for microfluidic experiments, leading to approximately one cell per droplet for the flow rates used.

4.3.4 Device Loading

Microfluidic devices were connected to 1 mL syringes via polytetrafluoroethylene (PTFE) tubing (Cole Parmer). Syringe pumps were used to vary the fluid flow rates between 0.16 and 0.21 mL/hour to produce droplets of the appropriate size at the T-junction. The continuous phase was FC-40 (3M Company) fluorinated oil with 2 wt% block copolymer fluorosurfactant (designed by the Weitz Group at Harvard and supplied by RAN Biotechnologies, catalogue# 008-FluoroSurfactant, Beverly, MA, USA). The dispersed phase was a solution of phosphate buffered saline (PBS) or phenol-free media containing cells that had been incubated with nanoprobes and subsequently washed.

4.3.5 SERS Spectroscopy

Two different instruments were used to collect data. A WITec Alpha 300R confocal microscope (WITec, Ulm, Germany) in an upright set-up employing a 633 nm wavelength excitation laser and a 300g/mm and an inverted Renishaw InVia system (Renishaw, Wolton-under-Edge, UK) employing a 633 nm wavelength excitation laser and a 1200 g/mm grating. A suite of objectives were utilized and are detailed in **Table 4-1**.

4.3.6 SERS Processing

A data processing tool was developed in Matlab to process Raman or SERS spectra in the SPC file format. Briefly, spectra were baseline corrected using an asymmetric least squares baseline correction.[27] A peak or peaks of interest were then specified and the intensity of the peaks was automatically extracted from the dataset. For data collected in a rastering format (maps) the intensity at each point could be plotted to generate SERS maps.

4.4 Results and Discussion

To interrogate single cells within polydimethylsiloxane (PDMS) microfluidic devices using SERS, a laser must pass through four media (**Figure 4.1**A) before interacting with the sample. Malachite green isothiocyanate (MGITC) was selected as the Raman reporter because its signature peaks at 1614 cm^{-1} and 1364 cm^{-1}, assigned to the phenyl-N + C−C stretching mode and the phenyl-N stretching mode [28], do not overlap with the strong PDMS asymmetric and symmetric C-H stretches at 2965 cm^{-1} and 2903 cm^{-1} respectively[29-31] (**Figure 4.1**A). Gold nanoparticles (35 nm) were pre-aggregated with MGITC, coated with streptavidin, mixed with biotinylated wheat germ agglutinin (WGA) and then washed to removed unbound WGA. The adherent PC3 cells were removed from the culture flask to create a cell suspension, incubated with the nanoprobes for 10 minutes, washed and ultimately encapsulated in droplets. The droplets were subsequently stored in a chamber array, a modified version of the dropspot device[32], before the device was transferred for imaging by Raman microscopy.

SERS data of biological samples is often acquired by defining a region of interest over which the laser is rastered. At each pixel location a spectrum is collected, from each spectrum the same feature (i.e., wavenumber or wavenumber range) is selected, and the value (i.e., intensity or integrated intensity) of the feature is then plotted on an *x-y* grid to generate a SERS map. Commonly, conclusions are drawn by manually inspecting SERS maps, but the use of statistical descriptions and chemometric analyses are becoming a standard part of SERS data analysis. Often these higher order descriptions, such as in our work

on intracellular pH[33] detection, are accompanied with re-rendered SERS maps that display complex content. However, variability between maps or the physical clustering of regions of interest (i.e., how many pixels meeting a certain criterion are adjacent to one another) is not taken into account. While not appropriate for all experiments, the study of cell expression, especially as enabled by droplet microfluidics, supports the adoption of automated techniques to detect regions of interest. The imaging processing techniques developed in our data tool allow us to generate SERS maps, to then identify regions of interest within each map, and then statistically analyze the size and distribution of each region.

4.4.1 Development of Data Processing and Analysis Tool.

A workflow diagram illustrating our data processing algorithm is shown in **Figure 4.2**. SERS maps enable visualization of the results of a SERS experiment and are a simplification of the total data collected (i.e., a reduction in data dimensionality). Embedded within each pixel of a SERS map is a full spectrum containing 1015 (Wire 4.2) or 1024 (Project FOUR 4.1) points and a myriad of vibrational information. A typical SERS map obtained for the single cell studies contained 900 pixels or a total of 9×10^5 points. Baseline correcting, normalizing, and rendering a SERS map based on the intensity of a specific peak was readily achieved using proprietary software such as Wire 4.2 or Project FOUR 4.1. However, these programs generally lack batch processing capacity, transparency in the data processing algorithms, and the ability to open data files in a non-proprietary format. To overcome these challenges and to take advantage of the large amount of information available from the SERS optofluidic platform a specialized data analysis and processing tool was written in Matlab. The code is readily available online at GitHub[34].

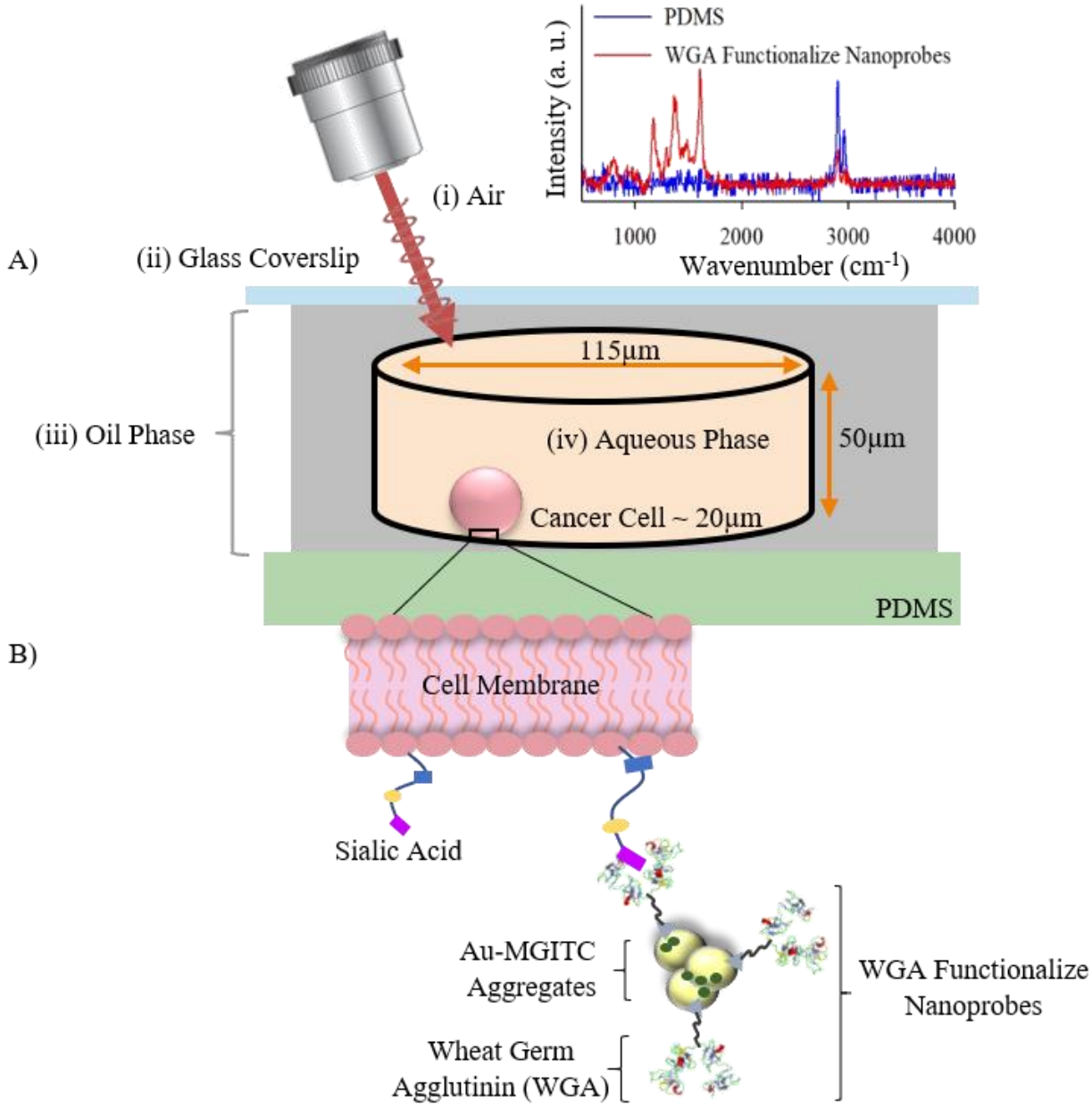

Figure 4.1. Illustration of a single cell encapsulation event within the microfluidic device. The four media that the laser must pass through before interacting with the target (cancer cell) are labeled from i to iv. The cartoon also includes the dimensions of the microfluidic device and cancer cell. The inset displays the Raman spectrum from the PDMS and the SERS spectra from Wheat Germ Agglutinin (WGA) functionalized nanoprobes (A). Zoom in of the cell membrane shows the expression of sialic acid. A WGA functionalized nanoprobe is shown attached to the sialic acid and the individual components of the probe are named (B).

To optimize data handling and cross-platform functionality, we exported data from Wire 4.2 or Project Four 4.1 using the SPC file format (.spc). This data was then imported into Matlab for further processing. .spc is preferred over text (.txt) or comma separated value (.csv) files because it contains the raw spectra plus metadata containing additional scan details. Within Matlab, automated baseline correction was achieved using a modification of Eiler's asymmetric least squares baseline estimation.[27] Following normalization, SERS maps could be rendered based on the intensity of a specific peak, the ratio of multiple peaks, or based on the mathematical transformation of a peak ratio.[33] To demonstrate the efficacy of this data processing tool, data from a single experiment was processed using the tool and the Wire 4.2 proprietary software (**Figure 4.6**). Collected data was baseline corrected, the intensity of the 1609 cm^{-1} peak was plotted (feature selection) and the maps were scaled using the same look-up-table (LUT) so that they could be directly compared. The resulting maps from the data processing tool and Wire 4.2 were identical. A spectrum to spectrum comparison of the data from a single pixel (**Figure 4.6**2C & 2D) shows that the baseline corrected data is nearly identical, as would be expected from using distinct algorithms.

The advantages of using this automated tool are evident when processing and analyzing a large number of analyses from an experiment or dataset (i.e., the collection of SERS maps collected from a single microfluidic device or project). The characteristics of each map, such as the minimum, maximum, and average pixel values, can be collated during processing and can be queried after all the data was processed to define a LUT. The maps can then be rescaled based on these statistics. For example, in our study of cell-to-cell heterogeneity (as discussed *vide infra*) the LUT was defined to be 2× to 3× the standard deviation above the mean. Other variable ranges can be readily defined depending on the desired application. The library of SERS maps were analyzed and edge finding scripts were used to identify regions of interest and the size of clusters meeting certain criteria were calculated.

4.4.2 SERS Whole Cell Imaging and observation of cell-to-cell heterogeneity.

To demonstrate the capacity of the optofluidic platform for single cell analysis, wheat germ agglutin (WGA) was used to target the glycan N-acetyl neuraminic (sialic) acid expressed on cancerous prostate

(PC3) cells. Pre-aggregated SERS hotspots coated with WGA – nanoprobes – were mixed, in excess, with PC3 cells, after a ten-minute incubation period the cells were washed and introduced into the microfluidic platform. A Poisson distribution for cell encapsulation in droplets was considered. A cell loading concentration of 10^6 cells per mL favored the formation of single cell encapsulation events.[35] SERS maps were then collected from: i) individual droplets with a focus on single cell encapsulation events, representative images shown in **Figure 4.3**A-C; and ii) multiple droplets (discussed in the next section).

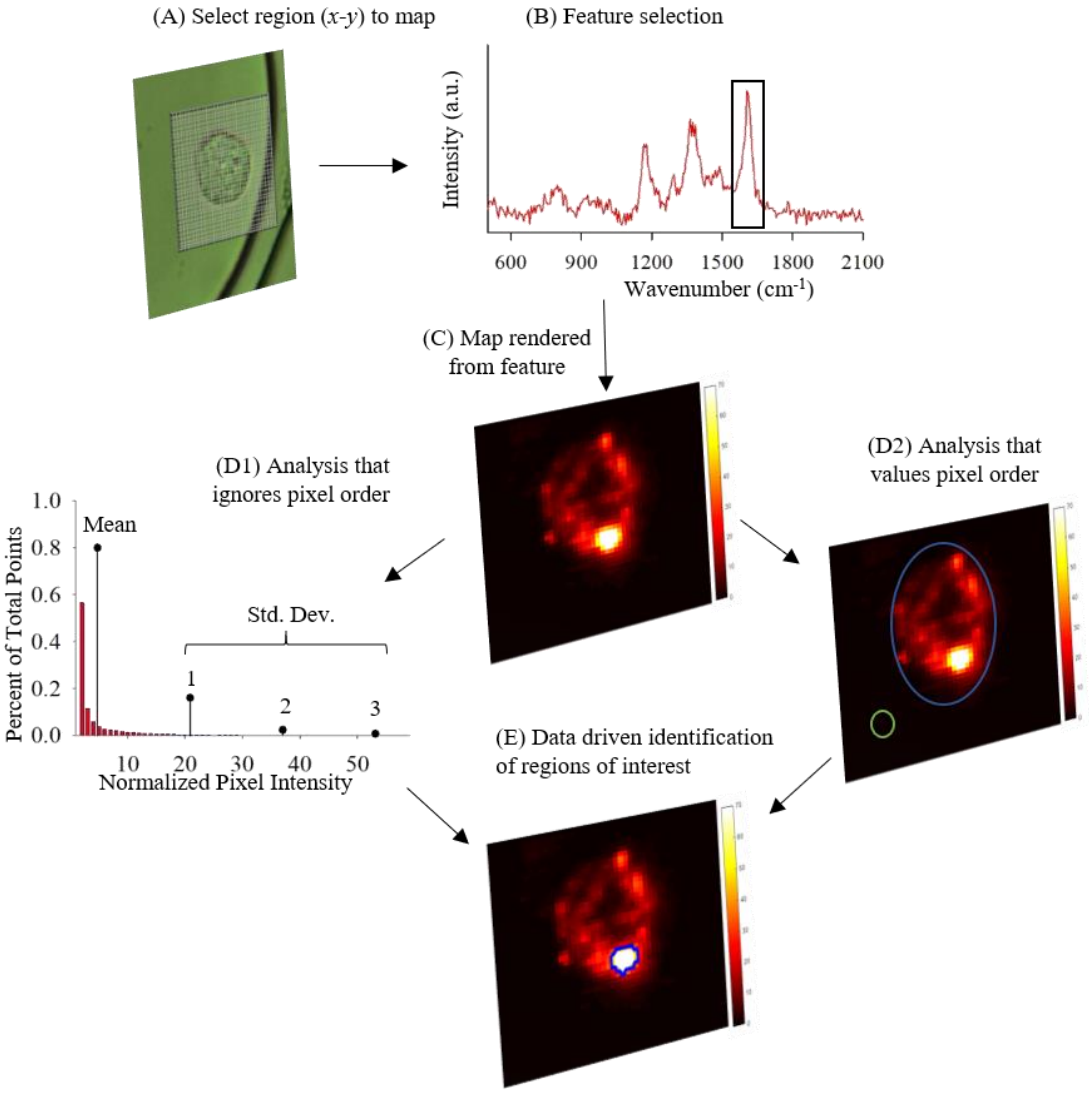

Figure 4.2. Details of SERS scan: 20× Objective; 40µm by 40µm area of interest; pixel size 1µm/pixel; grating 1200g/mm; 633nm laser; collection time 0.1 seconds. (A) At each pixel a spectrum is collected in two dimensions: intensity vs wavenumber. Pre-processing such as baseline correction and normalization are undertaken followed by feature selection. (B) Single SERS maps are rendered after feature selection to aid in data interpretation. At each *x*-y coordinate the intensity of the feature is depicted using a color (C). A library of maps is generated and increases the dimensionality to 4D (map × *x* location × *y* location × wavenumber) or after feature selection, fixing the wavenumber, 3D (map × *x* location × *y* location). Typical SERS data processing only discusses pixel intensity and uses measures such as mean intensity, standard deviation, etc. to describe the data set. For analysis of cells and other ordered objects crucial information is lost by neglecting pixel order (D1). Corrected total intensity (CTI) is a simple method that values pixel order. The area of interest is selected, blue circle, and the integrated density of the area is calculated (area × mean intensity). From this value, the mean background intensity × area of cell is subtracted to yield the CTI. (D2) Combing the statistical information and pixel order allows for complex analysis of the maps. For example, from the map library (D1) the value of two and three standard deviations above the mean pixel intensity can be calculated. These values can be used to recolor the map (C) and visually the contrast between the background and region of interest (ROI) becomes evident. The data tool can also now distinguish the ROI from the background and determined the size of the ROI (E).

and then normalized by the SERS intensity of the nanoprobes for that experiment. SERS maps, such as those in **Figure 4.3**D-F, were then generated by selecting the spectral feature at 1609 cm^{-1} and plotting the intensity at each pixel. To compare maps and evaluate cell-to-cell variability, a new parameter, corrected total intensity (CTI), was defined. This parameter, an analogue to corrected total cell fluorescence (CTCF)[36,37], values pixel order and how the object of interest is distinct from the background. A benefit of SERS rastering is the collection of data with four dimensions (*x* location, *y* location, wavenumber, and intensity). In generating a map, the dimensionality of the data is reduced to three dimensions (*x* location, *y* location, and intensity at a specific wavenumber) and allows for intuitive visual inspection that is easily correlated to the mapped feature (i.e., a cell). However, in typical SERS analyses the *x* and *y* mapping data are disregarded and the discussion is focused on the statistical characterization of a spectral feature of interest. While this approach may be appropriate for the mapping of homogenous samples, the study of biological samples demands that the *x*-*y* information, the ordering of the pixels, is taken into account during analysis. Fluorescence spectroscopy often deals with data in the three dimensions of *x* location, *y* location, and intensity and thus we adopted the corrected total cell fluorescence measurement to analyze SERS maps.

The CTI measurements are determined by calculating the integrated density, the mean image intensity multiplied by the area of interest, and subtracting the average background intensity. Standard CTCF analysis is performed using ImageJ. Within ImageJ a threshold is applied to an imported image to find the objects of interest and the integrated density is then calculated for those regions of interest. The intensity for the background is then determined in ImageJ and ultimately in Excel (or a program of choice) the CTCF is calculated by finding the difference between the mean intensity in the ROI and the background and multiplying that by the area of the ROI. Our CTI were calculated in ImageJ using the same protocol except the starting images were SERS maps generated from the data. To demonstrate the need for ROI selection, the CTI data is compared with the total map intensity, the sum of the intensity at every point in the map, or described differently the integrated density of the map without ROI selection **Figure 4.3**G.

The coefficient of variation (CoV) was used to describe the variation across the collected data sets and the CTI results had a consistently larger CoV than the total map intensities (**Table 4-2**). In the total map calculations, the intensity contribution of the cell, which occupies ~30% of the map area, was damped by the background pixels. To demonstrate that the variation in the nanoprobe attachment from to cell-to-cell was neither the product of the functionalization chemistry, nor the orientation of the cells during cell mapping, the experiment was replicated using WGA functionalized with the fluorophore fluorescein

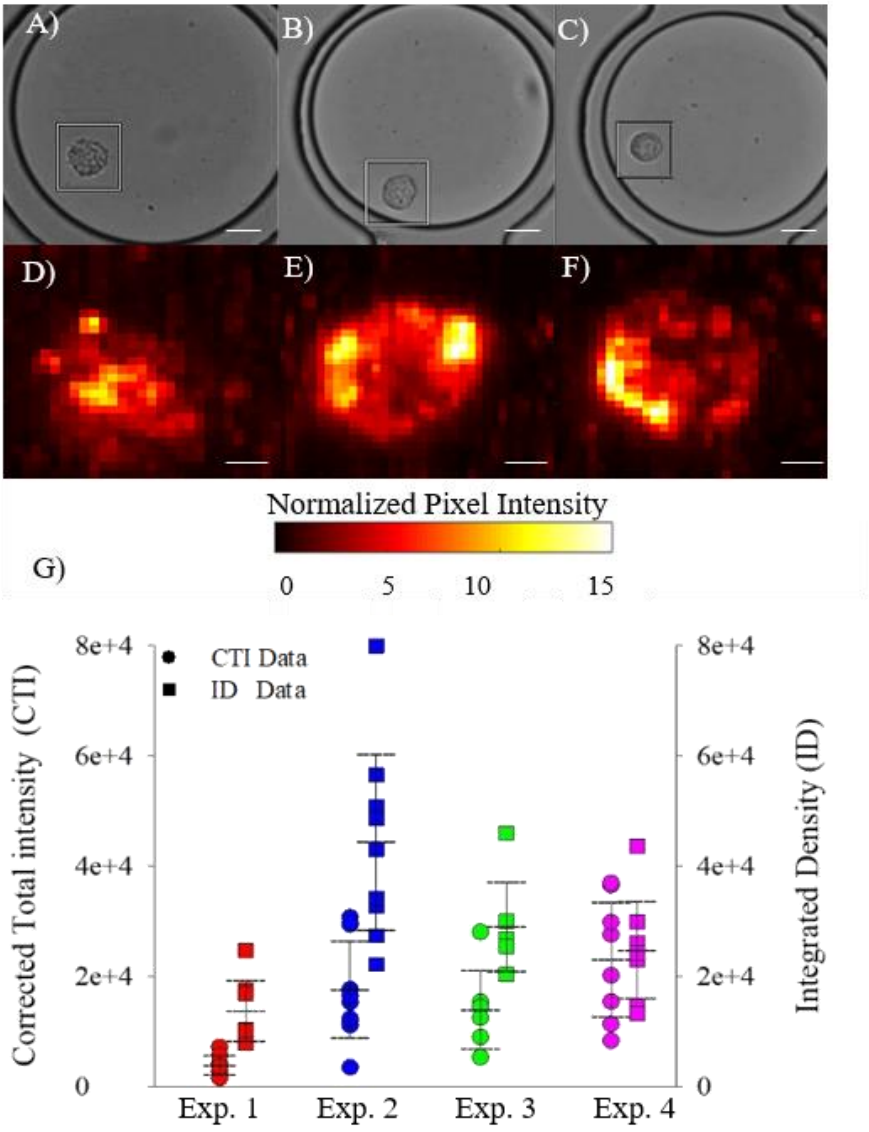

Figure 4.3. Optical images with a 20µm scale bar (A-C) of single PC3 cells encapsulated in droplets with the corresponding SERS maps with 5µm scale bar (D-F). The corrected total intensity (circles) and integrated dentistry (squares) for four different experiments, each represented in a unique color, with error bars representing one standard deviation (G).

(FITC). Interestingly, when the coefficient of variation for the CTFC results were tabulated (**Table 4-3**) they fell in the same range, 0.4 and 0.6, as the CTI calculations. The results show that there is indeed cell to cell variability in the expression of sialic acid residues on the surface of the PC3 cells.

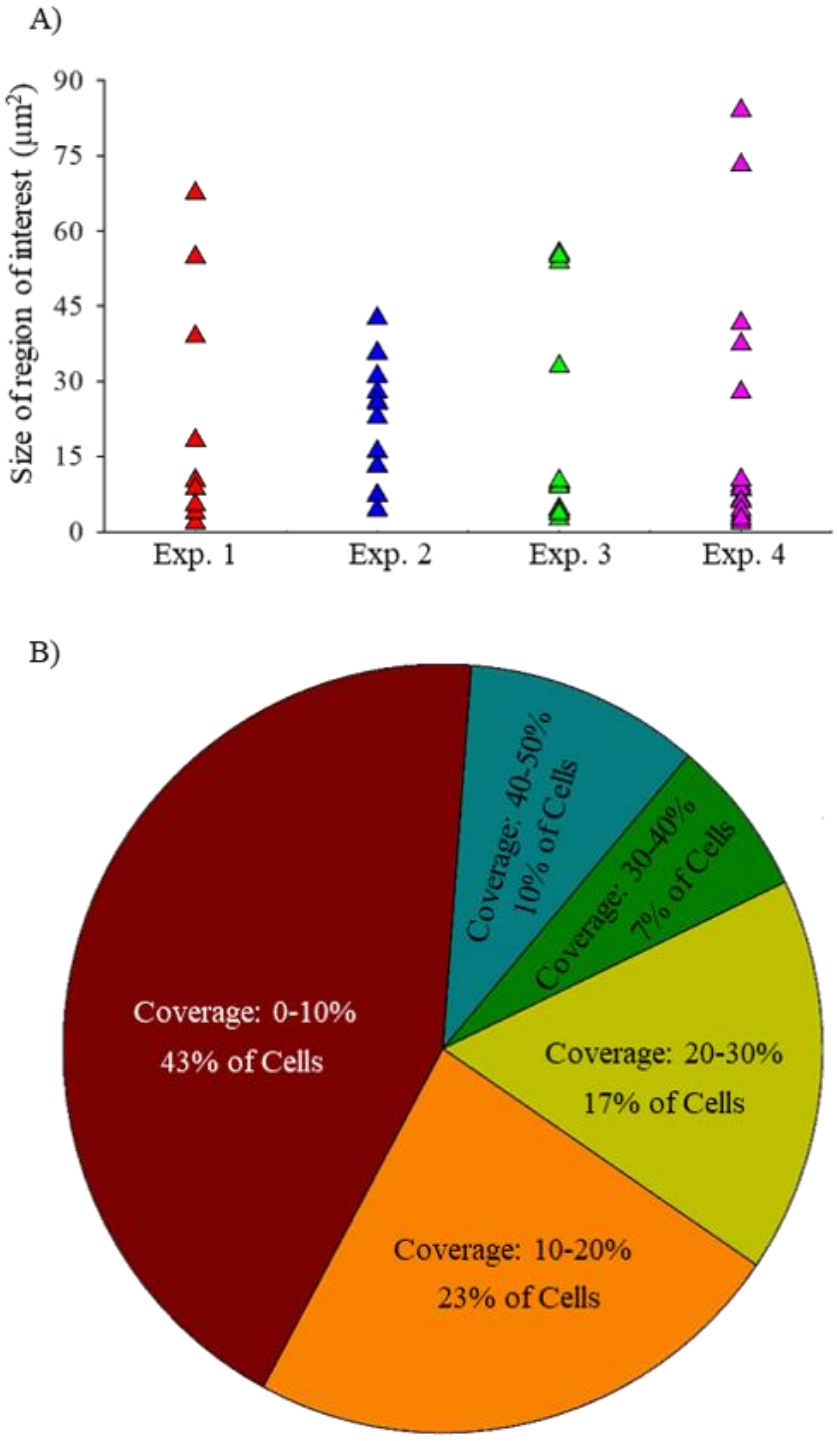

Figure 4.4. The size of all regions of interest (ROI), classified as a cluster of more than one pixel with an intensity greater than two standard deviations (2x) above the mean, for each experiment (A). Pie graph showing the distribution of ROI size (μm^2) for the whole data set. Each wedge is labeled with the size range and the percentage of ROI in that wedge (B).

In comparing the SERS maps, **Figure 4.3**D-F, and the fluorescence images, **Figure 4.8**, it was apparent that sialic acid residues were heterogeneously distributed on the cell surface, typically with a large cluster of glycans occurring in one area. To quantify the size of the glycan clusters the data processing tool was expanded for image processing. Specifically, for each experiment the LUT was defined to be 2× to 3× the standard deviation above the mean intensity of the data set; this thresholding set the majority of the background (pixels) to black. Contrast aids the edge finding scripts in determining the boundary between the region of interest and the background. Pixels above the threshold were identified and only clusters containing more than one pixel were extracted from the maps; maps could contain more than one cluster. The size of the clusters, in μm^2, was determined and the cluster sizes on a per experiment basis plotted (**Figure 4.4**A).

Most of the clusters, 53%, were less than 10 μm^2 and given that the average PC3 cell is 20 μm in diameter and, modeling the cell simply as a sphere, most clusters cover less than 3% of the cell surface. Even the largest cluster at 84 μm^2 occupies at max 27% of the area of an average cell. However, 47% of cells contain more than one glycan island suggesting that a direct area to area comparison would be more descriptive of glycan expression.

To understand the surface coverage in more detail, for each cell the size of the glycan island(s) was compared to the cell area. The exposed cell area was calculated with the same edge finding scripts as the island area except that input figures were the optical images of the cells. The pie graph (**Figure 4.4**B) underscores that most of the cells, 66%, had less than 20% of their total exposed area covered by glycans. Returning to the largest cluster, it was found to be the only island on that specific cell, the largest island in the dataset, covered 30% of the area of the cell; extremely close to the initial estimate. The largest total glycan area was 111 μm^2, originating from two islands, and covering 43% of the cell area whereas the cell with greatest coverage, 48%, contained a total glycan area of 74 μm^2. The fact that the largest single island, largest total glycan area, and largest area coverage are found on three different cells underscores that cell-to-cell variability exists and measuring the differences becomes accessible with the implementation of

SERS optofluidics. Moreover, the identification of these heterogeneities on the cell surface prompted biological experiments.

4.4.3 Imaging Across Scales.

A major benefit of using SERS optofluidics is the ability to examine many different cells at once. Typically, as done for the whole cell imaging, regions of interest are manually identified under white light and then SERS mapping areas are defined. The process of visually identifying regions of interest is laborious and time consuming especially when compared with fluorescent images, such as those in **Figure 4.8**, where hundreds of cells can be imaged quickly. Furthermore, the ability to identify SERS ROI's

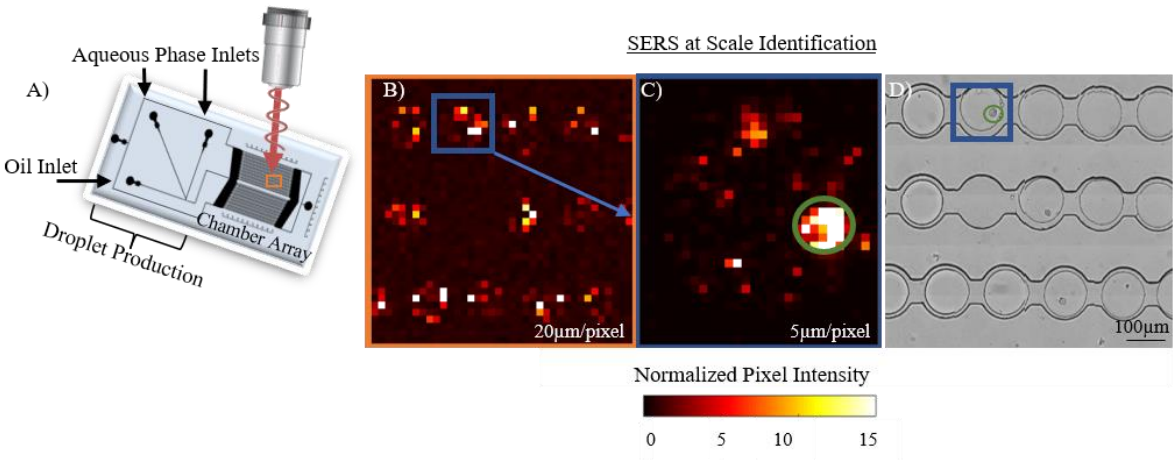

Figure 4.5. Schematic of the optofluidic platform (A) followed by the SERS at scale process. Note that the orange box in A denotes the SERS mapping shown in B. The processed low-resolution SERS map is shown in B with an area of interested outlined with a blue box. The area of interest is than scanned with higher resolution (C) and a second region of interest, the cell, is circled in green. The white light image of the area, orange box, is collected and then two regions of interest, blue box and green circle, are used to confirm the accurate identification of the cell.

without first using the white light image is advantageous because it removes the reliance on the white light microscope and pushes towards fully automated application. **Figure 4.5** shows the potential of SERS detection at scale with panel B showing a SERS map of a 760 μm by 760 μm region, taken at a relatively low resolution (20μm/pixel). An area of interest was identified and mapped at higher resolution (5μm/pixel), panel C, and the map clearly showed the presence of a cell. A bright field image was then

collected and confirmed the presence of a cell. A more detailed map, such as that in the single cell experiments could also have been easily collected if so desired

SERS at scale presents many exciting capabilities and has the ability to increase the applicability of SERS for biological studies. The ability to survey over 1000 droplets rapidly increases the quantification accessible with SERS for both lab based studies and the production of point-of-care sensors. Rapid SERS screening will allow the method to compete with more standard techniques such as flow cytometry but introduce the ability to easily identify and map with high resolution cells of interest. The platform is well suited for the study of environmental samples that are typically sample limited and/or highly dilute. The automated platform will aid in the identification of targets of interest without destroying the sample thus allowing SERS to be combined with more traditional analyses such as culturing or genomics analysis. Another major benefit of using SERS at scale is the ability to study dynamic processes. Unlike, fixed cell experiments or -omics analyses, the optofluidic platform allows for the study of cellular behavior as a function of time. With slight modifications to the platform, stressors can be introduced into the droplets and SERS can be used to measure the change in behavior of individual cells, opposed to traditional measurements which look at changes in bulk population behavior.

4.5 Conclusion and Future Outlook.

SERS optofluidics is a powerful tool for single-cell analysis and the dynamic imaging of aqueous studies of biological importance. In this paper, we have used this technology to show cell-to-cell variation, create a centralized data processing tool and show the ability to access information at a range of scales. The methods and tools presented here lay the foundation for future SERS optofluidics studies and show the first application of the platform for deciphering the composition of cell membranes. Additionally, the use of imaging processing to interpret SERS maps can be adopted for other applications where the region of interest is only a subset of the total area mapped.

4.6 References

(1) Hindson, B. J.; Ness, K. D.; Masquelier, D. A.; Belgrader, P.; Heredia, N. J.; Makarewicz, A. J.; Bright, I. J.; Lucero, M. Y.; Hiddessen, A. L.; Legler, T. C.; Kitano, T. K.; Hodel, M. R.; Petersen, J. F.; Wyatt, P. W.; Steenblock, E. R.; Shah, P. H.; Bousse, L. J.; Troup, C. B.; Mellen, J. C.; Wittmann, D. K., et al. *Anal Chem* **2011**, *83*, 8604-8610.

(2) Macosko, E. Z.; Basu, A.; Satija, R.; Nemesh, J.; Shekhar, K.; Goldman, M.; Tirosh, I.; Bialas, A. R.; Kamitaki, N.; Martersteck, E. M.; Trombetta, J. J.; Weitz, D. A.; Sanes, J. R.; Shalek, A. K.; Regev, A.; McCarroll, S. A. *Cell* **2015**, *161*, 1202-1214.

(3) Klein, A. M.; Mazutis, L.; Akartuna, I.; Tallapragada, N.; Veres, A.; Li, V.; Peshkin, L.; Weitz, D. A.; Kirschner, M. W. *Cell* **2015**, *161*, 1187-1201.

(4) Bjork, S. M.; Sjostrom, S. L.; Andersson-Svahn, H.; Joensson, H. N. *Biomicrofluidics* **2015**, *9*, 044128.

(5) Girault, M.; Kim, H.; Arakawa, H.; Matsuura, K.; Odaka, M.; Hattori, A.; Terazono, H.; Yasuda, K. *Sci Rep* **2017**, *7*, 40072.

(6) Theberge, A. B.; Courtois, F.; Schaerli, Y.; Fischlechner, M.; Abell, C.; Hollfelder, F.; Huck, W. T. S. *Angew Chem Int Ed Engl* **2010**, *49*, 5846-5868.

(7) Lowe, K. C. *Journal of Fluorine Chemistry* **2002**, *118*, 19-26.

(8) Clausell-Tormos, J.; Lieber, D.; Baret, J. C.; El-Harrak, A.; Miller, O. J.; Frenz, L.; Blouwolff, J.; Humphry, K. J.; Koster, S.; Duan, H.; Holtze, C.; Weitz, D. A.; Griffiths, A. D.; Merten, C. A. *Chem Biol* **2008**, *15*, 427-437.

(9) Liu, B. X.; Jiang, W.; Wang, H. T.; Yang, X. H.; Zhang, S. J.; Yuan, Y. F.; Wu, T.; Du, Y. P. *Microchimica Acta* **2013**, *180*, 997-1004.

(10) Chung, E.; Lee, J.; Yu, J.; Lee, S.; Kang, J. H.; Chung, I. Y.; Choo, J. *Biosensors and Bioelectronics* **2014**, *60*, 358-365.

(11) Craig, D.; McAughtrie, S.; Simpson, J.; McCraw, C.; Faulds, K.; Graham, D. *Anal Chem* **2014**, *86*, 4775-4782.

(12) Lee, S.; Chon, H.; Lee, J.; Ko, J.; Chung, B. H.; Lim, D. W.; Choo, J. *Biosensors and Bioelectronics* **2014**, *51*, 238-243.

(13) Lee, S.; Chon, H.; Lee, M.; Choo, J.; Shin, S. Y.; Lee, Y. H.; Rhyu, I. J.; Son, S. W.; Oh, C. H. *Biosensors and Bioelectronics* **2009**, *24*, 2260-2263.

(14) Pallaoro, A.; Braun, G.; Moskovits, M. *MRS Proceedings* **2012**, *1468*.

(15) Qian, X.; Peng, X. H.; Ansari, D. O.; Yin-Goen, Q.; Chen, G. Z.; Shin, D. M.; Yang, L.; Young, A. N.; Wang, M. D.; Nie, S. *Nat Biotechnol* **2008**, *26*, 83-90.

(16) Scaffidi, J. P.; Gregas, M. K.; Seewaldt, V.; Vo-Dinh, T. *Anal Bioanal Chem* **2009**, *393*, 1135-1141.

(17) Gracie, K.; Correa, E.; Mabbott, S.; Dougan, J. A.; Graham, D.; Goodacre, R.; Faulds, K. *Chemical Science* **2014**, *5*, 1030-1040.

(18) Brautigam, K.; Bocklitz, T.; Silge, A.; Dierker, C.; Ossig, R.; Schnekenburger, J.; Cialla, D.; Rosch, P.; Popp, J. *Journal of Molecular Structure* **2014**, *1073*, 44-50.

(19) Old, O. J.; Fullwood, L. M.; Scott, R.; Lloyd, G. R.; Almond, L. M.; Shepherd, N. A.; Stone, N.; Barr, H.; Kendall, C. *Analytical Methods* **2014**, *6*, 3901-3917.

(20) Cristobal, G.; Arbouet, L.; Sarrazin, F.; Talaga, D.; Bruneel, J. L.; Joanicot, M.; Servant, L. *Lab Chip* **2006**, *6*, 1140-1146.

(21) Ackermann, K. R.; Henkel, T.; Popp, J. *Chemphyschem* **2007**, *8*, 2665-2670.

(22) Walter, A.; Marz, A.; Schumacher, W.; Rosch, P.; Popp, J. *Lab Chip* **2011**, *11*, 1013-1021.

(23) Lu, X.; Samuelson, D. R.; Xu, Y.; Zhang, H.; Wang, S.; Rasco, B. A.; Xu, J.; Konkel, M. E. *Anal Chem* **2013**, *85*, 2320-2327.

(24) Hassoun, M.; Ruger, J.; Kirchberger-Tolstik, T.; Schie, I. W.; Henkel, T.; Weber, K.; Cialla-May, D.; Krafft, C.; Popp, J. *Anal Bioanal Chem* **2017**.

(25) Raval, G. N.; Parekh, L. J.; Patel, D. D.; Jha, F. P.; Sainger, R. N.; Patel, P. S. *Indian J Clin Biochem* **2004**, *19*, 60-71.

(26) McMillan, K. S.; McCluskey, A. G.; Sorensen, A.; Boyd, M.; Zagnoni, M. *Analyst* **2016**, *141*, 100-110.

(27) Eilers, P. H. *Anal Chem* **2004**, *76*, 404-411.

(28) Leng, W.; Vikesland, P. J. *Langmuir* **2014**, *30*, 8342-8349.

(29) Smith, A. L. *Spectrochimica Acta* **1960**, *16*, 87-105.

(30) Cai, D.; Neyer, A.; Kuckuk, R.; Heise, H. M. *Journal of Molecular Structure* **2010**, *976*, 274-281.

(31) Jayes, L.; Hard, A. P.; Sene, C.; Parker, S. F.; Jayasooriya, U. A. *Anal Chem* **2003**, *75*, 742-746.

(32) Schmitz, C. H.; Rowat, A. C.; Koster, S.; Weitz, D. A. *Lab Chip* **2009**, *9*, 44-49.

(33) Wei, H.; Willner, M. R.; Marr, L. C.; Vikesland, P. J. *Analyst* **2016**, *141*, 5159-5169.

(34) Willner, M. R. Raman-and-SERS-Processing 1.0.1 **2017**, DOI: 10.5281/zenodo.838226 https://github.com/MarjorieRWillner/Raman-and-SERS-Processing/tree/1.0.1

(35) Collins, D. J.; Neild, A.; deMello, A.; Liu, A. Q.; Ai, Y. *Lab Chip* **2015**, *15*, 3439-3459.

(36) Burgess, A.; Vigneron, S.; Brioudes, E.; Labbe, J. C.; Lorca, T.; Castro, A. *Proc Natl Acad Sci U S A* **2010**, *107*, 12564-12569.

(37) McCloy, R. A.; Rogers, S.; Caldon, C. E.; Lorca, T.; Castro, A.; Burgess, A. *Cell Cycle* **2014**, *13*, 1400-1412.

4.7 Supporting Information

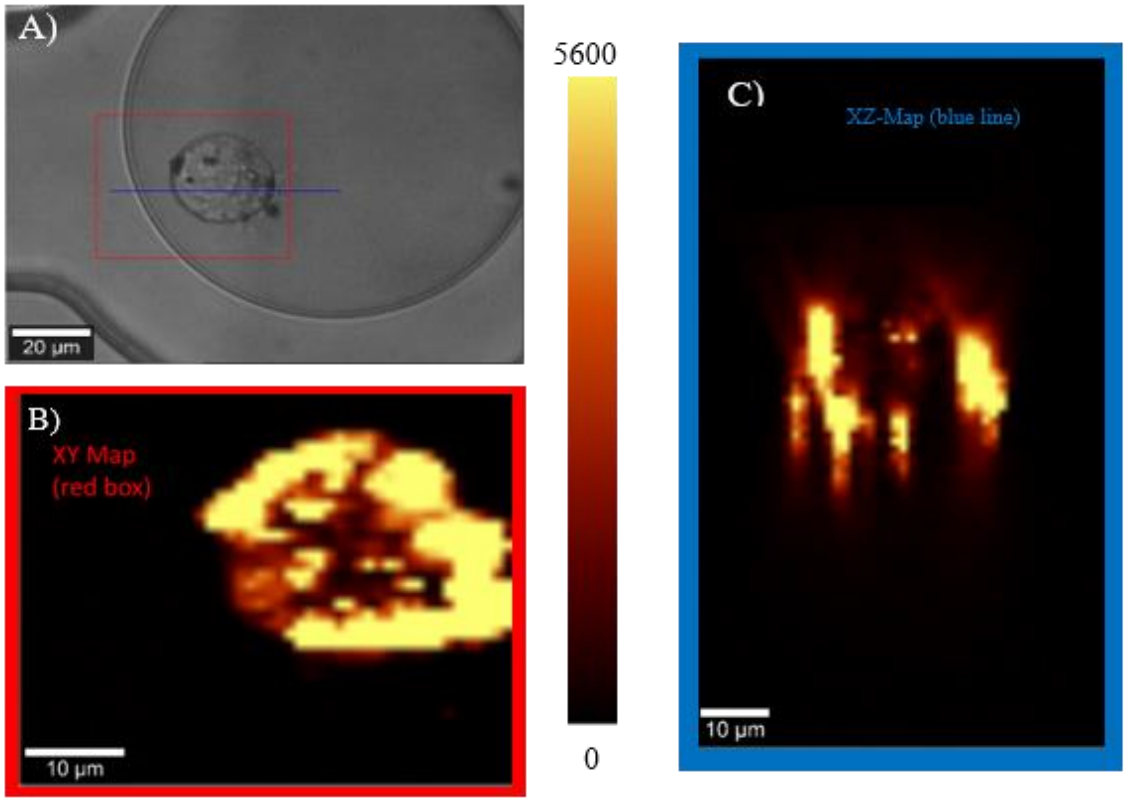

Figure 4.6. SI Figure 1. Optical image of a single PC3 cell encapsulate in a droplet. The red box corresponds to the XY mapping area and the blue line corresponds to the location of XZ map (A). XY SERS map represented by the red box processed in Project FOUR 4.1 (B). Raw XZ SERS map represented by the red box box processed in Project FOUR 4.1 (C).

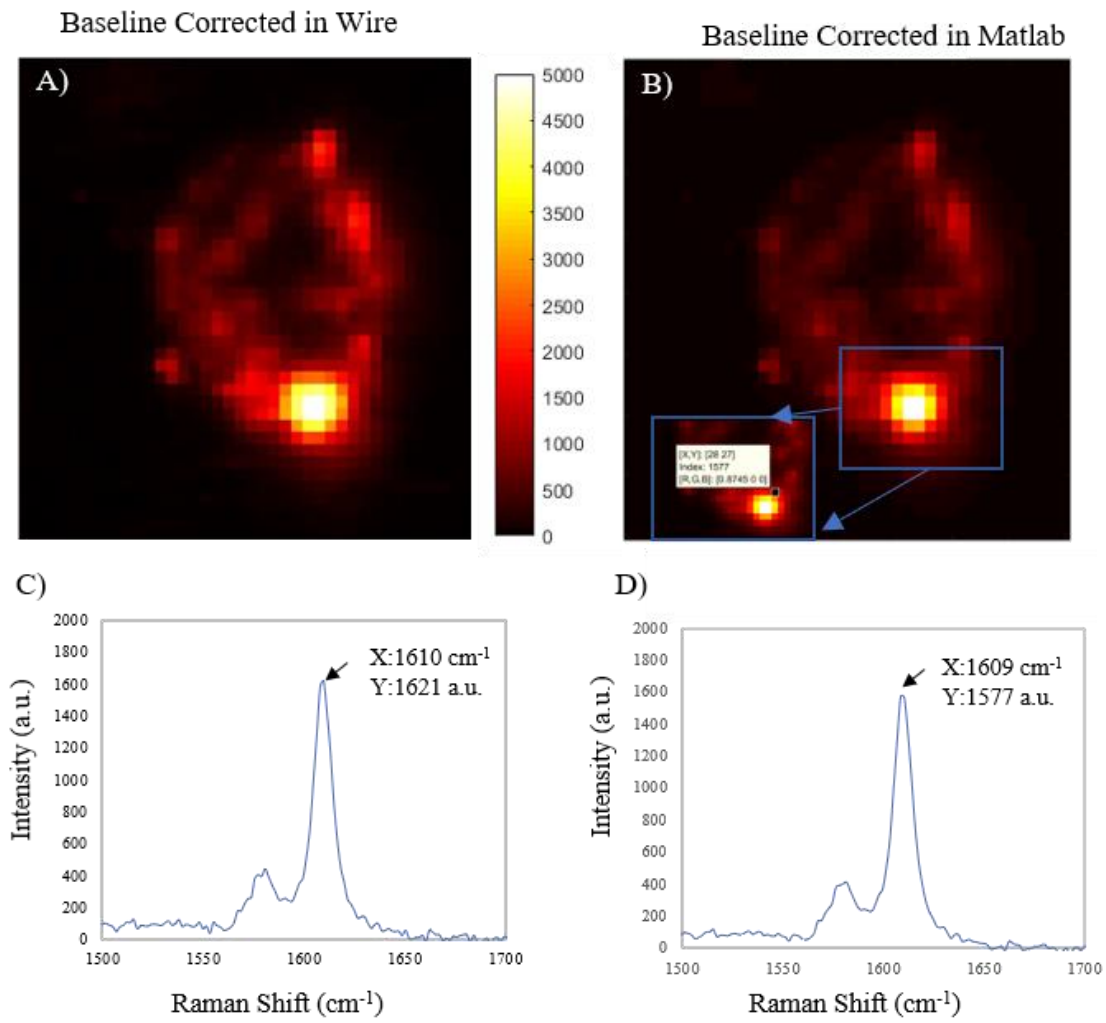

Figure 4.7. SI Figure 2. Demonstration of the efficacy of Matlab (A, C) baseline correction processing and map rendering by direct comparison to proprietary Wire 4.2 (B, D) processing. A and B show the rendered SERS maps scaled with same look up table (LUT). Image B inset shows the data from a single pixel and C and D show the spectra from the representative pixel. Images C and D show minor variation in the peak of interest as expected with different baseline correction algorithms.

Table 4-1. Table S1: Objective Details

Instrument	Setup	Objective	NA	Wavelength	δx (μm)	δy (μm)	δz (μm)	Volume (μm ^{3})
Renishaw	Inverted	20	0.40	633	0.97	0.97	7.91	7.37
Renishaw	Inverted	50	0.75	633	0.51	0.51	2.25	0.60
WITec	Upright	10	0.3	633	1.29	1.29	14.1	23.30
WITec	Upright	20	0.4	633	0.97	0.97	7.9	7.37
WITec	Upright	50	0.7	633	0.55	0.55	2.6	0.79

Table 4-2. Table S2: Coefficient of variation for the SERS maps within each experiment as calculated for the images processed in ImageJ and Matlab

	Coefficient of Variation	
Experiment	**Image J**	**Matlab**
1	0.42	0.40
2	0.49	0.36
3	0.50	0.28
4	0.45	0.35

Table 4-3. Table S3: Coefficient of variation for the fluorescence images as calculated in ImageJ

	Coefficient of Variation
Experiment	**Image J**
Experiment A – Replicate 1	0.51
Experiment A – Replicate 2	0.56
Experiment A – Replicate 3	0.42
Experiment B – Replicate 1	0.55
Experiment B – Replicate 2	0.46

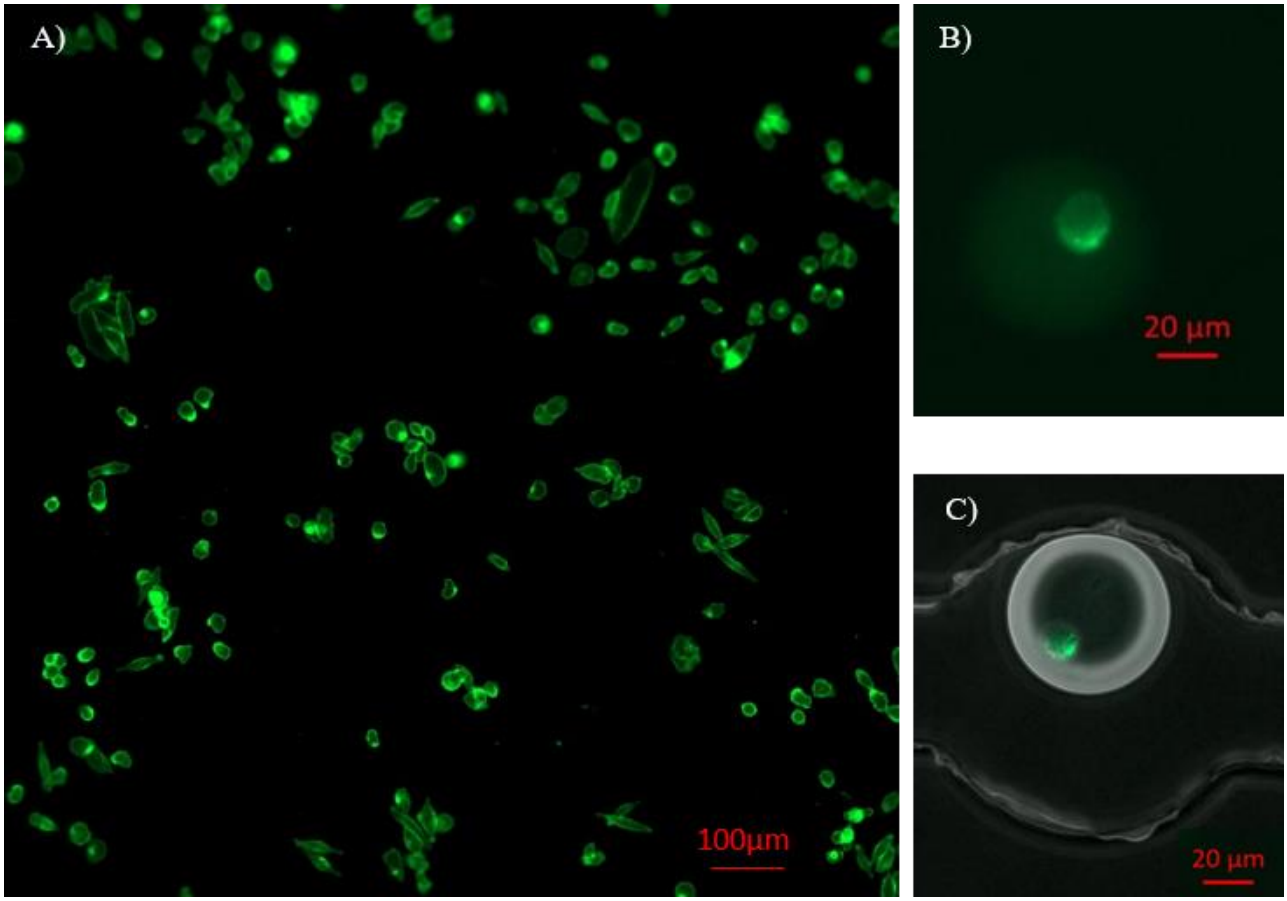

Figure 4.8. SI Figure 3. Fluorescence Images of PC3 cell tagged with wheat germ agglutin (WGA) functionalized with fluorescein (FITC) (Sigma,UK and Sigma, US). Large view image of tagged PC3 cells adhered to a 96-well plate (A). Fluorescence image of single cell encapsulation in the optofluidic platform (B). Image of a single cell encapsulation in the optofluidic with the fluorescence overlaid on the bright field image.

Chapter 5 Conclusions and Future Perspectives

The research presented in this dissertation crosses a broad swath of environmental applications of Raman spectroscopy. My interest in the development of nanosensors for environmental contaminants, **Chapter 2**, led me to study the broader impact of nanoscale phenomena in environmentally relevant questions. In **Chapter 3**, we explored the applications of Raman spectroscopy to characterize ester bonds and distinguish between esters located near electron donating groups and those on the aliphatic backbone of the polymer. **Chapter 4** contains the heart of the dissertation, a project that took nearly four years to complete and involved research on two continents. The development of the SERS optofluidics platform was a true interdisciplinary effort drawing on a wide range of expertise including surface chemistry, assay development, photonics and microfluidics. A key aspect of the platform development was the creation of an automated data processing tool to deal with the hundreds of maps collected from four different Raman instruments. Unexpectedly, the development of this tool allowed me to engage in a wide range of research projects and expanded my understanding of both fundamental SERS and aerosol chemistry.

Raman and SERS are promising tools for studying the environment. I think, however, that the widescale adoption and utilization of the technique faces several challenges:

1. Raman and SERS solutions are often discussed without reference or comparison to existing methods. The lack of conversation regarding which questions are best answered with SERS versus other methods, especially fluorescence, often leads others in the scientific community to view the Raman/SERS community as ‘tone deaf’. I believe a more honest conversation on how and why Raman and SERS complement other methods would aid in the broader adoption of Raman as an analytical technique. The research presented in this dissertation is focused on applications in which Raman provides a level of development not accessible through comparable fluorescence measurements.
2. Sensor development is too often undertaken by mono-disciplinary teams. The literature contains both reports from chemists that clearly underestimate the complexity of the biology and reports

from biologists that use nanoparticles without characterizing the material. An interdisciplinary approach is needed to intelligently design nanosenors for a specific application while appreciating the impact of sample preparation on the behavior of the pathogens. My work on the SERS optofluidics platform was slow because our collaboration lacked a dedicated cancer biologist. Our team contained a multitude of diverse expertise but we still faced challenges that would have been easier to address with the input of a biology expert.

3. SERS and Raman were initially developed for material characterization and therefore most of the commercial instruments are setup using an upright configuration. However, many more complex environmental questions are centered on the interaction between materials and organisms, which necessitate the use of an inverted microscope. The creation of commercially available inverted microscopes with environmental chambers would greatly benefit not only the research presented in this dissertation, but also the adoption of Raman by the environmental community.

Appendix A Synthesis of Highly Stable SERS pH Nanoprobes Produced by Co-Solvent Controlled AuNP Aggregation

(This chapter has been published in ***Analyst***.[1] This paper was published by The Royal Society of Chemistry.)

A.1 Abstract

Production of gold nanoparticle (AuNP) surface-enhanced Raman spectroscopy (SERS) nanoprobes requires replicable aggregation to produce multimers with high signal intensity. Herein, we illustrate a novel, yet simple, approach to produce SERS nanoprobes through control of co-solvent composition. AuNP multimers were produced by mixing AuNP monomers in water:ethanol co-solvent for variable periods of time. By varying the water:ethanol ratio and the amount of 4-mercaptobenzoic acid (4-MBA) present, the aggregation rate can be systematically controlled. Thiolated poly(ethylene glycol) was then added to halt the aggregation process and provide steric stability. This approach was used to produce pH nanoprobes with excellent colloidal stability in high ionic strength environments and in complex samples. The pH probe exhibits broad pH sensitivity over the range 6-11 and we calculate that a single AuNP dimer in a 35 fL volume is sufficient to generate a detectable SERS signal. As a proof-of-concept, the probes were used to detect the intracellular pH of human prostate cancer cells (PC-3). The internalized probes exhibit a strong 4-MBA signal without any interfering bands from either the cells or the culture media and produce exceptionally detailed pH maps. pH maps obtained from 19 xy surface scans and 14 yz depth scans exhibit highly consistent intracellular pH in the range of 5 to 7, thus indicating the greater reliability and reproducibility of our pH probes compared with other probes previously reported in the literature. Our water:ethanol co-solvent production process is fast, simple, and efficient. Adjustment of solvent composition may become a powerful way to produce SERS tags or nanoprobes in the future.

A.2 Introduction

Gold nanoparticles (AuNPs) are widely used for surface-enhanced Raman scattering (SERS) based sensing due to their strong localized surface plasmon resonance (LSPR), low toxicity, and long-term stability.[2-6] It is generally accepted that the largest SERS signals or "hot spots" are generated in the narrow gap between two AuNPs as a result of the strong electromagnetic coupling in that region.[7, 8] Reproducible production of SERS "hot spots" is non-trivial and requires that AuNP aggregation be neither too minimal (leaving too many monomers and a weak signal), nor too extensive (resulting in an unstable colloid). Controlled aggregation as a mechanism to produce "hot spots" has attracted extensive research attention and the use of small organic molecules as nanoparticle linkers has been deemed to be one of the more efficient ways to bridge nanoparticles.[9-15] For example, Taylor et al. used a cucurbit [n]uril "glue" to produce reproducible and controlled AuNP aggregates with a gap distance of 0.9 nm.[14] Aggregation inducers occupy a portion of the "hot spot" volume and generate peaks in the SERS spectrum. For this reason, SERS nanoprobes (defined as an AuNP multimer containing two or more AuNP monomers) are often produced using a Raman active linker. We and others have illustrated that malachite green isothiocyanate (MGITC), 2-aminothiolphenol (2-ATP), and 3,5-dimercaptobenzoic acid linkers can produce nanoprobes with intense, but reproducible SERS signals.[9, 12, 16] One substantial challenge, however, is that not all desired SERS applications utilize organic molecules that induce aggregation and bridge nanoparticles.

To date, a number of nanoparticles for SERS based determination of pH have been reported in the literature.[9, 15-23] The pH sensing capacity of these nanoparticles is generally realized via surface functionalization of the particle with a pH sensitive molecule whose SERS spectrum changes as a function of pH. For example, 4-aminothiolphenol, 2-aminothiolphenol, 3-amino-5-mercapto-1,2,4-triazole, and 4-mercaptobenzoic acid (4-MBA) are often employed due to the pH sensitivity of the SERS band of the amine or carboxyl groups of these molecules. Amongst these, 4-MBA exhibits a broad pH sensitive range, simple structure, high photochemical stability, and thiol mediated AuNP surface affinity.[17, 22-25] Arguably the most

common way to synthesize 4-MBA-AuNPs is to dilute a concentrated 4-MBA ethanol solution in an aqueous AuNP suspension.[17, 24, 26] Unfortunately, 4-MBA does not effectively induce AuNP aggregation and thus the SERS probes produced by this approach exhibit a weak and irreproducible signal. Lawson et al. improved probe reproducibility and signal intensity by utilizing 3,5-dimercaptobenzoic acid as both the pH indicator and aggregation inducer.[9] However, the three step organic reaction required for the synthesis of 3,5-dimercaptobenzoic acid is mechanistically challenging and thus not feasible for widespread use. While there is substantial interest in the production and potential application of SERS based pH sensors, the syntheses reported to date have generally resulted in particles of only transient colloidal stability and weak signal due to the limited ability for the aforementioned molecules to induce nanoparticle aggregation and form stable nanoprobes.

Past studies have shown that AuNPs aggregate more rapidly in the presence of ethanol than in water due to the lower polarity of the alcohol.[27] We hypothesized that addition of ethanol to an aqueous suspension of AuNPs would reproducibly change the solvent properties and thus enable controlled AuNP aggregation. Such an approach has three potential advantages: 1) Coordinated changes in solvent properties should enable control of the aggregation rate such that reproducible aggregates can be produced both in the presence and absence of a SERS active organic molecule; 2) Once stable aggregates are formed, excess ethanol can be removed by centrifugation; and 3) Because no complicated organic syntheses are required, this method may be more sustainable and thus more cost-efficient than many extant methods. With this rationale, we set out to test whether a water:ethanol co-solvent system could be used to control AuNP aggregation and produce AuNP-based SERS nanoprobes.

Through the use of water:ethanol co-solvent mixtures we can systematically produce AuNP multimers of controlled size (Figure A**.1**). Multimers of size appropriate for SERS were formed in 50:50 water:ethanol co-solvent and then following functionalization with a protective HS-PEG layer a highly stable SERS pH probe was produced. Compared with previously used BSA and silica coatings, PEG has a long hydrophilic chain that does not inhibit proton diffusion to the SERS hot spots.[20, 26] This pH nanoprobe illustrates high

SERS activity, high pH sensitivity, a broad pH sensitive range, and excellent stability in high ionic strength environments. To our knowledge this is the first time that co-solvents have been used for SERS pH probe production. This approach can be easily extended to produce numerous types of SERS probes through controlled adjustment of co-solvent type and concentration.

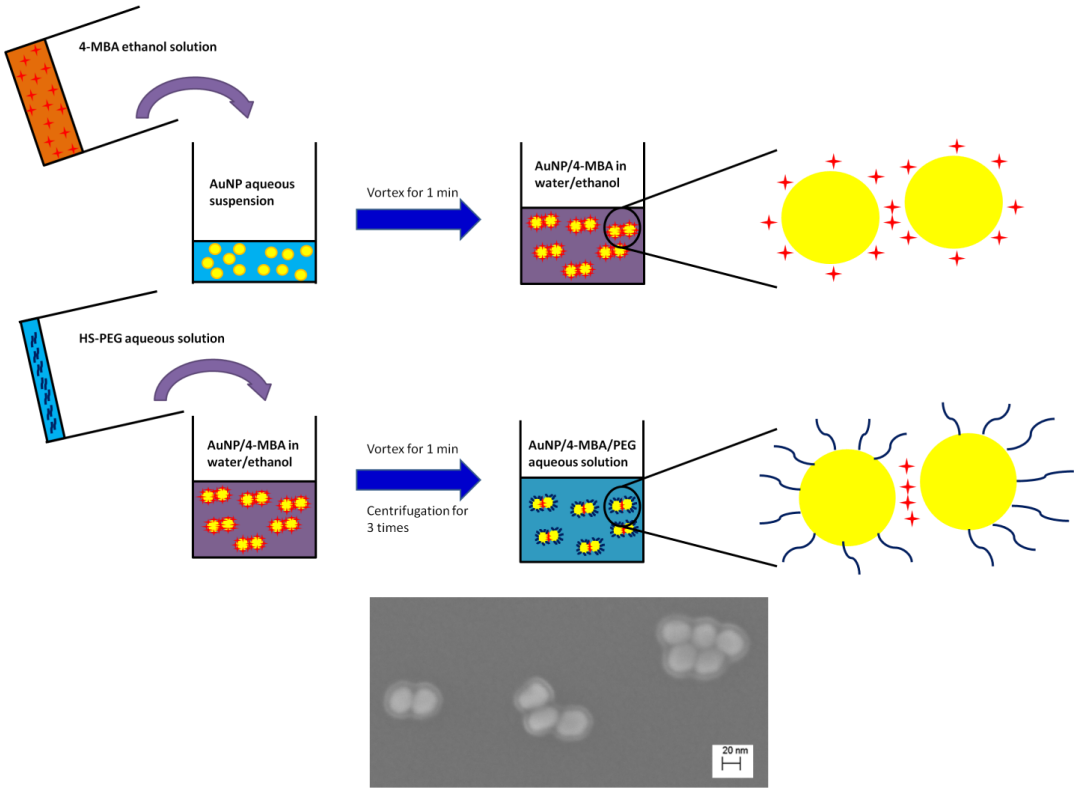

Figure A.1. Production of AuNP/4-MBA/PEG nanosensor.

A.3 Experimental Section

A.3.1 Materials

Gold chloride trihydrate ($HAuCl_4 \cdot 3H_2O$), sodium citrate tribasic dihydrate ($Na_3Citrate \cdot 2H_2O$), 4-Mercaptobenzoic acid (4-MBA), and phosphate buffer (PB) solution were purchased from Sigma-Aldrich. Thiolated poly(ethylene glycol) (HS-PEG; 5 kD) was purchased from Nanocs. Anhydrous ethanol was purchased from Fisher Scientific.

A.3.2 AuNP Synthesis

AuNPs were synthesized using the seed-mediated approach. Briefly, 13 nm gold nanoparticle seeds were synthesized according to Frens.[28] $Na_3Citrate{\cdot}2H_2O$ (final concentration 3.88 mM) was added to 100 mL of boiling 1 mM $HAuCl_4{\cdot}3H_2O$ under vigorous mixing conditions. The reaction was allowed to run until the solution color changed to wine red, indicating completion. During seed synthesis the pH was controlled at 6.2-6.5 to improve their monodispersity.[29] Following seed synthesis, 35 nm AuNPs were synthesized by seed-mediated growth.[30] A 250 mL flask containing 100 mL of $HAuCl_4{\cdot}3H_2O$ solution (0.254 mM) was heated to boil under vigorous stirring. To this flask was added 2.02 mL seed suspension and 0.44 mL $Na_3Citrate{\cdot}2H_2O$ (final concentration 0.17 mM). After a 40 min reaction time the flask was cooled to room temperature.

A.3.3 AuNP Aggregation in Water:Ethanol Co-Solvent

AuNPs suspended in water:ethanol mixtures of varying ethanol content were prepared by adding 0.5 mL of a water:ethanol mixture (ethanol content 0-100%) to 0.5 mL of aqueous AuNP suspension. The mixture was then vortexed for 1 min to ensure complete mixing of the components. The kinetics of AuNP aggregation in the water:ethanol mixtures were investigated by monitoring the variation in the UV-VIS extinction spectra and the DLS determined hydrodynamic diameter over a two day period. 4-MBA-AuNPs in water:ethanol co-solvent were prepared by adding 0.5 mL 4-MBA in ethanol (100 μM) to 0.5 mL AuNP aqueous suspension. We emphasize that the 4-MBA solution and the AuNP suspension were mixed at a 1:1 volumetric ratio. Equal volume mixing of the two components results in more homogeneous adsorption of 4-MBA and more highly controlled AuNP aggregation.[31] The aggregation kinetics of 4-MBA functionalized AuNPs in water:ethanol co-solvent were investigated by both UV-VIS extinction spectra and DLS. SERS spectra of 4-MBA-AuNPs in solutions with different ethanol contents were collected at 100 min after the mixing of 0.5 mL AuNP suspensions and 0.5 ml 4-MBA solutions with ethanol contents 12.5-100%.

A.3.4 Production of Colloidally Stable SERS pH Probes

The procedure for production of our SERS probe is shown in Figure A**.1**. First, 0.5 mL of 100 μM 4-MBA in ethanol was added to 0.5 mL of aqueous AuNP suspension and then fully mixed by vortexing. After 10, 55, 100, or 140 min, 100 μL of HS-PEG aqueous solution (500 μM) was added to the mixture. The suspension was kept for 20 min at room temperature and subsequently washed by centrifugation 3× to remove excess 4-MBA, HS-PEG, and ethanol. Following centrifugation, the supernatant was discarded and the sediment was redispersed in 1 mL water.

A.3.5 Evaluation of the Sensitivity and Stability of the pH Probe

To evaluate the pH sensitivity of our probe, 1 mL of probe was added to 1 mL of PB solution (20 mM) with different pH. The pHs of the mixtures were also measured by a commercial pH meter (Accumet AB15 plus, Fisher Scientific) and their corresponding SERS spectra were recorded. A pH calibration curve was produced by plotting the change in the SERS spectra versus pH. To evaluate the colloidal stability of the probe, 1 mL probe was added to 1 mL PB solution (20 mM) and variations in DLS determined hydrodynamic diameter, UV-VIS extinction spectra, and pH indicator values were monitored for one hour. To further test the capacity of the probe (200 μL) it was also added to 800 μL of two different soft drinks (Fanta orange and club soda) and tap water. SERS spectra were acquired and the derived pH values were compared with those measured by the commercial pH meter.

A.3.6 Intracellular pH Monitoring

A human prostate cancer cell line, PC-3, was cultured in F-12K Medium (Kaighn's Modification of Ham's F-12 Medium) (ATCC) supplemented with 10% fetal calf serum and 1% penicillin/streptomycin. Cells were grown to confluence in an incubator at 37 °C with 5% CO_2 prior to harvesting using trypsin/EDTA. A cell concentration of 2.4 x 10^4 cells/mL was then seeded into a 6-well plate (volume of cell medium). Cells were then incubated overnight in an incubator at 37 °C with 5% CO_2. Each well was then inoculated with 20 μl of nanoprobes and left in the incubator overnight. After approximately 24 hours the cells were washed three times with PBS before being imaged.

A.3.7 Instrumentation

Pristine AuNP size (35±1 nm, n=40) was measured by field-emission scanning electron microscopy (FESEM, LEO (Zeiss) 1550) and transmission electron microscopy (TEM, JEOL JEM-1400) with the assistance of Image J (Figure A.**2**). Pristine AuNP size (39 nm) was also measured by dynamic light scattering (DLS, Nano Zetasizer, Malvern). The LSPR of the AuNPs as well as AuNP aggregates was characterized by UV-VIS spectroscopy (Cary 5000, Agilent). Raman spectra were acquired by a Raman spectrometer (Alpha500R, WITec) with a 10× objective and 0.5 s integration time. The 785 nm laser light was dispersed by a 300 gr/mm grating and detected by a Peltier CCD. Each Raman spectrum reported (unless noted otherwise) was an average of 400 single spectra acquired across a 1000 μm × 1000 μm Raman map. The cells were directly imaged in the 6-well plate using a 785nm laser, 50x objective and a 0.05 second integration time.

A.3.8 SERS Data Processing

The SERS data for the calibration curve and cell experiments was imported into MATLAB® 2015b (The Mathworks, USA). The spectra were first baseline corrected using an asymmetric least squares fitting,[32] the intensities of the peaks of interest (1084cm^{-1}, 1410 cm^{-1} and 1710 cm^{-1}) were tracked and ultimately ratios between the pH insensitive and pH sensitive peaks were plotted. A calibration curve with a Boltzmann fit was established using Origin 8.0 to describe the relationship between the pH and SERS peak ratios. The pH was then calculated at each of the points in the SERS maps and a visual representation was rendered in Matlab. The data from all the cell experiments was further compiled and analyzed in Matlab.

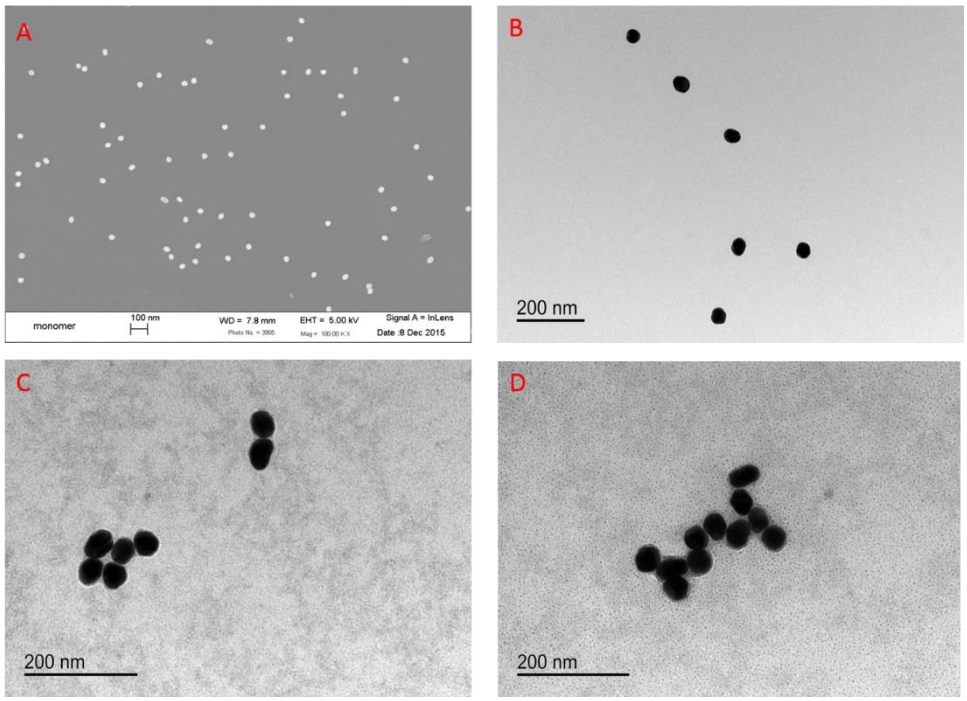

Figure A.2. A) Scanning electron microscopy image of the pristine AuNPs spin coated on a silicon wafer; Transmission electron microscopy images of pristine AuNP monomer (B), and PEG-coated AuNP aggregates (C&D).

A.4 Results and Discussion

A.4.1 Controlled AuNP Aggregation in Water:Ethanol Co-Solvent

AuNPs synthesized by sodium citrate reduction are stable in the absence of salt due to the negative charge imparted by surface associated citrate and its degradation products.[29, 33] Ethanol, however, is known to induce AuNP aggregation due to dipole-dipole attractive interactions.[27] Herein, we observed that changes in the ethanol co-solvent concentration greatly affected AuNP size and colloidal stability. For ethanol co-solvent concentrations of 0-25% the hydrodynamic diameter proportionally increased with the ethanol content (Figure A.**3**). AuNP multimers produced in water:ethanol cosolvent mixtures below 50:50 were stable over a two day period, while those produced at a 50:50 water:ethanol ratio exhibited more extensive aggregation. Because aggregate formation is vitally important for "hot spot" formation and SERS nanoprobe production, we focused on the 50:50 water:ethanol mixture (referred to as a water:ethanol co-solvent hereafter).

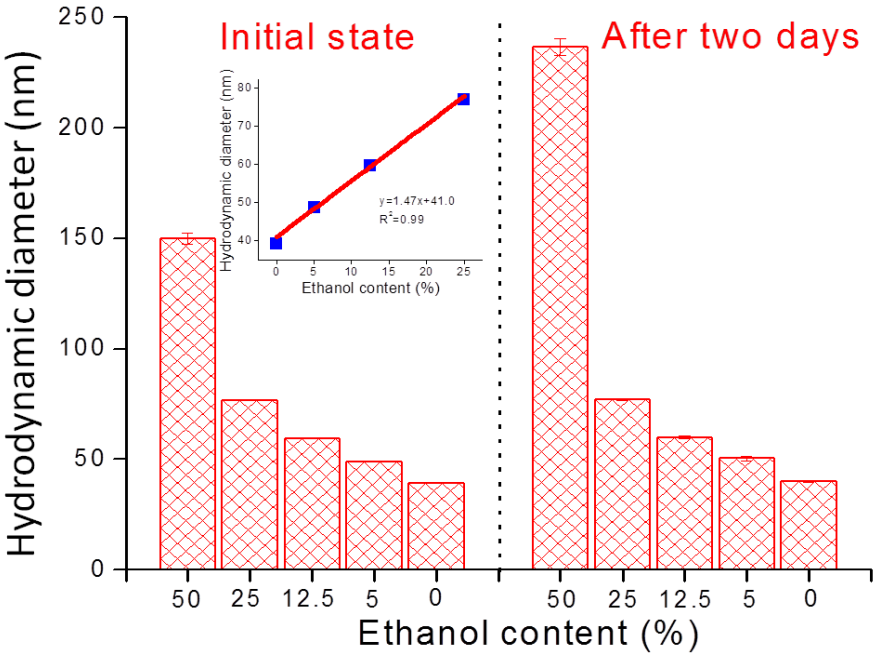

Figure A.3. Size of AuNPs dispersed in water/ethanol mixture with different ethanol content; Inset figure shows the linear relationship between AuNP size and the ethanol content when it is below 25%.

An immediate increase in the AuNP hydrodynamic diameter from 39 to 150 nm was observed in water:ethanol co-solvent, while no change was observed in water alone (Figure A.**4**A). In co-solvent, the AuNP hydrodynamic diameter increased slowly from 150 to 188 nm during the first hour. After two days the AuNP size ultimately reached 236 nm and the colloid was colloidally stable (Figure A.**3** and inset of Figure A.**4**A). We attribute the rapid AuNP aggregation in water:ethanol co-solvent to the systematic variation of the solvent dielectric constant. As shown in Equation A-1, the electrostatic repulsive force (V_{elec}) supporting AuNP stability is proportional to the solvent dielectric constant ε when other parameters (φ is the surface potential, h is the gap between two particles, and k is the inverse of Debye length) remain constant.[34] Addition of ethanol (ε = 24.4) to water (ε = 80.1) leads to a smaller dielectric constant in co-solvent than in water alone, which in turn decreases the electrostatic repulsive force between AuNPs.

$$V_{elec} = 2\pi\varepsilon a\varphi^2 \ln(1+e^{-kh}) \qquad \text{Equation A-1}$$

4-MBA functionalized AuNPs exhibited completely different aggregation kinetics compared with the pristine AuNPs. The 4-MBA-AuNP hydrodynamic diameter slightly decreased in the initial ~40 min and then increased from 40 to 180 min, thus indicating that aggregation is minimal for the first ~40 min and then proceeded more rapidly until the colloids were no longer colloidally stable. Control suspensions of AuNPs and 4-MBA-AuNPs in DI water exhibited no sign of aggregation (Figure A.**4**A).

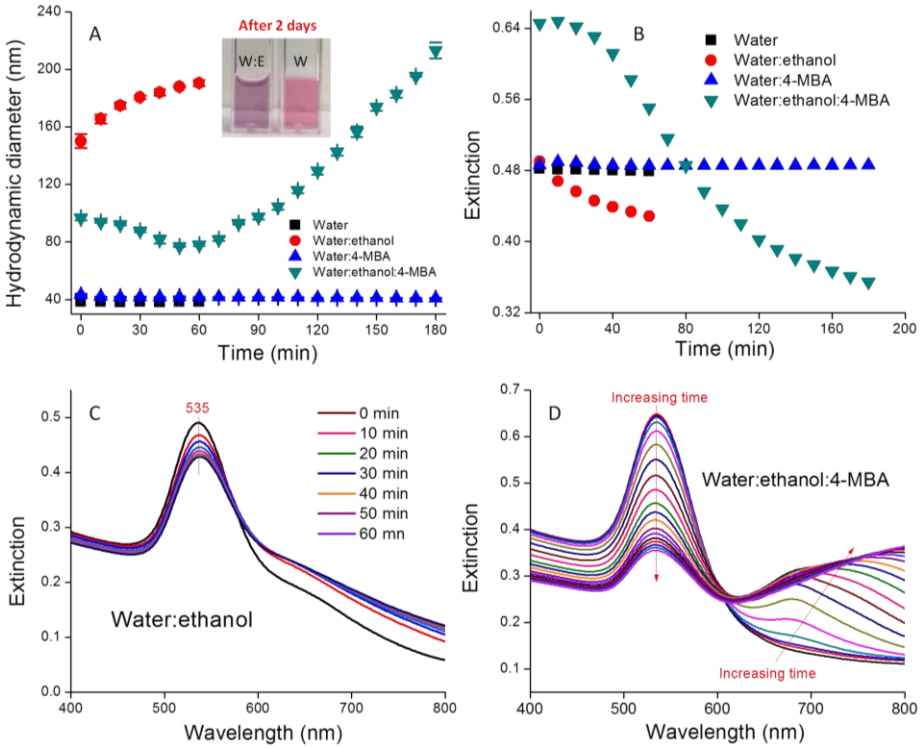

Figure A.4. A) Temporal variation of the DLS determined hydrodynamic diameter of AuNPs dispersed in water and 50:50 water:ethanol in the presence and absence of 4-MBA; Inset photos are of AuNPs in water and 50:50 water:ethanol after two days; B) Temporal variation in the extinction of the primary LSPR band for AuNPs dispersed in water and 50:50 water:ethanol in the presence and absence of 4-MBA; C) Extinction spectra of AuNPs in water:ethanol as a function of time, and D) Extinction spectra of AuNPs in water:ethanol:4-MBA as a function of time.

UV-VIS spectroscopy results are consistent with the DLS data. The extinction spectra of AuNPs in water:ethanol co-solvent exhibited a primary LSPR band at 535 nm and a secondary LSPR band at ~650 nm, thus indicating AuNP aggregation (Figure A.**4**C). As time increased from 0 to 60 min, the primary LSPR band gradually decreased in magnitude, while the secondary band simultaneously increased (Figure A.**4**C). To quantitatively illustrate this change we plot the height variation of the primary LSPR band as a function of time in Figure A.**4**B. This figure demonstrates that AuNP aggregation in water:ethanol co-

solvent occurs rapidly at the beginning and then occurs more slowly, thus resulting in the long-term stability of the suspension.

Similar to the DLS results, the extinction spectra of 4-MBA-AuNPs in water:ethanol co-solvent exhibited different time-dependent variation relative to pristine AuNPs (Figure A**.4**B&D). Over the first 40 min, the spectra remained almost constant, thus indicating no obvious aggregation. Following this short delay, the LSPR band at 535 nm decreased at a rate comparable to the increase in the intensity of the band at 650 nm until 2 h. After 2 h, the bands at 535 nm and 650 nm decreased, while a third band at 750 nm developed. Unlike pristine AuNPs, the 4-MBA-AuNPs in water:ethanol co-solvent were initially stable and then once aggregation was initiated it proceeded until the colloidal stability was completely lost by 12 h (data not shown). We attribute the delay in aggregation to the increase in solvent dielectric constant that occurs due to addition of a high concentration of 4-MBA (100 μM), which in turn results in an increase in V_{elec} (Equation A-1). At extended reaction times increasingly larger amounts of 4-MBA have adsorbed onto the AuNPs and this leads to a decrease in the local dielectric followed by the onset of aggregation. Such speculation is supported by the fact that no delay in the onset of aggregation was observed when the 4-MBA concentration was decreased by 10×, 100×, or 1000×, thus suggesting that low 4-MBA concentrations are insufficient to change the local dielectric (Figure A**.5**). For low 4-MBA concentrations, the initial AuNP size is highly dynamic because of rapid initial aggregation (data not shown). Because of the delay in the onset of aggregation that occurs in the presence of high 4-MBA concentrations, the point at which aggregation is initiated can be easily pinpointed and the entire aggregation process can be well controlled.

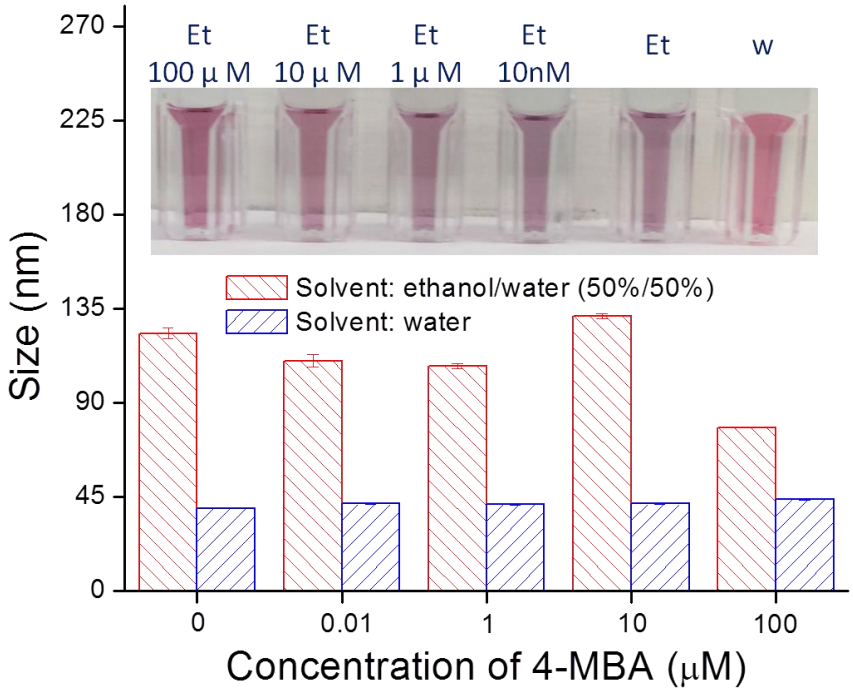

Figure A.5. Size of 4-MBA coated AuNPs in water and water:ethanol co-solvent with different 4-MBA concentrations; Insets are photos of MBA coated AuNPs in water and water:ethanol co-solvent with different 4-MBA. All the results are at time = 0 h.

The extinction spectra of the AuNPs and 4-MBA-AuNPs in water remain stable over a three-hour period (Figure A.**6**), thus demonstrating the important role of ethanol to accelerate aggregation. The role of 4-MBA in AuNP aggregation in water:ethanol co-solvent can thus be concluded: 1) to stabilize the colloid in the first 40 min due to the increase in solvent dielectric constant; 2) to promote aggregation after 40 min due to the decreased stabilizing capacity of 4-MBA relative to the citrate AuNP surface coating. The synergistic interplay between the ethanol and 4-MBA concentrations in dictating AuNP aggregation enables reproducible and stable pH probe production, as shown in the following sections.

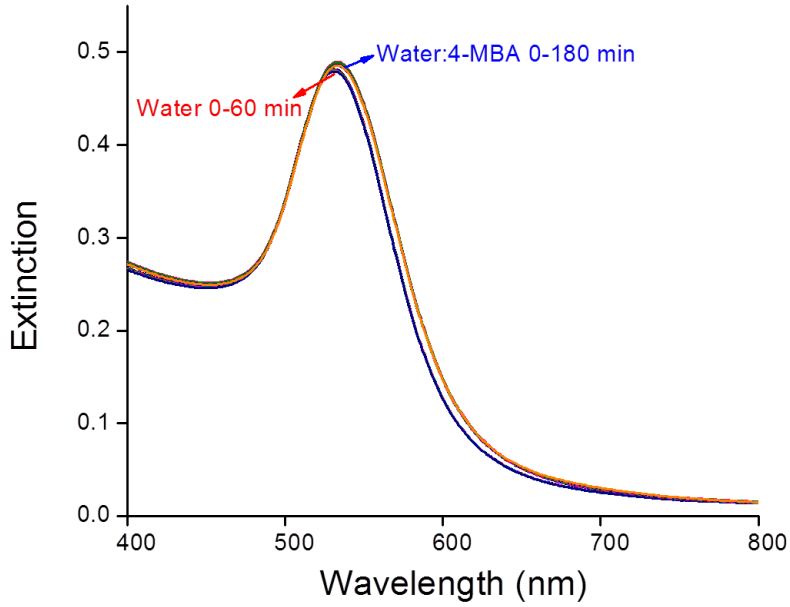

Figure A.6. Extinction spectra of AuNPs and 4-MBA coated AuNPs in water as a function of time.

A.4.2 SERS of 4-MBA-AuNPs in Water:Ethanol Co-Solvent

The variation in the SERS spectra for 4-MBA-AuNPs in water:ethanol co-solvent was monitored every 6 min for 3 h (Figure A.**7**). At t=0, only the ethanol spectrum was apparent with a prominent band at 886 cm^{-1}. The intensity of this band remained constant over the 3 h reaction period because of the fixed ethanol content. With time, the characteristic bands of 4-MBA (528, 698, 1084, 1286, and 1597 cm^{-1}) appeared and increased in magnitude from 0 to 168 min (Figure A.**7**A). In comparison, the Raman bands of 4-MBA-AuNPs in water alone were approximately 260× weaker than in water:ethanol co-solvent. Such a result highlights the importance of producing multimers containing "hot spots" to achieve an intense SERS signal and succinctly illustrates the important role that ethanol plays in AuNP aggregation and in the generation of a strong 4-MBA SERS signal.

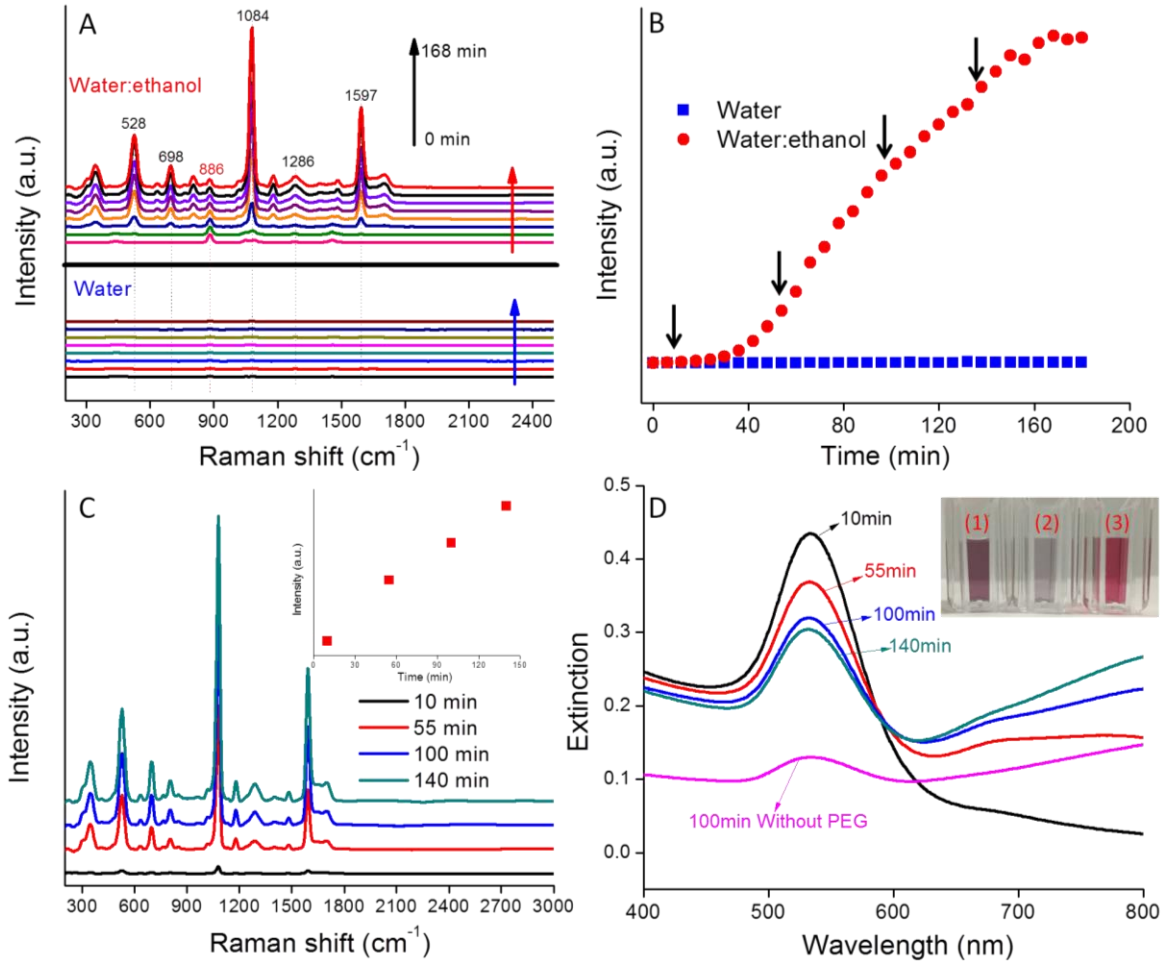

Figure A.7. A) Selected SERS spectra of 4-MBA-AuNPs in water and water:ethanol mixture over three hours; B) SERS intensity variation of band at 1084 cm^{-1} as a function of time; C) SERS spectra of 4-MBA-AuNPs after PEG coating at different times; D) UV-VIS extinction spectra of 4-MBA-AuNPs coated with HS-PEG at different times as well as without the HS-PEG coating; Inset is the photo of (1) AuNP monomer colloid, (2) 4-MBA-AuNPs without HS-PEG coating after centrifugation; and (3) 4-MBA-AuNPs with HS-PEG coating after centrifugation.

To quantitatively show the time-dependent variation in SERS signal, the intensities of the Raman band at 1084 cm^{-1} for 4-MBA-AuNPs in water and in water:ethanol co-solvent were compared (Figure A.**7**B). In water:ethanol co-solvent, the SERS intensity was constant for the initial 40 min, a period that corresponds to the aggregation delay depicted in Figure A.**4**A&B. This result demonstrates that AuNP aggregation is crucial for the generation of a strong SERS signal. Between 40 and 160 min, the SERS intensity increased steadily, due to enhanced coupling between the developing LSPR band in the NIR region and the 785 nm incident laser wavelength (Figure A.**4**D).[12] Between 160 and 180 min the SERS intensity plateaued, a result that may be due to the depletion of sufficient numbers of AuNP monomers to feed the growing multimer population (Figure A.**7**B). We note that all the 4-MBA Raman bands varied simultaneously with a change

in aggregation state, thus indicating aggregation state had no influence on the peak ratios, a result that is consistent with the literature.[20]

SERS spectra of 4-MBA-AuNPs in solutions with different ethanol contents were also collected. As shown in Figure A**.8**, the SERS signal generally decreased with the decrease of ethanol content, which was attributed to the ineffective aggregation of AuNPs in solutions with lower ethanol contents. There is a substantial SERS signal enhancement when ethanol content increased from 25-50%. This indicates the ethanol content threshold that could effectively induced AuNP aggregation lies in between 25-50%, which is supported by the results in Figure A**.3**. Overall, these results suggested that the change of solution dielectric constant induced by ethanol can be effectively applied to control AuNP aggregation and thus enhance their SERS signal.

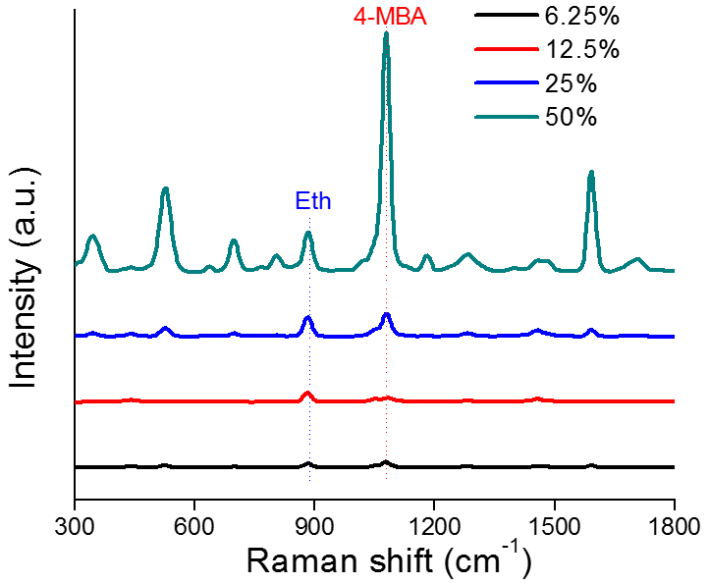

Figure A.8. SERS spectra of 4-MBA coated AuNPs in solutions with different ethanol contents.

A.4.3 Production of Colloidally Stable SERS pH Probe

Uncontrolled aggregation and flocculation limit the broad application and use of most of the currently described SERS pH probes.[16, 17, 24] A stable pH probe with broad pH sensitivity is desired to enhance reproducibility and enable real world applications. HS-PEG is recognized for its capacity to sterically stabilize AuNPs and thus we used it as a means to stabilize our nanoprobes.[35] We specifically investigated

the addition of HS-PEG to arrest nanoprobe aggregation. Accordingly, HS-PEG was added to aliquots of the reacting system depicted in Figure A**.7**B at the times denoted by the black arrows (10, 55, 100, and 140 min). Each of these times corresponds to a different extent of aggregation and thus variable SERS intensity. Two days after adding HS-PEG, the 4-MBA-AuNP extinction spectra remained virtually unchanged, thus indicating that HS-PEG can effectively quench the aggregation of the 4-MBA-AuNPs in water:ethanol (Figure A**.9**).

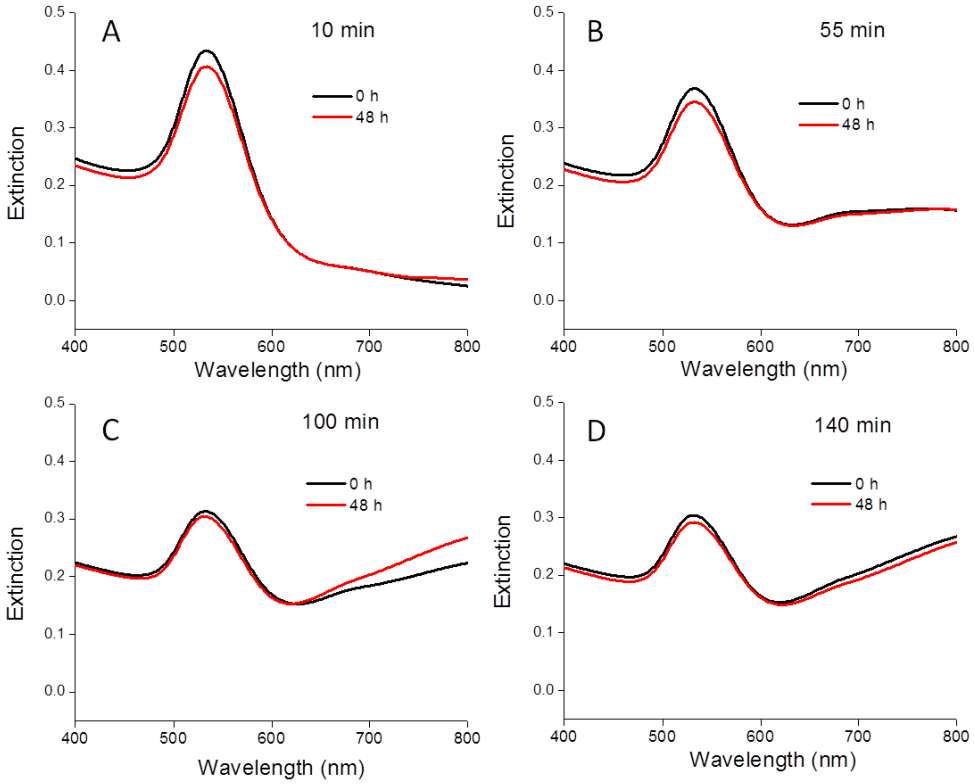

Figure A.9. UV-VIS extinction spectra of 4-MBA coated AuNPs in water/ethanol co-solvent 0 h and 48 h after adding HS-PEG.

After addition of HS-PEG, the nanoprobes were washed by centrifugation three times to remove excess 4-MBA, HS-PEG, and ethanol. Following each centrifugation, the supernatant was discarded and the solids were redispersed in water. Assuming each 4-MBA molecule occupies a 0.2 nm^2 area on the AuNP surface, the maximum number of 4-MBA molecules each AuNP can hold is 24,000.[23] Under our synthesis conditions the concentration of 4-MBA exceeded 300,000 molecules per AuNP and thus the AuNP surface should be saturated by 4-MBA. The added amount of HS-PEG was of similar concentration to that of 4-MBA and there was some concern that HS-PEG could replace 4-MBA on the AuNP surface and thus lower

the SERS intensity. However, as shown in Figure A**.10**, the addition of HS-PEG had no detrimental effect on the measured SERS intensity. This result suggests that HS-PEG either does not replace surface associated 4-MBA or does so only on the periphery of the AuNP clusters and not within the "hot spots" responsible for the intense SERS signal. Of these two hypotheses, the latter is supported by SEM images that illustrate 4-MBA-AuNP clusters consistently wrapped by a ~5.6 nm thick PEG layer (a thickness consistent with the 5k molecular weight[36]), but with interparticle junctions of only a few angstroms that are consistent with the expected spacing for SERS "hot spots" (Figure A**.1**). These results are corroborated by TEM images that show small AuNP clusters with PEG coatings (Figure A**.2**C&D).

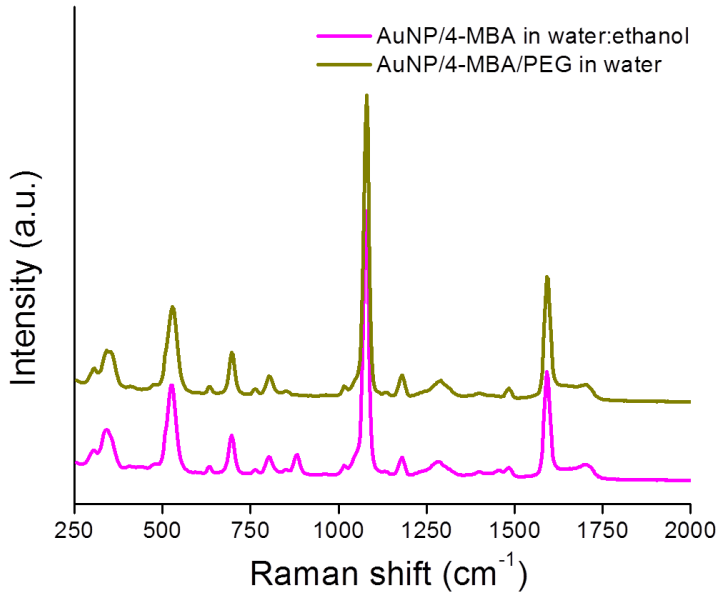

Figure A.10. SERS spectra of AuNP/MBA in water:ethanol co-solvent and AuNP/4-MBA/PEG in water at 100 min.

The absence of a peak at 886 cm^{-1} in the spectra for the washed probes (Figure A**.7**C) indicates that a majority of the ethanol initially present in the system was removed by centrifugation. We note that it is highly advantageous that the reagent used to induce AuNP aggregation can be easily removed following probe synthesis since it then does not occupy the SERS "hot spot" volume. The SERS intensity increased almost linearly with the coating time (Inset of Figure A**.7**C), which is consistent with the trend observed in the absence of the HS-PEG coating (Figure A**.7**B).

UV-VIS extinction spectra of HS-PEG coated 4-MBA-AuNPs after centrifugation are shown in Figure A**.7**D. With an increase in the HS-PEG coating time, the LSPR band at 535 nm gradually decreased while the band in the NIR region gradually increased, leading to the increase in SERS intensity (Figure A**.7**C). As a negative control, 4-MBA-AuNPs without HS-PEG were also washed by centrifugation. After washing, the extinction spectrum became almost flat (Figure A**.7**D) and the colloid color significantly faded (Inset of Figure A**.7**D), thus indicating that most of the 4-MBA-AuNPs were lost by the irreversible formation of large aggregates during centrifugation. As a comparison, the colloid with a HS-PEG coating showed dark purple color (Inset of Figure A**.7**D), highlighting the important role of HS-PEG for colloid stability. An ideal pH probe should be able to generate high SERS intensity as well as stay suspended in water for an extended period of time (i.e., the aggregates cannot be too large). Balancing these two aspects, 4-MBA-AuNPs coated with HS-PEG at 100 min were selected as the best pH probe and further tested.

A.4.4 pH Nanoprobe Sensitivity and Stability

The pH sensitivity of our nanoprobe was tested in phosphate buffer (PB) solutions of different pH. As shown in Figure A**.11**A, the SERS spectra varied with pH. The bands at 1410 ($-COO^-$) and 1710 cm^{-1} (-COOH) increased or decreased in intensity, respectively, as well as slightly shifted with an increase of solution pH, while the Raman band at 1084 cm^{-1} (benzene ring) remained constant. This result indicates that the protective PEG layer is permeable to H^+ and does not detrimentally affect the pH sensitivity of the probe. We note that this probe exhibits high SERS intensity at both extremely acidic (pH=1.2) and basic (pH=12.6) conditions. These high ionic strength conditions normally result in colloidal instability, thus the high signal intensities demonstrate the excellent stability conferred by the PEG coating (Figure A**.12**).

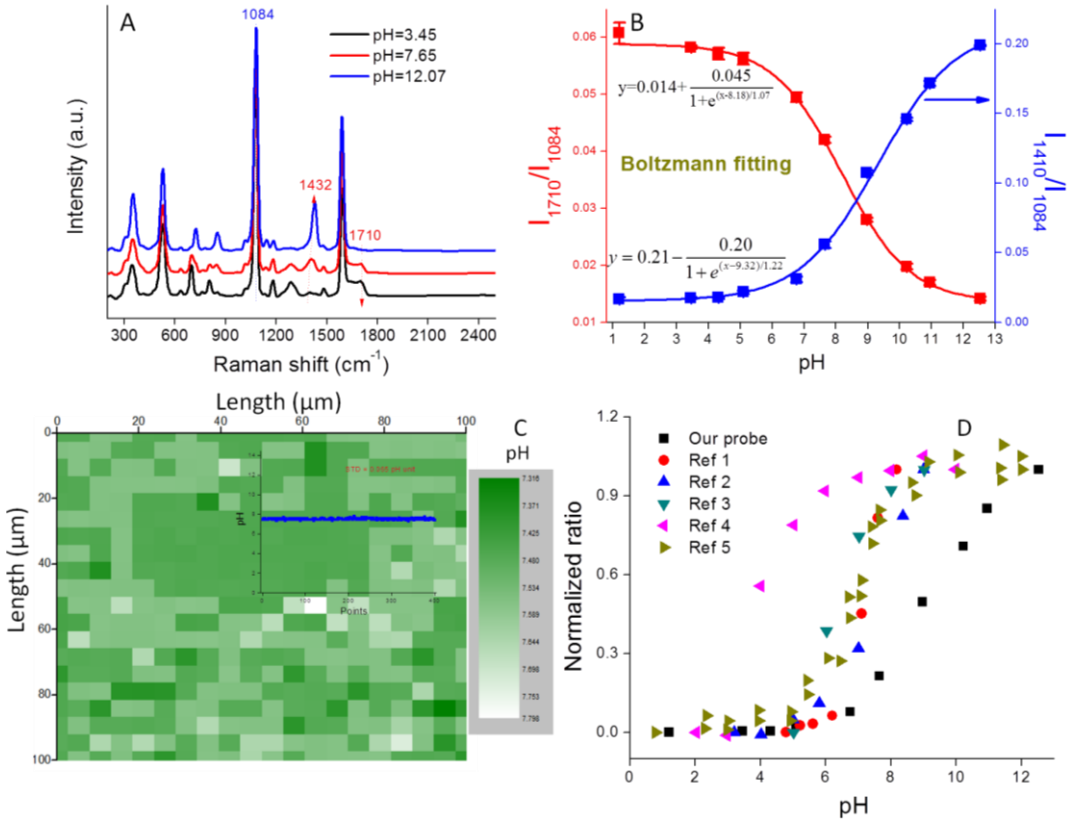

Figure A.11. A) SERS spectra of pH probe in PB buffer of different pH; B) pH calibration curve in the range 1-13; C) A Raman map containing 400 pixels, each pixel shows a pH value for a 3.5×10^{-11} mL volume; Inset figure: pH value variation of the 400 pixels from the Raman map; D) pH calibration curves from both our study and the literature for 4-MBA functionalized pH probes. The curves are normalized to their maximum values.[15, 17, 22, 24, 26]

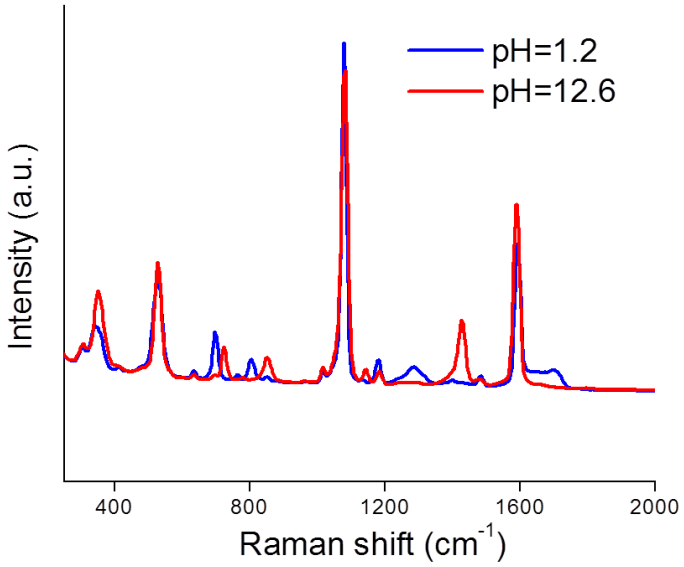

Figure A.12 SERS spectra of probe at pH=1.2 and 12.6.

Ratios of each of the pH-sensitive peaks (1410 cm^{-1} or 1710 cm^{-1}) relative to the pH-insensitive peak (1084 cm^{-1}) were plotted as a function of pH from 1 to 13 (Figure A.**11**B). In the acidic pH range of 1-6

and the basic range of 11-13, the intensity ratios (I_{1410}/I_{1084} and I_{1710}/I_{1084}) increase or decrease minimally, while in the 6-11 pH range, the ratios change much more dramatically, thus indicating that this is the most sensitive pH range for this probe. The pH calibration curves could be perfectly fitted using the Boltzmann expression (Figure A**.11**B) that has been previously applied to fit sigmoid shaped pH curves.[25] The linear portion of the curve covers five pH units, a range that is much broader than those reported in the literature for other 4-MBA based nanoprobes (Figure A**.11**D). This result can be attributed to both the high SERS intensity of our probes and their unique colloidal stability. We note that the derived pK_a value (8.75) is nearly 4 pH units higher than that of bulk 4-MBA (4.79). Such a large pK_a discrepancy between nanostructure associated 4-MBA and its bulk value has been previously reported and can be attributed to changes in surface topography and electron density.[37, 38] pH measurements obtained with this nanoprobe are highly reproducible (STD<5% for three parallel measurements) due to their well controlled aggregation and stability (Figure A**.11**B).

Most recently, Zheng et al. utilized bovine serum albumin (BSA) to stabilize their pH nanoprobes.[20] However, due to the nonspecific mechanism by which BSA associates with the nanoprobes, the resulting nanoprobes were difficult to reproduce and had limited shelf stability. Importantly, Zheng et al. attributed the majority of their SERS signal to the presence of small numbers of dimer and trimer AuNP aggregates that formed following BSA addition. Such a result supports our focus on the systematic production of colloidally stable AuNP aggregates of fixed size. Wang et al. developed silica shell-coated AgNP pH probes and successfully prevented BSA from contaminating the AgNP surface.[26] However, the reverse microemulsion method utilized for this synthesis is chemical-intensive and time-consuming. Also the silica shell limited the diffusion of protons to the AgNP surface, making the pH sensitive range very narrow (pH 3-6). We note that none of the previously reported probes exhibit stability over the broad pH range of 1-13 that we report here.

A significant advantage of nano-sized pH probes is their capacity to provide high spatial resolution and their potential to quantify pH within microenvironments. The laser spot size of a Raman microscopy system

limits the resolution that can be achieved by a SERS probe. For our probe and our microscope objective this spot size is described in the lateral ($\delta_{lateral}$ = 1.6 μm) and axial (vertical) dimensions (δ_{axial} = 17.4 μm) using Equation A-2 and Equation A-3, where λ is the laser wavelength, and NA (numerical aperture) is the characteristic parameter of an objective. Assuming a cylindrical laser spot, the minimum volume that can be detected is 35 fL. This volume is much smaller than that can be detected by commercial pH meter.

$$\delta_{lateral} = \frac{0.61\lambda}{NA} \qquad \text{Equation A-2}$$

$$\delta_{axial} = \frac{2\lambda n}{(NA)^2} \qquad \text{Equation A-3}$$

A 1000 μm × 1000 μm Raman map collected in PB solution contains 400 pixels as shown in Figure A**.11**C. Using the pH calibration curve in Figure A**.11**D, a pH map illustrates the pH value within the 35 fL volume derived from a single Raman spectrum. As shown in Figure A**.13**, such a single spectrum exhibits an excellent signal/noise ratio. Because the concentration of AuNPs used in this study is known (1.3×10^{11} mL^{-1}) each detection volume contained on average 2.3 NPs. This result demonstrates that each multimer exhibits extremely high SERS intensity. When all 400 pH values from the Raman map were plotted (inset to Figure A**.11**C), an extremely flat line was obtained. The small standard deviation (STD = 0.065 pH units) demonstrated the high pixel-to-pixel reproducibility of the SERS spectra. The pH sensitivity of our probe is defined as three fold of the STD,[39] i.e., about 0.2 pH units.

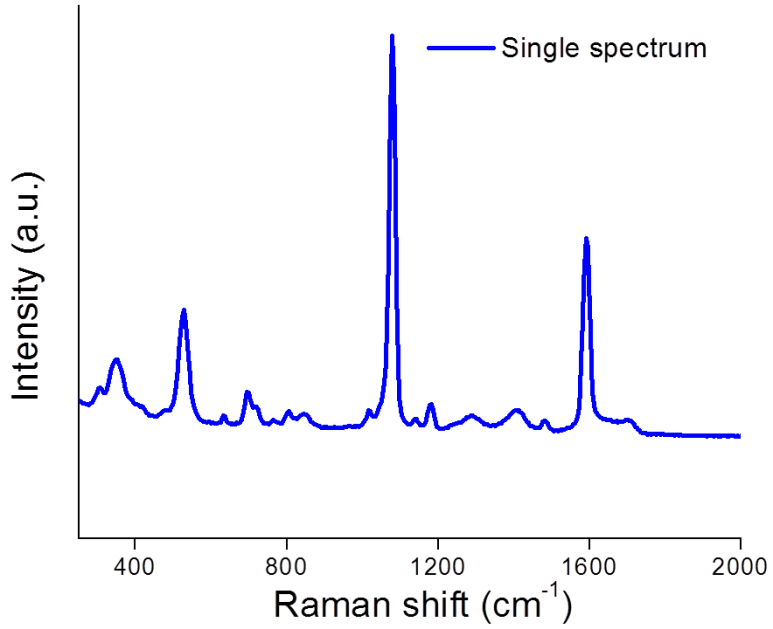

Figure A.13. Single Raman spectrum from a random selected pixel in the Raman map.

Probe stability is important for real world application of AuNP-based pH probes. The HS-PEG coating is expected to prevent AuNP aggregation and nonspecific chemical adsorption on the AuNP probes, thus improving both the spatial and temporal reproducibility of the probe response. To evaluate their stability, the probes were suspended in PB solution (0.01M) and the variation of their extinction spectra, size, and pH indicator values (I_{1410}/I_{1084} and I_{1710}/I_{1084}) were monitored for one hour. As shown in Figure A.**14**A-C, the extinction spectra, hydrodynamic diameter, and pH indicator values each remained constant during one hour thus indicating that the probes were highly stable in pH buffer. In addition, the stability of the probe was tested in two soft drinks (Fanta orange and club soda) and tap water. As shown in Figure A.**14**D, the pH values measured by our pH probe are consistent with those measured by a commercial pH meter. Impressively, the probes generated high quality and reproducible SERS spectra in each of these matrices, thus indicating that they were very stable in these complex matrices and that the other constituents present exhibited no interferences to probe response (Figure A.**15**).

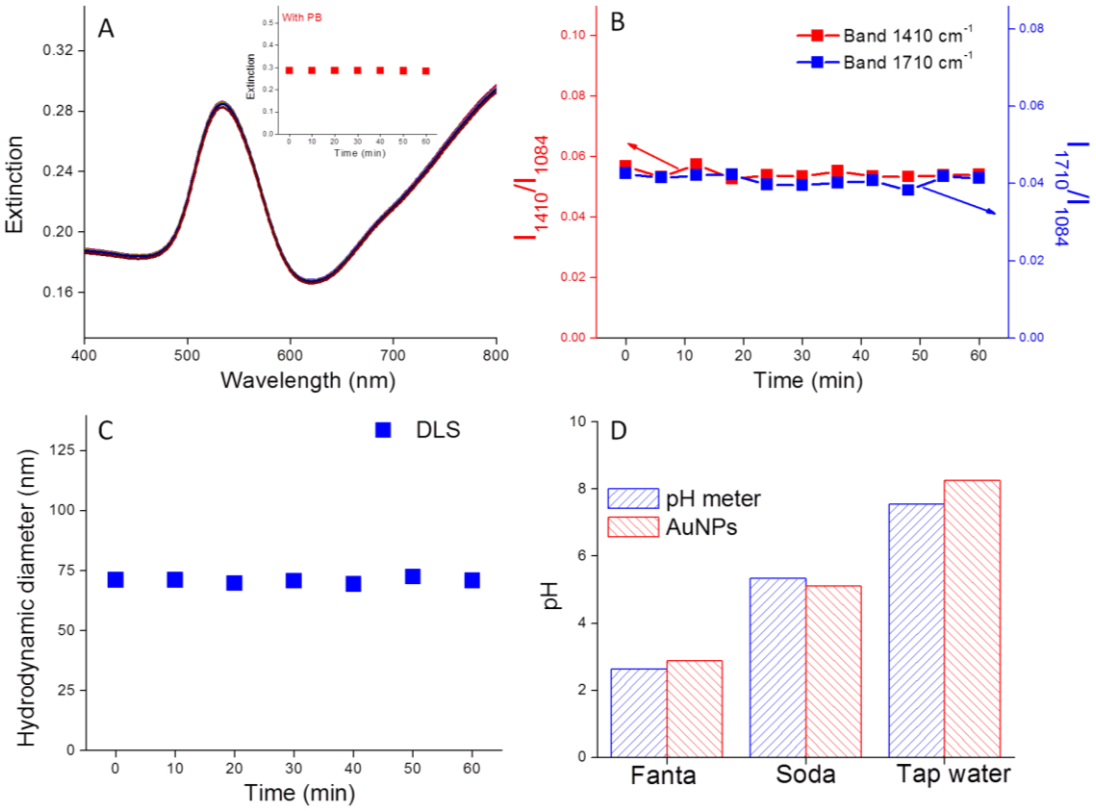

Figure A.14. A) Variations of the UV-VIS extinction spectra, B) pH indicator values, and C) hydrodynamic diameter of the pH probe in 0.01 M PB solution as a function of time; D) pH values of three real water samples measured by our pH probe and a commercial pH meter in our lab.

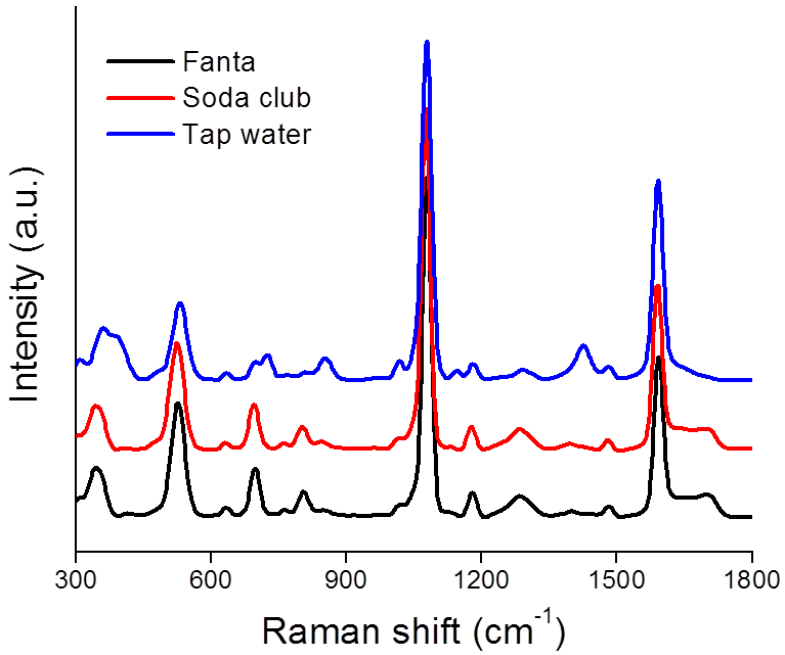

Figure A.15 SERS spectra of our pH probe suspended in Fanta, club soda, and tap water.

A.4.5 Intracellular pH Monitoring

As a proof-of-concept, we utilized our pH probes to detect the intracellular pH of the clinically relevant PC-3 human prostate cancer cell line. Nanoparticle uptake by PC-3 cells has been demonstrated numerous times in the literature[40] with endocytosis, a broad term encompassing many distinct pathways, considered the predominant method of AuNP uptake.[41, 42] Briefly, our pH probes were incubated with PC-3 cells for 24 hours, washed, and then imaged using Raman spectroscopy. As shown in Figure A**.16**A, the sizes and shapes of the cancer cells were heterogeneous, as expected for an adherent cell-line incubated for nearly two days.[43] The most prominent 4-MBA Raman band (1084 cm^{-1}) was used to identify the internalized nanoprobe locations and as shown in Figure A**.16**B, the probe position was co-located with that of the cancer cells. Intracellular localization of the nanoprobes was verified by depth scanning (Figure A**.17**). The nearly uniform SERS intensity within the cell, ~25 μm in depth, provides evidence that the probes were located inside the cell and not on the cell surface. These results demonstrate that the cancer cells can easily take up the pH sensitive PEG-4-MBA-AuNP probes described herein and can be readily imaged.

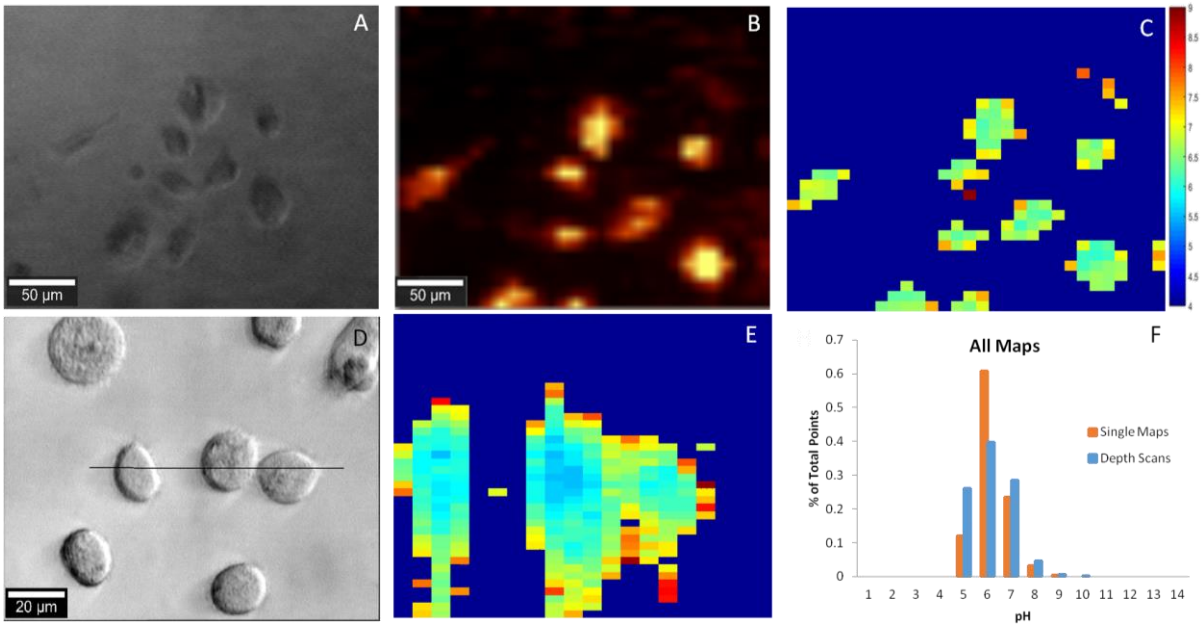

Figure A.16. A) Optical 10X image of PC3 cancer cells; B) SERS map of Figure A based on intensity of the 1084-[1] cm peak; C) pH map rendered in MATLAB of Fig A derived from the signal of Fig B. D) Optical 50X image of PC3 cancer cells with black line indicating position of YZ plane; E) In-depth pH map indicated by the black line in Fig D and F) Summary of pH distribution for single maps and depth scans.

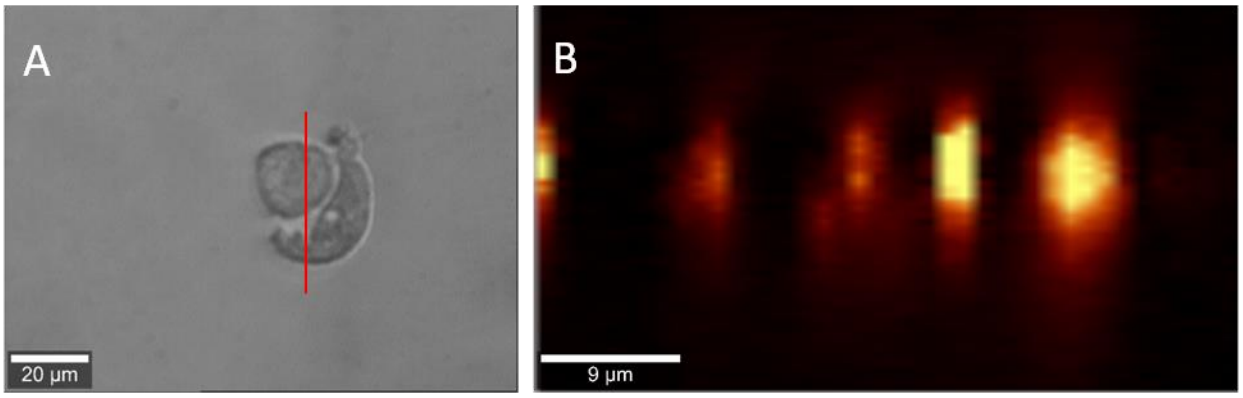

Figure A.17. A) Optical image of prostate cancer cell and B) Y-Z cross section Raman scan (marked by the red line) of the cancer cell.

To determine the intracellular pH of the cancer cells in rapid and automated fashion, the collected SERS maps were imported into Matlab and baseline corrected and analyzed using in-house scripts. At each point in every SERS map, the ratio between the pH insensitive peak (1084 cm^{-1}) and the pH sensitive peak (1410 cm^{-1}) was determined. Using a calibration curve established in cell culture media (Figure A**.18**), the pH was calculated at each point and then rendered into a XY map (Figure A**.16**C). The SERS spectrum of the internalized pH probes includes the 4-MBA Raman bands with good signal-to-noise ratio with no interference from either the cell or the culture medium, thus indicating the excellent stability and protection capability of the PEG layer. A typical SERS spectrum is shown in Figure A**.19**. Ultimately, 19 unique pH maps were collected. The intracellular pH range calculated over the whole sample set, Figure A**.16**F, agrees with the intracellular pH range reported in the literature of pH 4 to 9.[15, 17, 24, 25] Additionally, fourteen depth scans, YZ cross sections, were collected and demonstrate the three-dimensional spatial consistency of our probes (Figure A**.16**D&E). Again, for both single maps and depth scans across the dataset (Figure A**.16**F) more than 95% of the pH points fall between pH 5-7 and 99% of the points fall within the expected range for intracellular pH.

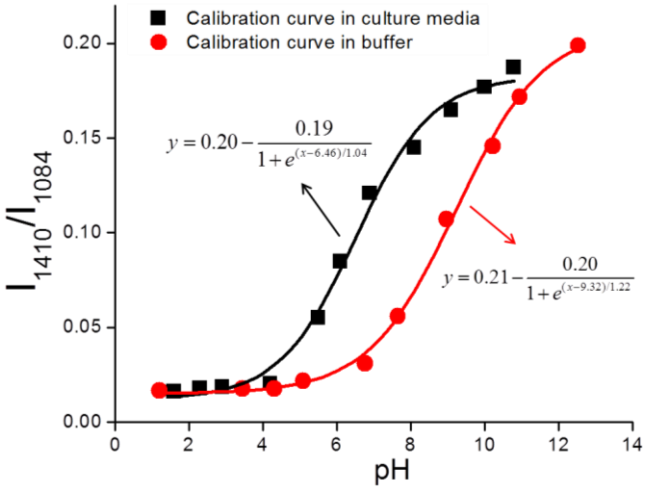

Figure A.18. pH calibration curves for pH probes in cell media (black squares) and in buffer (red circles).

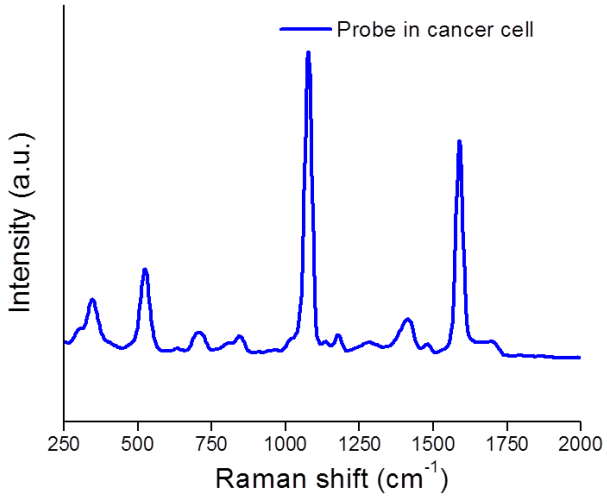

Figure A.19. SERS spectrum of the pH probe inside the cancer cell.

We found it necessary to develop a pH calibration curve in cell culture media. As shown in Figure A**.18**, there is a substantial difference in both the shape of the calibration curve and pH sensitive range in cell culture media relative to PB. We attribute this fact to the presence of proteins in the culture media as we observed a similar phenomenon in milk (data not shown). To our knowledge the observation that pH nanoprobes should be calibrated in culture media has not been addressed in a majority of the prior studies detailing their development. In Figure A**.20** we compare internal cell pH values measured using a calibration curve obtained in cell culture media relative to PB media alone. The lack of consideration of

this effect may be partially responsible for many of the extant reports of low pH zones in cells mapped using nanoprobes.

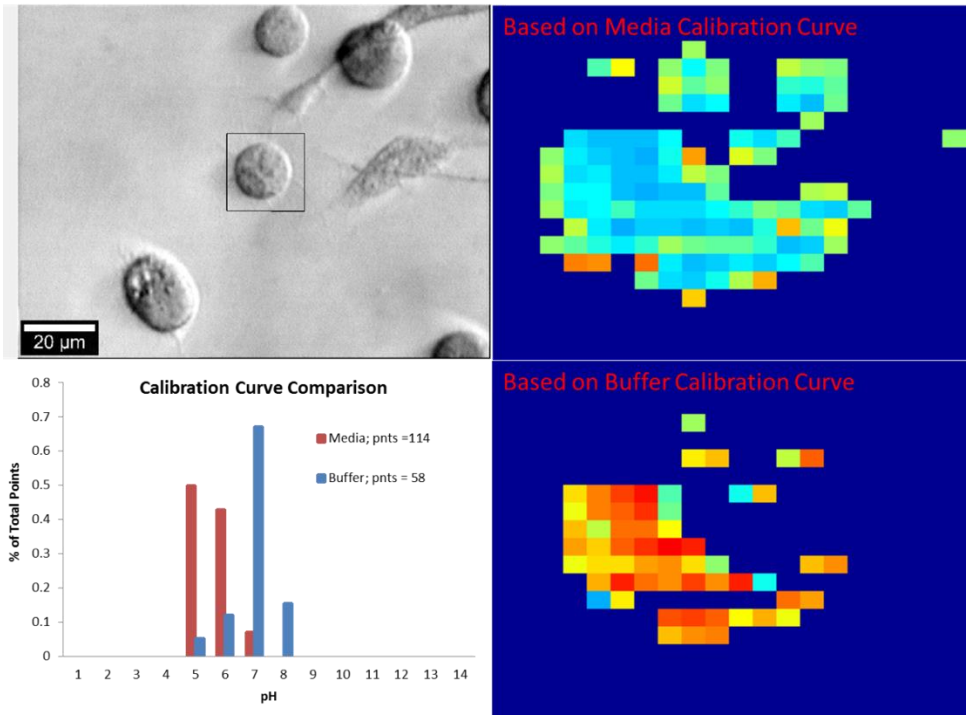

Figure A.20. Comparison of the pH calculated for a given cell with the two different calibration curves.

Compared to previously reported intracellular pH probes, our probe exhibits several advantages: 1) the Raman spectrum exhibits higher signal-to-noise ratio than those produced by uncontrolled aggregation (Figure A**.7**A, Figure A**.19**)[17, 24] due to our use of co-solvents to control the extent of aggregation. 2) The SERS spectra collected from probes internalized by PC3 cells only contain Raman bands for 4-MBA (Figure A**.19**) because the PEG protective layer prevents cellular components from reaching the surface. In contrast, many reported probes that do not have a protective layer exhibit potentially interferent Raman bands due to the biomolecules inside the cells.[16] 3) This paper demonstrates clear evidence that the probes are internalized by the PC3 cells by providing co-located optical and SERS images and is the first to present depth scans (Figure A**.16** & Figure A**.17**), while none of extent literature provides this information.[17, 22, 24, 26] As a comparison, in a recently published paper, 4-MBA-coated AuNPs without controlled aggregation and PEG protection were applied for detecting pH in EA.hy926 cells.[24] Due to lacking in SERS signal

optimization through controlled aggregation and stability through PEG protection, the probes exhibited much lower signal-to-noise ratio in cells compared to ours. SERS maps exhibited the tendency of the probes to locate in several limited areas inside the cells and reported several abnormally high pH values, which could be attributed to the severe aggregation of the unprotected probes and interferences from the biomolecules inside the cells or the culture media.

A.5 Conclusions

Herein we have described a novel, highly reproducible approach to control AuNP aggregation using water:ethanol co-solvent and 4-MBA mixtures. By using this approach, and by coating the resulting multimers with PEG to provide steric stability we were able to produce highly stable pH nanoprobes. Because of their colloidal stability these nanoprobes exhibit a broader pH sensitive range of 6-11 than existing pH nanoprobes described in the literature. An individual dimer within a 3.5 fL volume generates high SERS intensity, which is ideal for detecting pH changes within microenvironments. To provide proof of concept, we utilized the pH nanoprobes to detect the intracellular pH of PC-3 cancer cells. Using a Raman mapping approach and data processing we establish that intra-cellular pH is highly consistent across multiple cells and we have produced the most robust database of intracellular pH obtained by SERS to date. Because the protective PEG layer can be replaced with bifunctional PEG (i.e., both thiol and carboxy terminated) our nanoprobes can be further functionalized to provide multiplex sensing capacity. In our ongoing studies we seek to utilize this capacity to measure not only pH, but also to detect and quantify cells.

A.6 Reference

1. Wei, H.; Willner, M. R.; Marr, L. C.; Vikesland, P. J., Highly stable SERS pH nanoprobes produced by co-solvent controlled AuNP aggregation. *Analyst* **2016,** *141*, (17), 5159-5169.
2. Wei, H.; Vikesland, P. J., pH-Triggered Molecular Alignment for Reproducible SERS Detection via an AuNP/Nanocellulose Platform. *Sci. Rep.* **2015,** *5*, 18131.
3. Halvorson, R. A.; Vikesland, P. J., Surface-Enhanced Raman Spectroscopy (SERS) for Environmental Analyses. *Environ. Sci. Tech.* **2010,** *44*, (20), 7749-7755.
4. Wei, H.; Abtahi, S. M. H.; Vikesland, P. J., Plasmonic Colorimetric and SERS Sensors for Environmental Analysis. *Environ. Sci. Nano* **2015,** *2*, (2), 120-135.
5. Wei, H.; Rodriguez, K.; Renneckar, S.; Leng, W.; Vikesland, P. J., Preparation and evaluation of nanocellulose–gold nanoparticle nanocomposites for SERS applications. *Analyst* **2015,** *140*, (16), 5640-5649.
6. Rule, K. L.; Vikesland, P. J., Surface-Enhanced Resonance Raman Spectroscopy for the Rapid Detection of Cryptosporidium Parvum and Giardia Lamblia. *Environ. Sci. Tech.* **2009,** *43*, (4), 1147-1152.
7. Braun, G.; Pavel, I.; Morrill, A. R.; Seferos, D. S.; Bazan, G. C.; Reich, N. O.; Moskovits, M., Chemically Patterned Microspheres for Controlled Nanoparticle Assembly in the Construction of SERS Hot Spots. *J Am Chem Soc* **2007,** *129*, (25), 7760-7761.
8. Kleinman, S. L.; Frontiera, R. R.; Henry, A. I.; Dieringer, J. A.; Van Duyne, R. P., Creating, Characterizing, and Controlling Chemistry with SERS Hot Spots. *Phys Chem Chem Phys* **2013,** *15*, (1), 21-36.
9. Lawson, L. S.; Chan, J. W.; Huser, T., A Highly Sensitive Nanoscale pH-Sensor Using Au Nanoparticles Linked by a Multifunctional Raman-Active Reporter Molecule. *Nanoscale* **2014,** *6*, (14), 7971-7980.
10. Braun, G. B.; Lee, S. J.; Laurence, T.; Fera, N.; Fabris, L.; Bazan, G. C.; Moskovits, M.; Reich, N. O., Generalized Approach to SERS-Active Nanomaterials via Controlled Nanoparticle Linking, Polymer Encapsulation, and Small-Molecule Infusion. *J. Phys. Chem. C* **2009,** *113*, (31), 13622-13629.
11. Romo-Herrera, J. M.; Alvarez-Puebla, R. A.; Liz-Marzán, L. M., Controlled Assembly of Plasmonic Colloidal Nanoparticle Clusters. *Nanoscale* **2011,** *3*, (4), 1304-1315.
12. Leng, W.; Vikesland, P. J., MGITC Facilitated Formation of AuNP Multimers. *Langmuir* **2014,** *30*, (28), 8342-8349.
13. Lim, D.-K.; Jeon, K.-S.; Hwang, J.-H.; Kim, H.; Kwon, S.; Suh, Y. D.; Nam, J.-M., Highly Uniform and Reproducible Surface-Enhanced Raman Scattering from DNA-Tailorable Nanoparticles with 1-nm Interior Gap. *Nat. Nanotechnol.* **2011,** *6*, (7), 452-460.
14. Taylor, R. W.; Lee, T. C.; Scherman, O. A.; Esteban, R.; Aizpurua, J.; Huang, F. M.; Baumberg, J. J.; Mahajan, S., Precise Subnanometer Plasmonic Junctions for SERS within Gold Nanoparticle Assemblies using Cucurbit [n] uril "Glue". *ACS Nano* **2011,** *5*, (5), 3878-3887.
15. Pallaoro, A.; Braun, G. B.; Reich, N.; Moskovits, M., Mapping Local pH in Live Cells Using Encapsulated Fluorescent SERS Nanotags. *Small* **2010,** *6*, (5), 618-622.
16. Wang, Z.; Bonoiu, A.; Samoc, M.; Cui, Y.; Prasad, P. N., Biological pH Sensing Based on Surface Enhanced Raman Scattering through a 2-Aminothiophenol-Silver Probe. *Biosensors and Bioelectronics* **2008,** *23*, (6), 886-891.
17. Talley, C. E.; Jusinski, L.; Hollars, C. W.; Lane, S. M.; Huser, T., Intracellular pH Sensors Based on Surface-Enhanced Raman Scattering. *Anal. Chem.* **2004,** *76*, (23), 7064-7068.
18. Bishnoi, S. W.; Rozell, C. J.; Levin, C. S.; Gheith, M. K.; Johnson, B. R.; Johnson, D. H.; Halas, N. J., All-Optical Nanoscale pH Meter. *Nano letters* **2006,** *6*, (8), 1687-1692.

19. Piotrowski, P.; Wrzosek, B.; Królikowska, A.; Bukowska, J., A SERS-Based pH Sensor Utilizing 3-Amino-5-Mercapto-1, 2, 4-Triazole Functionalized Ag Nanoparticles. *Analyst* **2014,** *139*, (5), 1101-1111.
20. Zheng, X. S.; Hu, P.; Cui, Y.; Zong, C.; Feng, J. M.; Wang, X.; Ren, B., BSA-Coated Nanoparticles for Improved SERS-Based Intracellular pH Sensing. *Anal. Chem.* **2014,** *86*, (24), 12250-12257.
21. Zong, S.; Wang, Z.; Yang, J.; Cui, Y., Intracellular pH Sensing Using p-Aminothiophenol Functionalized Gold Nanorods with Low Cytotoxicity. *Analytical chemistry* **2011,** *83*, (11), 4178-4183.
22. Liu, Y.; Yuan, H.; Fales, A. M.; Vo-Dinh, T., pH-Sensing Nanostar Probe Using Surface-Enhanced Raman Scattering (SERS): Theoretical and Experimental Studies. *Journal of Raman Spectroscopy* **2013,** *44*, (7), 980-986.
23. Gühlke, M.; Heiner, Z.; Kneipp, J., Combined Near-Infrared Excited SEHRS and SERS Spectra of pH Sensors Using Silver Nanostructures. *Physical Chemistry Chemical Physics* **2015,** *17*, (39), 26093-26100.
24. Jaworska, A.; Jamieson, L. E.; Malek, K.; Campbell, C. J.; Choo, J.; Chlopicki, S.; Baranska, M., SERS-Based Monitoring of the Intracellular pH in Endothelial Cells: the Influence of the Extracellular Environment and Tumour Necrosis Factor-α. *Analyst* **2015,** *140*, (7), 2321-2329.
25. Jamieson, L.; Jaworska, A.; Jiang, J.; Baranska, M.; Harrison, D.; Campbell, C., Simultaneous Intracellular Redox Potential and pH Measurements in Live Cells Using SERS Nanosensors. *Analyst* **2015,** *140*, (7), 2330-2335.
26. Wang, F.; Widejko, R. G.; Yang, Z.; Nguyen, K. T.; Chen, H.; Fernando, L. P.; Christensen, K. A.; Anker, J. N., Surface-Enhanced Raman Scattering Detection of pH with Silica-Encapsulated 4-Mercaptobenzoic Acid-Functionalized Silver Nanoparticles. *Analytical chemistry* **2012,** *84*, (18), 8013-8019.
27. Liao, J.; Zhang, Y.; Yu, W.; Xu, L.; Ge, C.; Liu, J.; Gu, N., Linear Aggregation of Gold Nanoparticles in Ethanol. *Colloids Surf. A Physicochem. Eng. Asp.* **2003,** *223*, (1), 177-183.
28. Freus, G., Controlled nucleation for the regulation of the particle size in monodisperse gold solutions. *Nature (Phys Sci)* **1973,** *241*, 20-22.
29. Ji, X.; Song, X.; Li, J.; Bai, Y.; Yang, W.; Peng, X., Size control of gold nanocrystals in citrate reduction: the third role of citrate. *Journal of the American Chemical Society* **2007,** *129*, (45), 13939-13948.
30. Brown, K. R.; Walter, D. G.; Natan, M. J., Seeding of colloidal Au nanoparticle solutions. 2. Improved control of particle size and shape. *Chemistry of Materials* **2000,** *12*, (2), 306-313.
31. Darby, B. L.; Le Ru, E. C., Competition between Molecular Adsorption and Diffusion: Dramatic Consequences for SERS in Colloidal Solutions. *Journal of the American Chemical Society* **2014,** *136*, (31), 10965-10973.
32. Eilers, P. H., and Hans FM Boelens *Baseline Correction with Asymmetric Least Squares Smoothing*; 2005.
33. Leng, W.; Pati, P.; Vikesland, P. J., Room Temperature Seed Mediated Growth of Gold Nanoparticles: Mechanistic Investigations and Life Cycle Assesment. *Environ. Sci. Nano* **2015,** *2*, (5), 440-453.
34. Ge, Z.; Wu, L.; Zhang, F.; He, Z., Energy extraction from a large-scale microbial fuel cell system treating municipal wastewater. *Journal of Power Sources* **2015,** *297*, 260-264.
35. Qian, X.; Peng, X.-H.; Ansari, D. O.; Yin-Goen, Q.; Chen, G. Z.; Shin, D. M.; Yang, L.; Young, A. N.; Wang, M. D.; Nie, S., In Vivo Tumor Targeting and Spectroscopic Detection with Surface-Enhanced Raman Nanoparticle Tags. *Nature biotechnology* **2008,** *26*, (1), 83.
36. Jokerst, J. V.; Lobovkina, T.; Zare, R. N.; Gambhir, S. S., Nanoparticle PEGylation for Imaging and Therapy. *Nanomedicine* **2011,** *6*, (4), 715-728.
37. Leopold, M. C.; Black, J. A.; Bowden, E. F., Influence of Gold Topography on Carboxylic Acid Terminated Self-Assembled Monolayers. *Langmuir* **2002,** *18*, (4), 978-980.

38. Ma, C.; Harris, J. M., Surface-Enhanced Raman Spectroscopy Investigation of the Potential-Dependent Acid− Base Chemistry of Silver-Immobilized 2-Mercaptobenzoic Acid. *Langmuir* **2011,** *27*, (7), 3527-3533.
39. Rezaee, M.; Assadi, Y.; Hosseini, M.-R. M.; Aghaee, E.; Ahmadi, F.; Berijani, S., Determination of organic compounds in water using dispersive liquid–liquid microextraction. *Journal of Chromatography A* **2006,** *1116*, (1), 1-9.
40. Gregas, M. K.; Scaffidi, J. P.; Lauly, B.; Vo-Dinh, T., Surface-Enhanced Raman Scattering Detection and Tracking of Nanoprobes: Enhanced Uptake and Nuclear Targeting in Single Cells. *Appl. Spectrosc.* **2010,** *64*, (8), 858-866.
41. Chithrani, B. D.; Ghazani, A. A.; Chan, W. C. W., Determining the Size and Shape Dependence of Gold Nanoparticle Uptake into Mammalian Cells. *Nano Lett.* **2006,** *6*, (4), 662-668.
42. Chou, L. Y. T.; Ming, K.; Chan, W. C. W., Strategies for the Intracellular Delivery of Nanoparticles. *Chem. Soc. Rev.* **2011,** *40*, (1), 233-245.
43. ATCC, PC-3 (ATCC® CRL-1435™). In.

Appendix BAerosol Droplets Exhibit a Stable pH Gradient

(This chapter is under review in ***Proceedings of National Academic of Sciences***.)

B.1 Abstract

Suspended aqueous aerosol droplets (<50 μm) are micro-reactors for many important atmospheric reactions. In droplets, and other aquatic environments, pH is arguably the key parameter dictating chemistry and biology. The dynamic nature of the droplet air/water interface has the potential to significantly alter droplet pH relative to bulk water values. Historically, it has been challenging to measure the pH of individual droplets due to their inaccessibility to conventional pH probes. In this study, we scanned droplets containing 4-mercaptobenzoic acid (4-MBA) functionalized gold nanoparticle (AuNP) pH nanoprobes by 2D and 3D laser confocal Raman microscopy. Using surface-enhanced Raman scattering (SERS), we acquired the pH distribution inside individual aerosol droplets for the first time and found that the pH in the core of a droplet is higher than that of bulk water by up to 3.6 pH units. This finding suggests the accumulation of protons at the air/water interface and is thus consistent with recent thermodynamic model results. The existence of this shift in pH was corroborated by the observation that a catalytic reaction that only occurs under basic conditions (i.e., dimercaptoazobenzene (DMAB) formation from 4-aminothiophenol (4-ATP)) occurs within the high pH core of a droplet, but not in bulk solution. Our nanoparticle-derived pH probe strategy enabled quantification of the pH gradient through the cross-section of an aerosol droplet and has important implications for acid-base catalyzed atmospheric chemistry.

B.2 Introduction

At high relative humidity (RH), aerosols containing liquid water are ubiquitous and have a profound influence on local, regional, and global atmospheric processes.[1-7] For example, aerosol droplets in clouds influence the global radiation budget and the hydrological cycle, which have uncertain feedbacks linked to factors driving climate change.[8, 9] At both local and global scale, sea spray and anthropogenic aerosols

impact coastal and inland communities as well as climate through their capacity to absorb and scatter solar radiation and their role in cloud formation,[10, 11] while anthropogenic aerosols contribute to air quality problems in urban areas across the world.[12]

To quantify the impacts of these aerosols, we need to characterize their physical and chemical properties to understand how they influence *in situ* aerosol chemical reactions. In particular, the formation of organosulfates, acetals, esters/amides and other compounds affect secondary organic aerosol (SOA) production.[13-15] pH is arguably the key parameter defining droplet chemistry because of its central role dictating chemical speciation and reactivity.[16-18] pH is known to affect reactive uptake of atmospheric gases, phase separation, and indirectly surface tension.[19-22] Nonetheless, it is analytically challenging to measure the pH of individual aerosols due to the current dearth of tools that can detect pH within the confined, micron-scale droplet environment.[23]

It is well known that water at the air-water interface exhibits different structure and hydrogen bond dynamics relative to bulk water and that these differences affect the pH of the near-surface region.[24] Unfortunately, it is both experimentally and theoretically challenging to probe the air/water interface, and even more so the acidity of that interface.[25] Electrophoretic mobility measurements of oil droplets and air bubbles in water indicate that this interface is negatively charged. The simplest explanation for this observation is the accumulation of hydroxide (OH^-) at the interface and the electrostatic repulsion of hydronium (H_3O^+). This conceptual model, however, is inconsistent with surface sensitive experimental techniques such as second harmonic generation (SHG) and sum-frequency generation (SFG) that indicate that the interface is H_3O^+ enriched.[26] Molecular dynamics[27] and continuum solvent model[26] simulations further support the argument that H_3O^+ has greater affinity for the air/water interface than does OH^- and that the water surface of aerosol droplet is expected to be acidic.[27, 28]

Currently, aerosol pH values are typically calculated using thermodynamic models, such as E-AIM and ISORROPIA-II,[17, 18, 29, 30] that assume equilibrium between dissolved inorganic ions in the aqueous aerosol environment. However, these equilibrium models require measurement of the concentrations of multiple

inorganic ions and the estimation of aerosol water content.[31] They also neglect the impacts of organic ions as well as particle phase and morphology. Furthermore, because aqueous aerosol particles are inherently heterogeneous, both internally and externally, there is a significant need to obtain individual aerosol particle measurements in place of ensemble average or bulk measurements.[23]

A number of spectroscopic and microscopic techniques such as electron microscopy, X-ray microscopy, fluorescence microscopy, single-particle aerosol mass spectroscopy, and Raman microscopy have the potential for single particle characterization.[23] Raman spectroscopy, in particular, provides the capacity to differentiate the vibrational states of acids and their conjugate bases under ambient conditions that are not accessible by other techniques. Recently, Rindelaub et al. used Raman spectroscopy to determine the pH of aerosol particles by tracking the ratio of the Raman bands of SO_4^{2-} and HSO_4^-.[32] Unfortunately, this approach was only useful in the highly acidic pH range near the HSO_4^-/SO_4^{2-} pK_a of 2. Recently, surface-enhanced Raman spectroscopy (SERS) has been suggested as a means to sensitively probe atmospheric aerosols.[33, 34] SERS is an *in situ* method that can be used to probe water matrices, it exhibits extreme sensitivity,[35-37] and it provides a highly stable signal.[38]

Recently, we and others[39-42] have shown that SERS provides the capacity to measure pH in confined aqueous environments. Using a plasmonic nanoparticle that has been surface functionalized with a pH sensitive amine or carboxylic acid it is possible to collect SERS spectra that change as a function of the local pH. Solution pH is then determined based upon relative peak heights or changes in the band locations of specific vibrational modes. Herein, we employed nano-sized pH probes to characterize the pH of individual phosphate-buffered aerosol droplets and found that they exhibited a stable pH gradient across a droplet that often exceeded three pH units. Phosphorous is an important, yet underappreciated, component of many aerosols.[43-45] It is also useful as a buffer as, in contrast to ammonium and sulfate, it exhibits minimal gas-particle partitioning. By combining the spatial resolution of a confocal Raman microscope with the inherent sensitivity of these probes, we were able to obtain the first two-dimensional (2D) and three-dimensional (3D) characterization of the pH distribution of micron-sized aerosol droplets under *in*

situ conditons. The information acquired by this approach provides improved quantification of the pH of aerosol droplets.

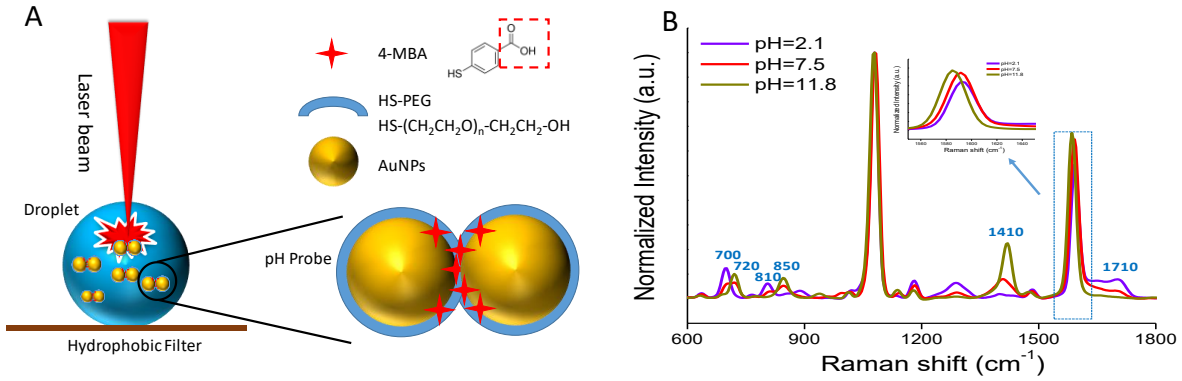

Figure B.1. Principle for the pH detection of aerosol droplets using pH SERS nanoprobes. A) Schematics illustrating SERS probing of aerosol droplets collected on a superhydrophobic PVDF filter and of SERS pH nanoprobes; B) SERS spectra of pH nanoprobes in bulk phosphate buffer (PB) solutions (0.6 M) that were adjusted to different pH values.

B.3 Results

B.3.1 Principle of Droplet pH Detection by SERS

Our overall experimental design is illustrated in Figure B**.1**. Aqueous microdroplets (17.4±4.6 µm) were generated from a 0.6 M phosphate buffer (PB) solution containing pH nanoprobes (2×10^{10} particles/mL) using a commercial atomizer (TSI 3076). Produced droplets were collected on a superhydrophobic surface prepared by drop-coating polydimethylsiloxane-treated silica nanoparticles onto a 0.22 µm polyvinylidene difluoride (PVDF) filter (Figure B**.1**A). The filter with the collected droplets was then placed in a humidity controlled flow cell. Unless otherwise indicated, all of the experiments were conducted at a RH of 97±0.5%.

As shown in Figure B**.1**A, the pH nanoprobes consist of an AuNP optical antenna, a thiolated polyethylene glycol (PEG) stabilizing layer, and the 4-mercaptobenzoic acid (4-MBA) pH indicator.[42] 4-MBA is bifunctional, with a thiol group to covalently bind to the AuNP surface and a carboxylate group to detect changes in pH. SERS spectra collected from nanoprobes in bulk solutions of 0.6 M PB with different initial pH values are shown in Figure B**.1**B. There are six characteristic Raman bands that change in intensity as the solution pH increases: 1) bands at 720 (out-of-plane ring hydrogen wagging), 850 (COO^- bending), and 1410 cm^{-1} (COO^- stretching) increase; and 2) bands at 700 (OCO bending), 810 (C-COOH

stretching), and 1710 cm^{-1} (CO stretching) decrease.[46] Simultaneously, the band at 1590 cm^{-1} (benzene ring breathing and axial deformation) shifts to a lower wavenumber.[47] The other Raman bands in the spectrum are pH-insensitive, with the band at 1080 cm^{-1} (benzene ring breathing and axial deformation) the strongest. The ratios of the Raman bands at 1710 cm^{-1} to 1080 cm^{-1} (I_{1710}/I_{1080}) and 1410 cm^{-1} to 1080 cm^{-1} (I_{1410}/I_{1080}) were used to construct pH calibration curves and are well described by the Boltzmann equation (Figure B.**2**).

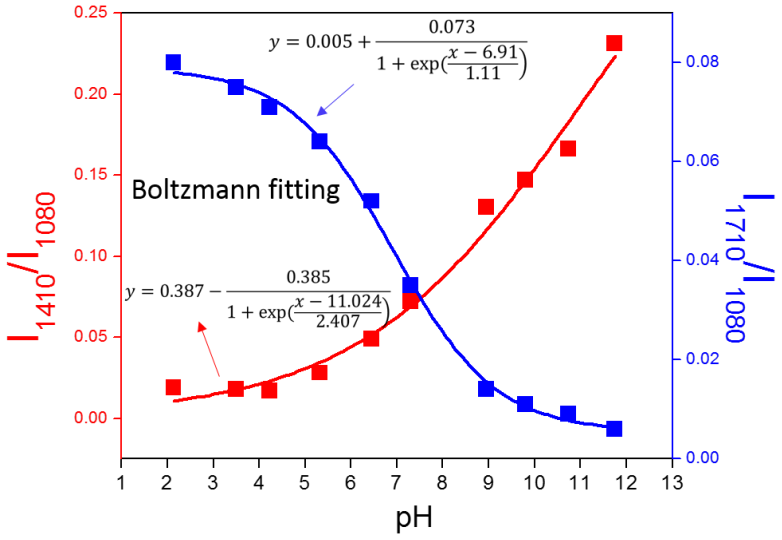

Figure B.2. pH calibration curves constructed by fitting the variation of ratios I_{1410}/I_{1080} and I_{1710}/I_{1080} as a function of solution pH in Boltzmann equation.

B.3.2 Collection and Raman Scan of Microdroplets

Following aerosolization, micrometer-sized aqueous droplets were observed across the filter, indicating successful droplet generation and collection (Figure B.**3**A). As shown in Figure B.**3**B, the droplets are highly spherical owing to the high contact angle of 157.3º imparted by the superhydrophobic substrate. Using ImageJ, we calculated an average droplet size of 19.5±6.2 μm for 155 droplets collected on five separately prepared superhydrophobic filters (Figure B.**3**C). Control experiments indicate that the presence of the pH nanoprobes did not significantly alter the droplet size distribution (Figure B.**3**C). We note, however, that droplets <10 μm were not enumerated due to their poor contrast against the substrate.

A key consideration for *in situ* droplet scanning is the stability of a droplet over the course of a measurement. To evaluate droplet stability, we monitored droplet diameter as a function of time and as

shown in Figure B.**4** observed that it remained stable over a 44 min period due to our control of RH in the flow cell. In contrast, droplets scanned under supersaturated RH conditions grew in size over the course of an hour (Figure B.**5**). The droplet diameter remained unchanged after an entire Raman scan using a 50× objective (Figure B.**6**), thus indicating a droplet is stable enough for laser confocal Raman interrogation.

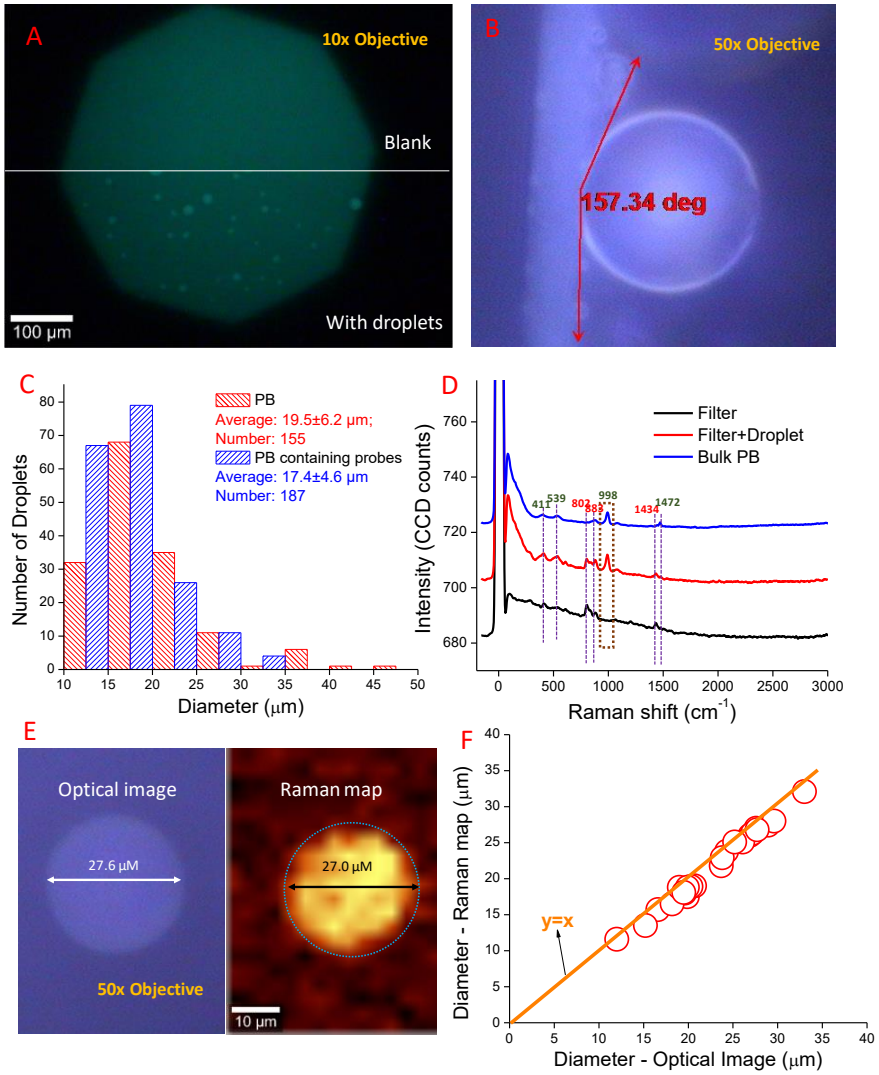

Figure B.3. Generation, collection, and Raman scan of the aerosol droplets. A) Optical images of a blank superhydrophobic PVDF filter (top) and aerosol droplets collected on a superhydrophobic PVDF filter (bottom); B) The optical image of the side view of a droplet that was used to measure contact angle; C) Size distribution of aerosol droplets generated from 1 M PB solution and 0.6 M PB solution + pH nanoprobes; D) Raman spectra of 1M bulk PB solution, superhydrophobic PVDF filter, and 1M PB aerosol droplet on a superhydrophobic PVDF filter; E) Optical image and Raman map of a droplet generated from 1 M PB solution constructed by tracking the Raman band at 998 cm^{-1}; F) Relationship between droplet diameters measured using Raman maps and optical images.

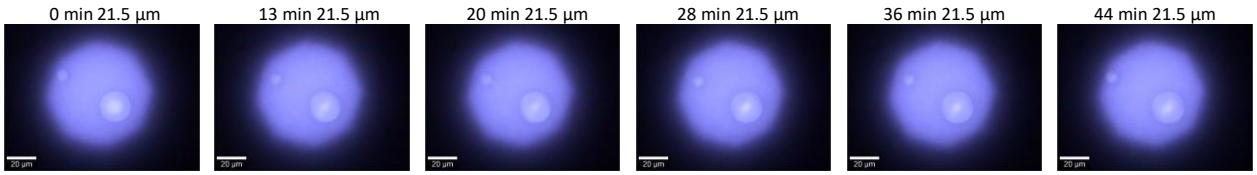

Figure B.4. Optical images of one microdroplet taken at different time under well controlled RH of 97%.

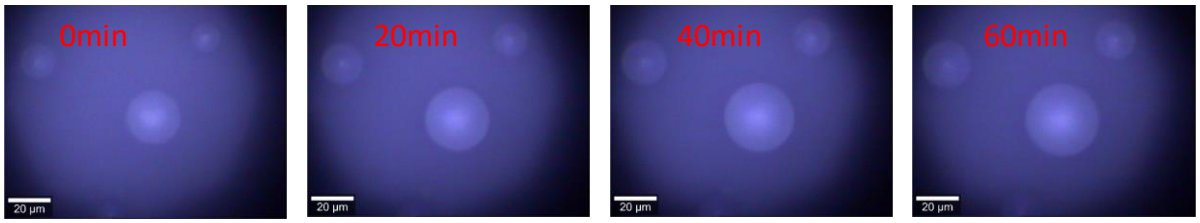

Figure B.5. Optical images of one microdroplet taken at different time under oversaturated RH caused by the wet paper in the cell.

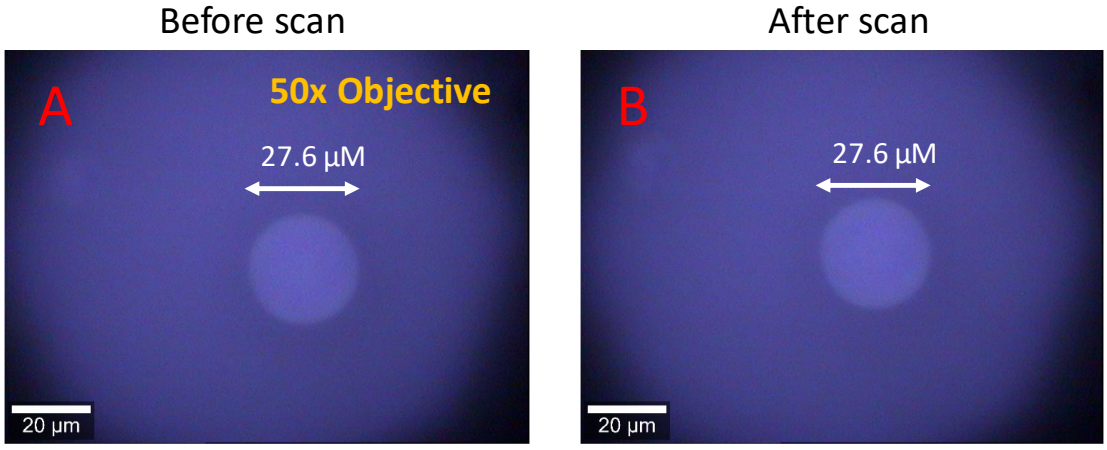

Figure B.6. Optical images of one aerosol droplet under 50x objective (A) before and (B) after laser interrogation.

Following the successful generation and collection of droplets, they were individually scanned by confocal Raman microscopy using collection areas slightly larger than their respective diameters. As shown in Figure B.**3**D, the normal Raman spectrum of a droplet generated from a PB solution contains Raman bands for both PB (411, 539, 998, and 1472 cm^{-1}) and the PVDF filter (802, 883, and 1434 cm^{-1}). A Raman map made by tracking the intense band at 998 cm^{-1} ($\nu_1(PO_4^{3-})$) is shown in Figure B.**3**E.[48] The area defined by the Raman signal is illustrated by the circle drawn around it. This circle is comparable to the droplet diameter determined from the optical image (27.0 vs 27.6 µm, Figure B.**3**E). As shown in Figure B.**3**F,

there is a linear relationship between the droplet diameter determined optically and that obtained by Raman imaging.

B.3.3 The Core pH of a Droplet is Higher Than Bulk pH

In the presence of the pH nanoprobes, the Raman signals arising from either the PB or the PVDF substrates are weak and are overwhelmed by the 4-MBA SERS signal (Figure B**.7**). SERS maps of droplets can however be obtained by tracking the benzene ring breathing and axial deformation mode of 4-MBA at 1080 cm^{-1}.[49] As shown in Figure B**.8**A, the SERS maps of five different droplets exhibited variable patterns indicating the pH nanoprobes are not as uniformly distributed within each droplet as the phosphate molecules are (Figure B**.3**E). Such droplet-to-droplet variation highlights the necessity of measuring pH inside individual droplets.

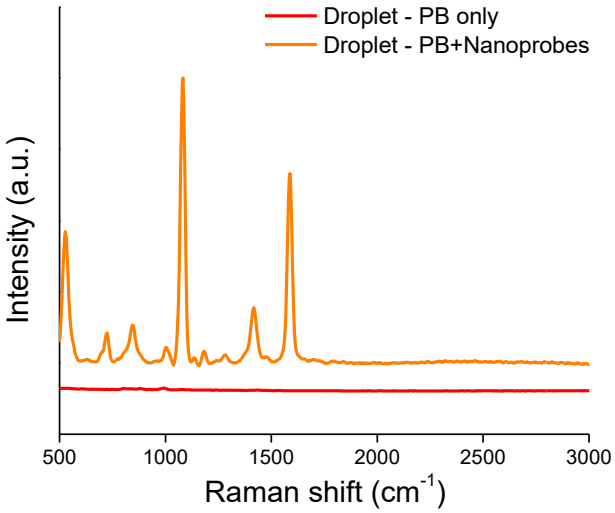

Figure B.7. Raman spectra collected from aerosol droplets containing only 1 M PB and 0.6 M PB + nanoprobes.

We note that the droplet diameter determined from the SERS signal is consistently smaller than that from the comparable optical images (Figure B**.8**B; Figure B**.9**). These results suggest that the PEG-coated AuNPs preferentially partition towards the droplet centroid and away from the comparatively hydrophobic air/water interface.[50, 51] It was recently suggested that polyvinylpyrrolidone (PVP) coated AgNPs preferentially accumulate at the air/water interface.[52] We tested this hypothesis by synthesizing PVP-coated pH nanoprobes, but determined that these nanoprobes still preferentially partition towards the droplet

centroid (Figure B**.10**). We are currently working to develop nanoparticle based pH probes that target the air-water interface.

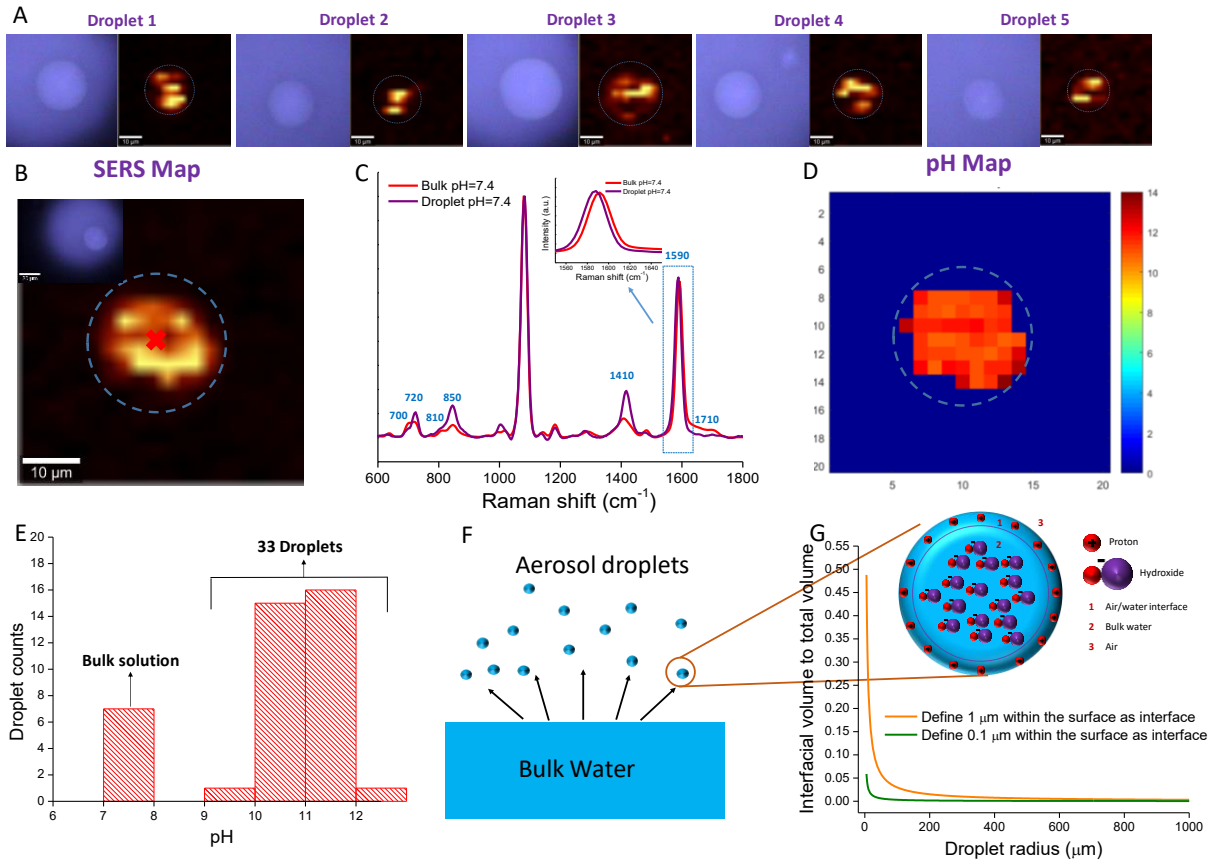

Figure B.8. 2D characterization of the pH inside aerosol droplets. A) Optical images and Raman maps of droplets generated from 0.6 M PB + pH nanoprobes by tracking the 4-MBA Raman band at 1080 cm^{-1}; B) One Raman map of a droplet by tracking the 4-MBA Raman band at 1080 cm^{-1}; the dashed circle is the outline of the droplet; Inset is the optical image of the droplet; The diameter determined by SERS signal is smaller than that determined by optical image (18.8 vs 23.5 μm); C) SERS spectra collected from bulk solution with pH of 7.4 and droplet generated from that bulk solution; D) pH map of the droplet shown in Fig. 3B; E) pH at the centroid of 33 different droplets generated from bulk solutions with pH of 7.4; F) Schematic of the aerosol droplets generated from a bulk solution and the accumulation of protons at air/water interface in aerosol droplets; G) Variation of interfacial volume to total volume of droplets as a function of droplet radius.

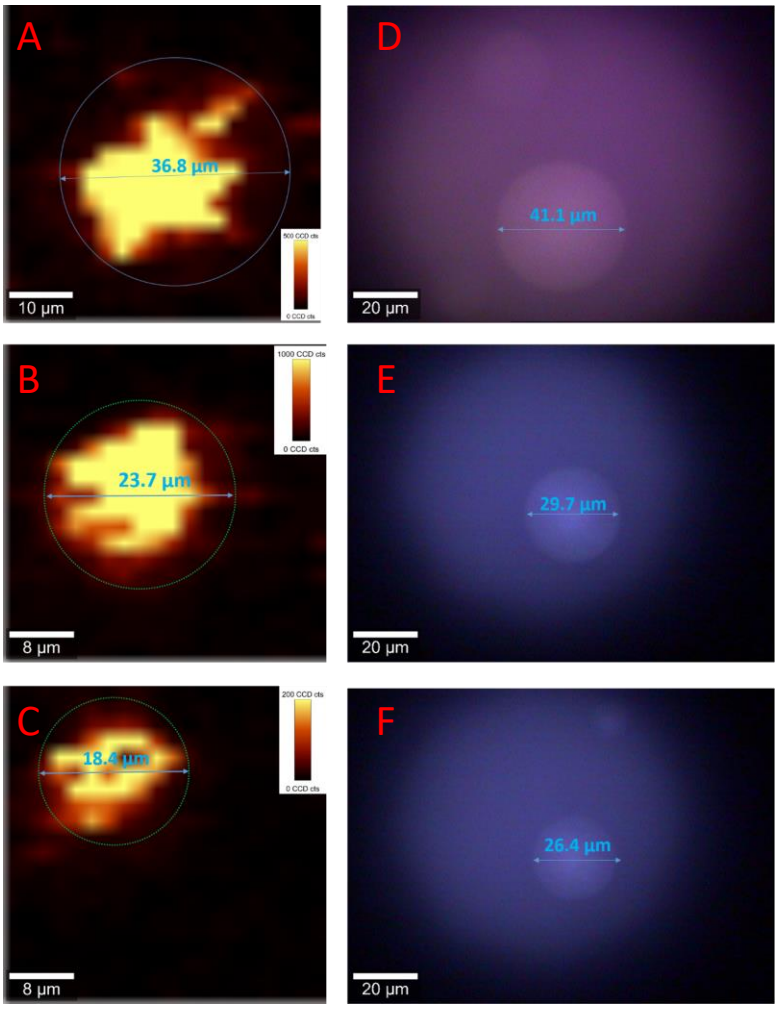

Figure B.9. A-C) SERS maps tracking 4-MBA band at 1080 cm^{-1} of three droplets; D-F) Optical images of the three droplets.

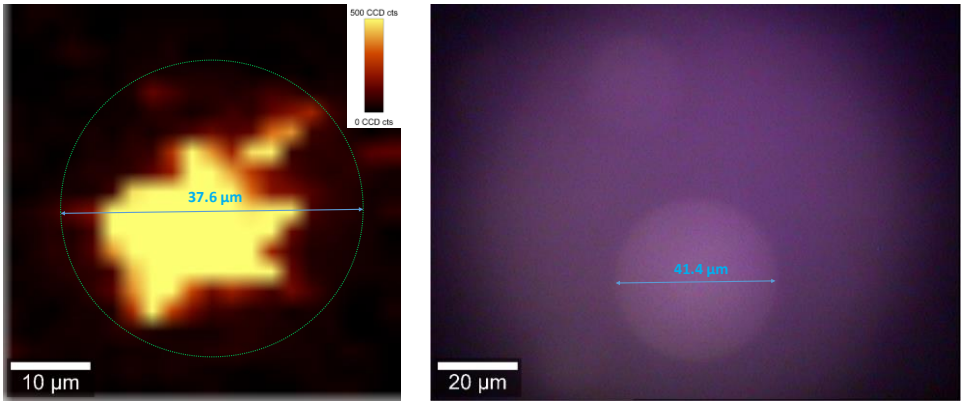

Figure B.10. SERS map and optical image of droplet containing PVP-coated pH nanoprobes.

A representative SERS spectrum collected from the center of a droplet is shown in Figure B.**8**C along with the SERS spectrum for nanoprobes dispersed in bulk PB. As shown, all seven pH indicators suggest that the pH at the droplet centroid was much higher than the bulk solution (pH=7.4) from which the droplet

was generated (i.e., the bands at 720, 850, and 1410 cm^{-1} increase in magnitude while the bands at 700, 810, and 1710 cm^{-1} decrease in magnitude and the band at 1590 cm^{-1} shifts to a lower wavenumber). The measured SERS signals were converted into pH values using the calibration curve shown in Figure B**.2** to produce 2D pH maps that reflect the measured pH distribution within the planar region bisecting the droplet (Figure B**.8**D). Interestingly all of the pixels exhibit pH values higher than the bulk solution pH of 7.4. This same result was found in similar pH maps collected for 33 individual droplets (Figure B**.11**). The measured average pH at the droplet centroid of 33 separate droplets was 11.0±0.49 (Figure B**.8**E). This value is 3.6 pH units higher than the initial bulk pH. Control experiments in which the probe concentration was varied by 0.5-2× (our experimentally accessible range) indicate that the measured pH was not affected by the nanoprobe concentration (Figure B**.12**). In addition, experiments using a range of initial pH values (2.1-10.7) indicate that the pH at the droplet centroid is always higher than the bulk (Figure B**.13**).

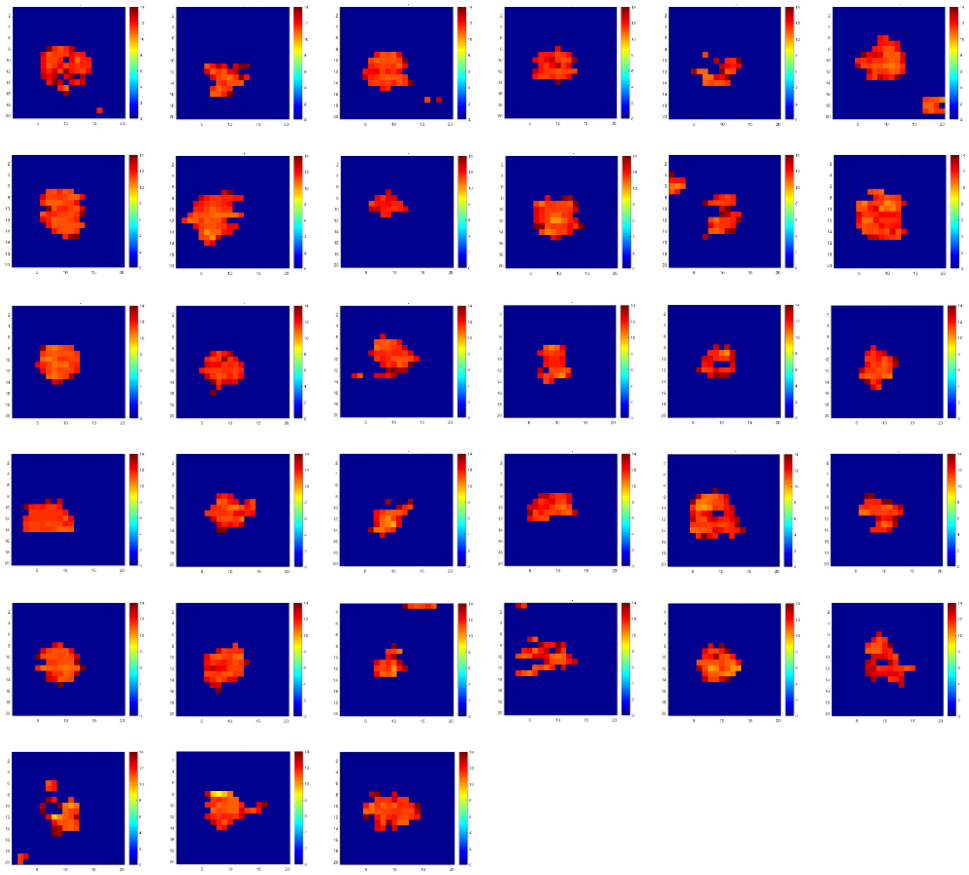

Figure B.11. pH maps of 33 droplets containing 0.6 M PB and pH nanoprobes.

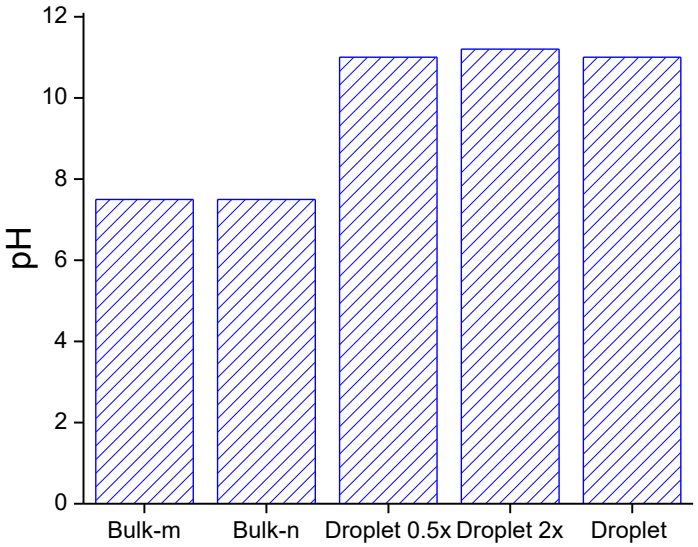

Figure B.12. pH values at the centroid of droplets containing half and twice probe concentrations. Bulk-m: bulk solution pH measured using commercial pH meter; Bulk-n: bulk solution pH measured using pH nanoprobes; Droplet 0.5×: droplet containing half probe concentration; Droplet 2×: droplet containing twice probe concentration.

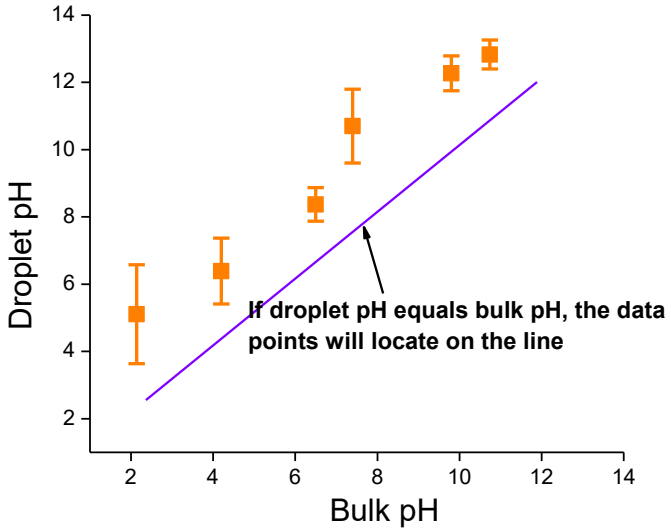

Figure B.13. pH of droplets (in a petri dish without controlling RH) generated from bulk solution with different pH.

An aerosol droplet should be considered a high surface area object with a substantial portion of its volume in the near vicinity of the air/water interface (Figure B.**8**F). The ratio of the interfacial to total volume (Y) as a function of droplet radius (r) can be mathematically expressed as:

$$Y = 1 - \left(\frac{r-a}{r}\right)^3 \qquad \text{Equation B-1}$$

where *a* is the depth relative to the interface. As shown in Figure B**.8**G, *Y* is essentially constant for a droplet radius between 100-1000 μm. However, when the radius is further decreased from 100 to 5 μm (the minimum droplet size studied here), *Y* increases exponentially. For example, in a 60 μm spherical water droplet ($V_{droplet}$ = 1.1 × 10^{-13} m^3) approximately 10% of the total volume is within 1 μm of the surface. For a 10 μm droplet, this percentage increases to 49%. The large air/water interfacial volume could lead to a large number of protons residing at this region, leaving a higher pH zone in the droplet interior. We investigated the relationship between droplet diameter and the pH of the centroid and did not find any correlation (Figure B**.14**). We attribute this fact to the 1) the limited range of droplet diameters (16-25 μm) investigated; and 2) the uncertainty of the height (Z) for the scans. As shown below, the Z exhibits significant influence on droplet pH.

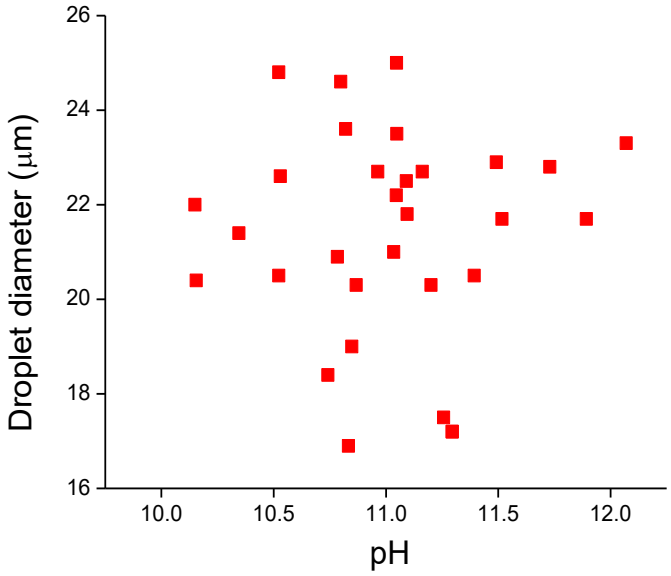

Figure B.14. pH values at the centroid of 31 droplets as a function of droplet diameter**.**

B.3.4 3D pH Distribution

2D scans of a microdroplet (Figure B**.8**B&D) cannot provide information about the pH of the interfacial region. This fact arises from two phenomena: 1) the pH nanoprobes preferentially partition towards the droplet centroid; 2) at the droplet edge the excitation laser is parallel to the air/water interface and thus

relatively few photons can be backscattered by the interfacial region and collected by the detector. This second limitation can be partially overcome by 3D droplet scanning.

As illustrated schematically in Figure B**.15**A, we systematically varied the Z height of the objective both above and below the planar region bisecting the droplet. This approach was first tested by tracking the phosphate band at 998 cm^{-1} for a droplet that did not have nanoprobes added. As shown in Figure B**.16**, the maps get smaller and smaller as the Z height was increased – thus demonstrating the feasibility of 3D scanning of a microdroplet. Subsequently, 3D scans of a droplet containing nanoprobes were collected. As the objective moved upward, the optical images of a droplet (22 μm) became increasingly blurry (Figure B**.15**B). The SERS maps of the droplet exhibit different patterns due to the Brownian motion of the nanoprobes (Figure B**.15**C). As shown in Figure B**.15**E, the pH at the center of each map generally decreased as the objective moved from 0 to 20 μm. This phenomenon was repeatedly observed for a number of different droplets (Figure B**.17**). As the objective moves upward, it gradually approaches the air/water interface. Therefore, the small portion of nanoprobes residing there make an increasingly larger contribution to the SERS signals that are collected, leading to the lower pH values. This observation further supports our speculation that the air/water interface can accumulate protons.

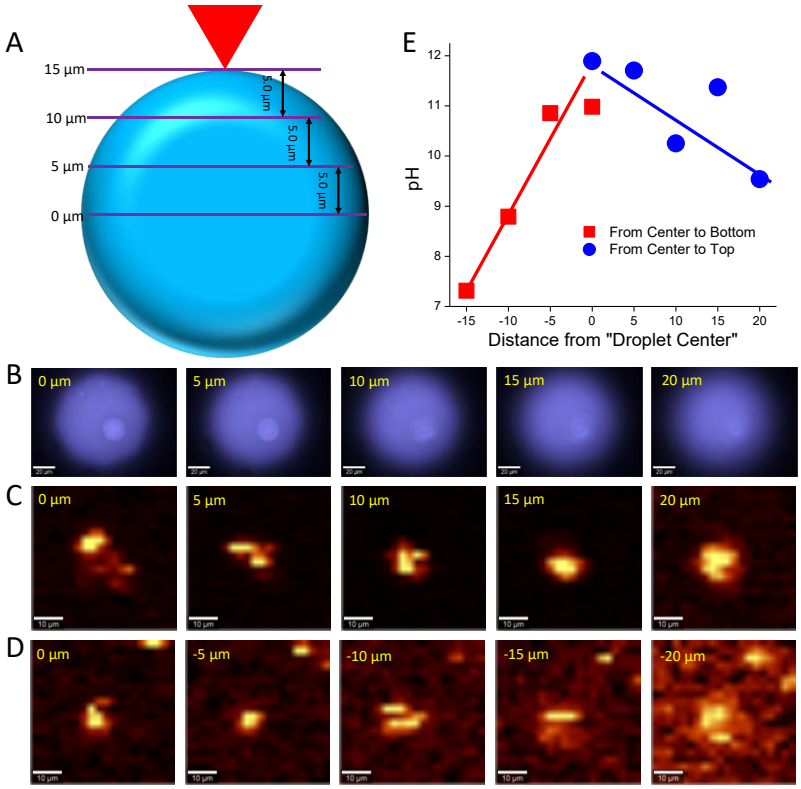

Figure B.15. 3D characterization of the pH inside aerosol droplets. A) Schematic of the 3D scan of the droplet. B) Optical images of droplets containing nanoprobes collected by focusing the light beam at different Z above the middle (0 µm); C) SERS maps of droplets containing nanoprobes collected by focusing the laser beam at different Z above the middle (0 µm); D) SERS maps of droplets containing nanoprobes collected by focusing the laser beam at different Z below the middle (0 µm); E) Variation of pH values at the center of each Raman map as a function of Z.

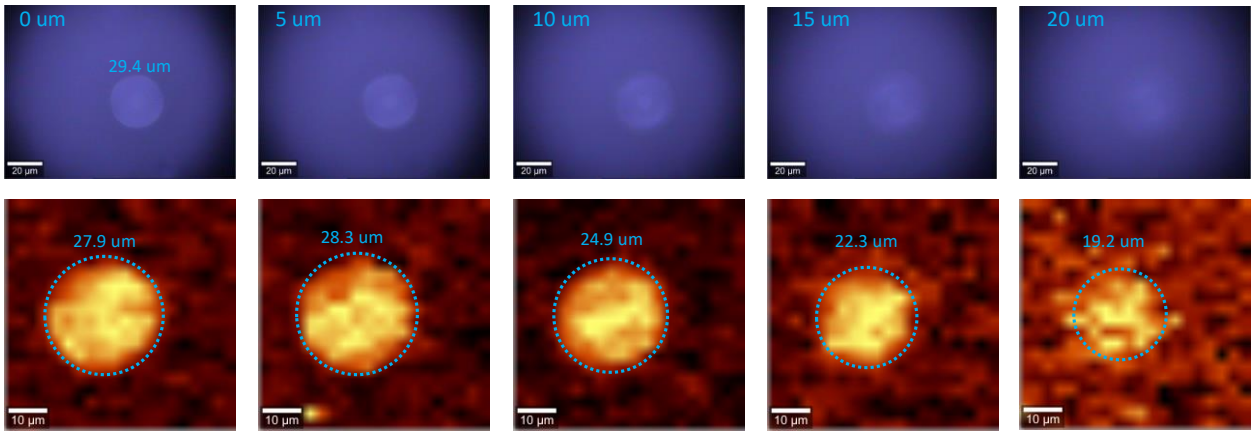

Figure B.16. Variation of optical images and SERS maps (tracking 998 cm^{-1}) collected from the droplet generated from 1M PB solution as a function of Z.

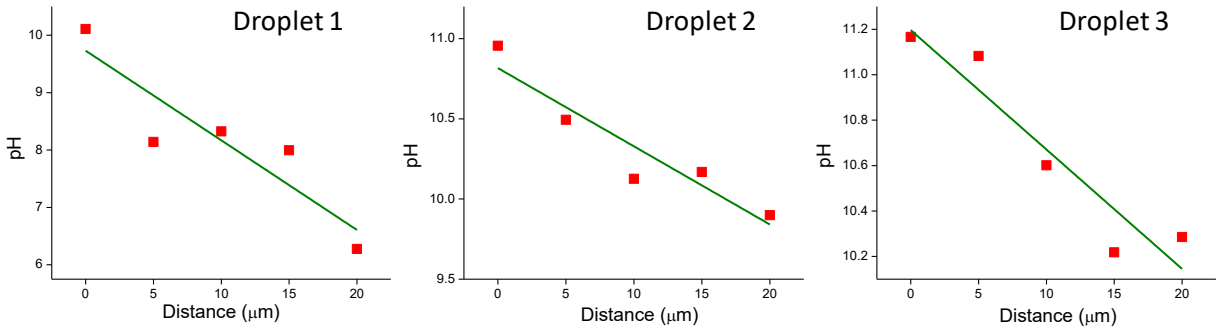

Figure B.17. Variation of pH at the centroid of Raman maps as the objective moved upward.

To further confirm our conclusion, the objective was moved downward from 0 μm and Raman scans were conducted at each Z. As shown in Figure B**.15**D, the contribution of the PVDF substrate to the collected SERS signal gradually increased as the objective was moved towards the droplet bottom, resulting in the deteriorating contrast between the SERS signal and the background signal. Meanwhile, the pH values at the center of each Raman map decreased as the objective moved downward (Figure B**.15**E). The observed differences in the slopes and the pH values at the extremes possibly reflect interactions between the droplet and the hydrophobic substrate. Nonetheless, in each case, the pH at the core of the droplet is substantially different from that at the droplet edge.

B.3.5 Confirmation of Alkaline Droplet pH via Alkaline-Catalyzed Reactions

To confirm the SERS results, we conducted experiments with a different pH indicator (4-ATP). It was recently reported that two 4-ATP molecules co-located within a SERS hot spot dimerize to form dimercaptoazobenzene (DMAB) under alkaline conditions (Figure B**.18**A).[53, 54] We therefore expected that 4-ATP dimerization would be detectable in droplets because of the highly basic pH zone within the droplet core. To test this hypothesis, droplets containing 4-ATP-based nanoprobes were scanned (Figure B**.18**B). As shown in Figure B**.18**, Raman bands at 1138, 1392, and 1432 cm^{-1} that reflect formation of a -N=N- linkage were detected in randomly selected droplets. Using the DMAB Raman band at 1432 cm^{-1} we constructed a SERS map of one droplet and observed consistently strong DMAB signals (Figure B**.18**C). In the control, no DMAB signals were observed within the SERS map of the bulk solution of the same compositions as the droplets (Figure B**.18**D).

The LSPR of AuNPs can release heat through Landau damping and dramatically elevate the temperature (up to 465 K) in the nanoscale vicinity of NPs.[55-57] Halas et al. recently reported that plasmonic nanoparticles with high scattering cross section can localize solar heat within a small volume at the solution surface when the nanoparticle concentration reaches multiple scattering regime[58] and this phenomenon has recently been used to efficiently generate steam without the requirement to boil the whole solution.[55] To exclude the effect of localized heating on this dimerization reaction, bulk solution containing 4-ATP probes was heated in a boiling water bath for 15 min prior to Raman imaging. As shown in Figure B**.18**E, no signal for DMAB was observed in this situation indicating it is the pH rather than the temperature that accelerates the dimerization reaction in droplets. These alkaline catalytic reactions occurring in aerosol droplets generated from neutral bulk solution further indicate that the aerosol droplets are indeed basic.

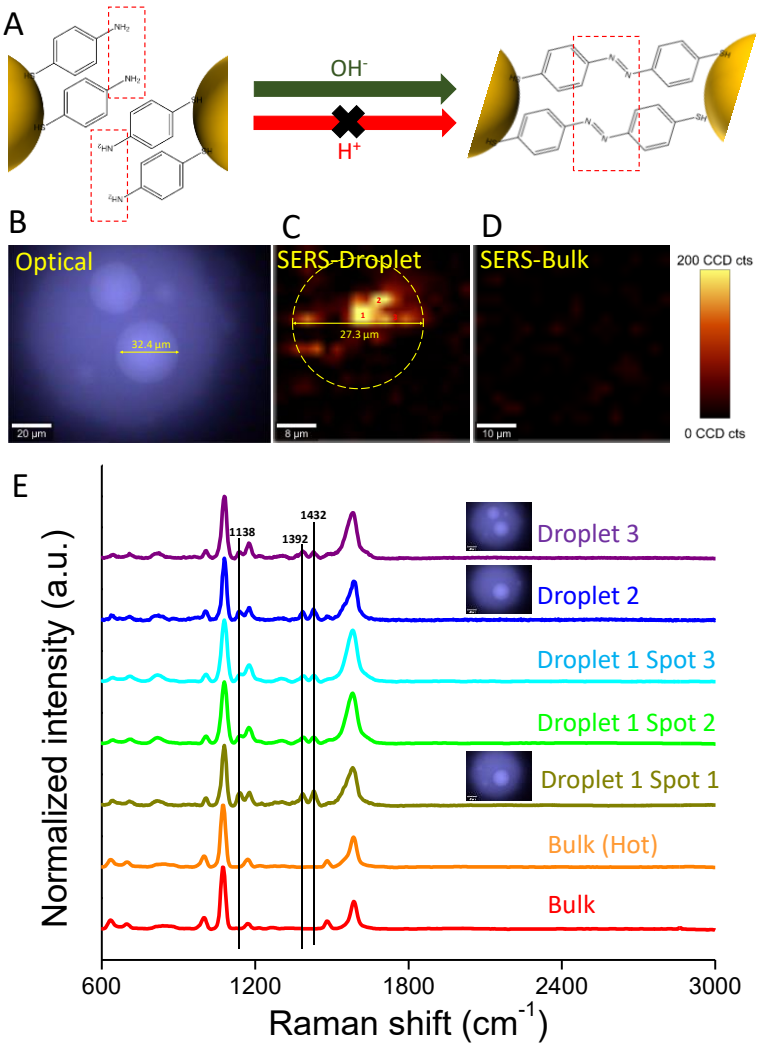

Figure B.18. Basic-catalyzed reaction occurs in droplets generated from neutral bulk solution. A) Schematic for plasmon-catalyzed 4-ATP dimerization enhanced at alkaline conditions; B) Optical image and SERS map of a droplet containing 0.6 M PB solution + 4-ATP-based nanoprobes; C) SERS map of droplet containing 4-ATP-based probes constructed by tracking the DMAB band at 1432 cm^{-1}; D) SERS map of bulk solution containing the same composition as the droplet constructed by tracking the DMAB band at 1432 cm^{-1}; E) SERS spectra of 4-ATP in different spots within one droplet, different droplets, and bulk solutions at room or elevated temperature.

B.4 Discussion

Aqueous aerosols (droplets) are ubiquitous in the atmosphere and are acknowledged for their profound influence on many local-scale and global bio/chemical processes.[1, 12, 59, 60] In this study, we for the first time provide direct experimental evidence that the non-interfacial region of aerosol droplets is more basic than the bulk solution from which they were generated, and we attribute this phenomenon to the preferential accumulation of protons within the interfacial region (Figure B.**8**F). While the underlying physics and

chemistry dictating this behavior are at best only partially understood, two possible explanations are that hydronium preferentially orients such that positively charged protons point towards 'bulk' water, with the electron rich oxygen groups pointing outwards towards the air. Such an orientation is consistent with the apparent negative surface charge of the interface. A second possibility is that localized disruption of the hydrogen-bond network in water stabilizes the Eigencation structure ($H_9O_4^+$) of water at the interface thus leading to enhanced H^+ stability.[27] To add to the confusion, novel theoretical description using the reactive and polarizable LEWIS model of water[61] is consistent with experimental studies that suggest the air/water interface is enhanced in OH^-.[62, 63] The one overriding conclusion that can be reached from all of these, and many other,[64-67] conflicting studies is that the pH of the air/water interface is at present poorly understood. The opposite pH at air/water interfaces reported so far may be a result of the different water chemistry inside aerosol droplets, which calls for more laboratory measurements of droplet pH using advanced *in situ* techniques.[68] Our ongoing work is examining how the water chemistry complexing the pH gradient inside the droplets.

It has been reported that the rate of a number of chemical reactions can be accelerated by up to several orders of magnitude in micrometer-sized droplets (microdroplets) generated by electrospray ionization (ESI).[69-74] The reasons for such uncommon reaction rates are (although not unambiguously known) mostly attributed to the unique air/water interfacial properties of the microdroplets such as high surface-to-volume ratio, altered pH, solvation, and reagent molecule orientation at interfacial region, microdroplet jet fission, and large electrostatic pressure.[70] The last two reasons are artifacts intrinsic to the ESI process. In this study, the microdroplets were generated by an atomizer that excludes the effect of the above-mentioned artifacts, but they nonetheless still exhibit significantly accelerated reaction rates for an alkaline-catalytic reaction. We argue that the proton-hydroxide separation inside the microdroplet induced by air/water interface is the primary cause of this phenomenon.

The acidic water surface and basic water core of aerosol droplets may have a profound influence on atmospheric pollutant uptake, transformation, and aerosol chemistry. Recently, Hung and Hoffmann

reported that SO_2(g) can be oxidized to SO_4^{2-} by O_2 at the acidic air/water interface.[75] The H_2SO_4 produced by this process can be neutralized and can then accumulate within the basic water core that acts as a sink for SO_4^{2-}. Furthermore, the acidic air/water interface is also favorable for NH_3(g) uptake. As the droplet evaporates, both interfacial water and H^+ (in the form of HCl or HNO_3) can transfer to the gaseous phase leaving behind a high concentration of $(NH_4)_2SO_4$ (a major component of Beijing smog) in the aerosol particles. Recently, an unexpectedly high SO_4^{2-} concentration in Beijing smog was observed at high RH in the presence of micrometer-sized droplets. Such a result is consistent with our speculation that the basic droplet core serves as sink for SO_4^{2-}.[76] In multi-phase aerosols containing liquid water, there is even greater potential for steep pH gradients that could have profound effects on SOA formation. Spatial differences in pH within a single aerosol could produce pockets of enhanced or reduced SOA production, as experiments have shown that yields from glyoxal and photooxidation of α-pinene are sensitive to pH.[77, 78] The approach used in this research introduces a new way to probe pH in individual droplets, and the results showing differences in pH between a bulk solution and micron-scale droplets produced from it have important implications not only for atmospheric chemistry but also for biology and other fields where chemical reactions inside droplets drive processes and reactions.

B.5 Materials and Methods

B.5.1 Materials

4-Mercaptobenzoic acid (4-MBA), 4-aminothiophenol (4-ATP), sodium citrate tribasic dehydrate ($Na_3Citrate{\cdot}2H_2O$), gold chloride trihydrate ($HAuCl_4{\cdot}3H_2O$), polyvinylphenol (PVP, molecular weight 10000) and 1 M phosphate buffer (PB, $C_T=[H_3PO_4]+[H_2PO_4^-]+[HPO_4^{2-}]+[PO_4^{3-}]=1M$) were purchased from Sigma-Aldrich. The range of buffer capacities (β) of 1M PB solution is 0.013-0.58 for the pH range 7.2 – 12.3, which is calculated based on Equation B-2 ($\alpha_0=[H_3PO_4]/C_T$, $\alpha_1=[H_2PO_4^-]/C_T$, $\alpha_2=[HPO_4^{2-}]/C_T$, $\alpha_3=[PO_4^{3-}]/C_T$). Thiolated poly(ethylene) glycol (HS-PEG, 5kDa) was purchased from Nanocs. AEROSIL®R202 (fumed silica treated with polydimethylsiloxane, average particle size: 14 nm) was

purchased from Evonik Industries. Polyvinylidene fluoride (PVDF) membrane filters (0.22 μm pore size, 13 mm in diameter) and polytetrafluoroethylene (PTFE) membrane filters (0.1 μm pore size, 13 mm in diameter) were purchased from EMD Millipore.

$$\beta = 2.303([OH^-]+[H^+]+C_T\alpha_0\alpha_1+C_T\alpha_1\alpha_2+C_T\alpha_2\alpha_3) \quad \text{Equation B-2}$$

B.5.2 pH Nanoprobe

The synthesis of the SERS pH nanoprobes is described in our prior publication.[42] Briefly, 500 μL 4-MBA ethanol solution (100 μM) was added to 500 μL AuNP suspension (5×10^{10} NPs/mL). Following vortex mixing, the mixture was kept in room temperature for 120 min and subsequently, 100 μL HS-PEG solution (500 μM) was added into the mixture. The mixture was washed by DI water for three times by centrifugation. 4-ATP-coated AuNPs were synthesized by adding 10 μL 4-ATP in ethanol (1 mM) into 500 μL AuNP suspension followed by 1 min vortex mixing. PVP-coated nanoprobes were synthesized as the following procedure: 500 μL of AuNP suspension and 500 μL of 100 μM 4-MBA ethanol solution are mixed together in a centrifuge tube and vortex for 1 min. After 30 min reaction at room temperature, 100 μL of 500 mM PVP aqueous solution was added. After 1 h reaction at room temperature, the mixture was washed by centrifugation with the same condition as PEG-coated probes.[42]

B.5.3 Generation and Collection of Aerosol Droplets

The method to generate and collect aerosol droplets is illustrated in Figure B**.1**A. In these experiments, 2 mL of probe suspension was added to 3 mL of 1 M PB solution followed by gently mixing. Aerosol droplets were generated by aerosolizing this suspension with a commercial atomizer (TSI 3076, TSI Inc.) that was contained in a custom chamber designed to maintain RH near 100% (Figure B**.19**). Aerosolized droplets were collected on a superhydrophobic filter placed ~1 cm away from the atomizer outlet. The superhydrophobic filter was produced by drop coating 100 μL of AEROSIL in acetone suspension (4 g/L) onto a PVDF filter that was then air dried. Once the aerosolized droplets were collected, the

superhydrophobic filter was sealed in a flow cell that is connected to an automatic humidity controller (Figure B.**20**). Humid air with a relative humidity (RH) of 97±0.5% is generated by the humidity controller and flows through the flow cell to maintain a nearly saturated RH inside the cell. The flow cell was then placed on the sample stage of the Raman spectrometer for analysis.

Figure B.19. Photo of the commercial atomizer contained in a homemade humidity chamber.

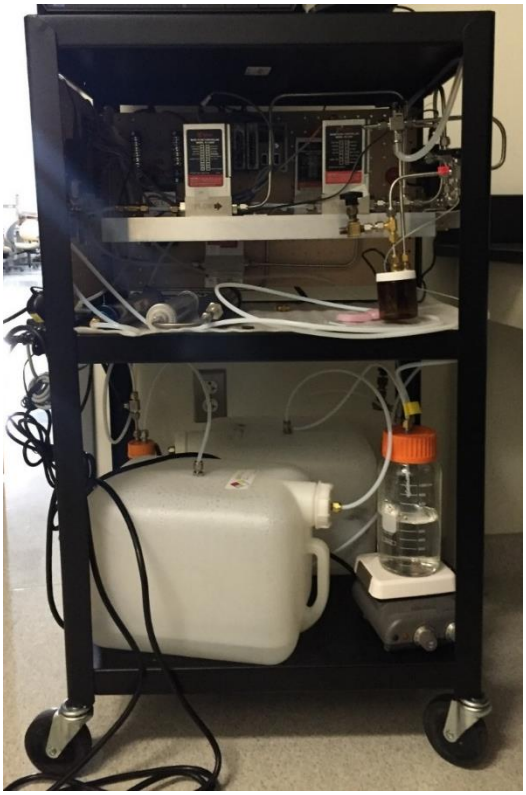

Figure B.20. The photo of the homemade humidity controller**.**

B.5.4 Instrumentation

Single aerosol droplets were scanned by a confocal Raman microscope using a 50× objective (WITec Alpha 500R) and a 785 nm laser. Laser spot size limits the spatial resolution of SERS measurement. In this study, the lateral size of the laser spot is 0.68 μm, the axial size of the laser spot is 3.2 μm, and the excitation volume is 1.5 μm^3. Raman scanning is enabled by a motorized scanning table with a lateral (*X*-*Y*) travel range of 150 × 100 mm and depth (*Z*) travel range of 30 mm with a minimum step size of 0.01 μm. Each collected SERS map consists of 20 × 20 pixels and corresponds to a square area slightly larger than the droplet size. Each pixel represents a single Raman spectrum collected with an integration time of 0.1 s. Bulk solution (0.6 mL) is sealed in a quartz cell (Starna Cells Inc.). The laser is focused at 200 μm below the cell lid and Raman scan is performed with the same parameters as those for the droplets.

B.6 Reference

1. Stevens, B.; Feingold, G., Untangling aerosol effects on clouds and precipitation in a buffered system. *Nature* **2009,** *461*, (7264), 607-613.
2. Husar, R. B.; White, W. H.; Blumenthal, D. L., Direct evidence of heterogeneous aerosol formation in Los Angeles smog. *Environ. Sci. Technol.* **1976,** *10*, (5), 490-491.
3. King, M. D.; Thompson, K. C.; Ward, A. D., Laser tweezers Raman study of optically trapped aerosol droplets of seawater and oleic acid reacting with ozone: implications for cloud-droplet properties. *J. Am. Chem. Soc.* **2004,** *126*, (51), 16710-16711.
4. Ariya, P. A.; Amyot, M.; Dastoor, A.; Deeds, D.; Feinberg, A.; Kos, G.; Poulain, A.; Ryjkov, A.; Semeniuk, K.; Subir, M., Mercury physicochemical and biogeochemical transformation in the atmosphere and at atmospheric interfaces: A review and future directions. *Chem. Rev.* **2015,** *115*, (10), 3760-3802.
5. Von Schneidemesser, E.; Monks, P. S.; Allan, J. D.; Bruhwiler, L.; Forster, P.; Fowler, D.; Lauer, A.; Morgan, W. T.; Paasonen, P.; Righi, M., Chemistry and the linkages between air quality and climate change. *Chem. Rev* **2015,** *115*, (10), 3856-3897.
6. Bian, Y.; Zhao, C.; Ma, N.; Chen, J.; Xu, W., A study of aerosol liquid water content based on hygroscopicity measurements at high relative humidity in the North China Plain. *Atmos. Chem. Phys* **2014,** *14*, (12), 6417-6426.
7. Kreidenweis, S.; Petters, M.; DeMott, P., Single-parameter estimates of aerosol water content. *Environ. Res. Lett.* **2008,** *3*, (3), 035002.
8. Lohmann, U.; Feichter, J., Global indirect aerosol effects: a review. *Atmos. Chem. Phys* **2005,** *5*, (3), 715-737.
9. Christensen, M. W.; Neubauer, D.; Poulsen, C. A.; Thomas, G. E.; McGarragh, G. R.; Povey, A. C.; Proud, S. R.; Grainger, R. G., Unveiling aerosol–cloud interactions–Part 1: Cloud contamination in satellite products enhances the aerosol indirect forcing estimate. *Atmos. Chem. Phys* **2017,** *17*, (21), 13151-13164.
10. Ault, A. P.; Zhao, D.; Ebben, C. J.; Tauber, M. J.; Geiger, F. M.; Prather, K. A.; Grassian, V. H., Raman microspectroscopy and vibrational sum frequency generation spectroscopy as probes of the bulk and surface compositions of size-resolved sea spray aerosol particles. *Phys. Chem. Chem. Phys.* **2013,** *15*, (17), 6206-6214.
11. Herrmann, H.; Schaefer, T.; Tilgner, A.; Styler, S. A.; Weller, C.; Teich, M.; Otto, T., Tropospheric aqueous-phase chemistry: kinetics, mechanisms, and its coupling to a changing gas phase. *Chem. Rev.* **2015,** *115*, (10), 4259-4334.
12. Pöschl, U.; Shiraiwa, M., Multiphase chemistry at the atmosphere–biosphere interface influencing climate and public health in the Anthropocene. *Chem. Rev.* **2015,** *115*, (10), 4440-4475.
13. Lin, Y.-H.; Zhang, Z.; Docherty, K. S.; Zhang, H.; Budisulistiorini, S. H.; Rubitschun, C. L.; Shaw, S. L.; Knipping, E. M.; Edgerton, E. S.; Kleindienst, T. E., Isoprene epoxydiols as precursors to secondary organic aerosol formation: acid-catalyzed reactive uptake studies with authentic compounds. *Environ. Sci. Technol.* **2011,** *46*, (1), 250-258.
14. Li, Y. J.; Cheong, G. Y.; Lau, A. P.; Chan, C. K., Acid-catalyzed condensed-phase reactions of limonene and terpineol and their impacts on gas-to-particle partitioning in the formation of organic aerosols. *Environ. Sci. Technol.* **2010,** *44*, (14), 5483-5489.
15. Zhang, H.; Zhang, Z.; Cui, T.; Lin, Y.-H.; Bhathela, N. A.; Ortega, J.; Worton, D. R.; Goldstein, A. H.; Guenther, A.; Jimenez, J. L., Secondary organic aerosol formation via 2-methyl-3-buten-2-ol photooxidation: evidence of acid-catalyzed reactive uptake of epoxides. *Environ Sci Technol Lett.* **2014,** *1*, (4), 242-247.
16. Schwarzenbach, R. P.; Gschwend, P. M.; Imboden, D. M., *Environmental organic chemistry*. John Wiley & Sons: 2005.

17. Weber, R. J.; Guo, H.; Russell, A. G.; Nenes, A., High aerosol acidity despite declining atmospheric sulfate concentrations over the past 15 years. *Nat. Geosci.* **2016,** *9*, (4), 282-285.
18. Guo, H.; Xu, L.; Bougiatioti, A.; Cerully, K. M.; Capps, S. L.; Hite Jr, J.; Carlton, A.; Lee, S.; Bergin, M.; Ng, N., Fine-particle water and pH in the southeastern United States. *Atmos. Chem. Phys* **2015,** *15*, (9), 5211-5228.
19. Dallemagne, M. A.; Huang, X. Y.; Eddingsaas, N. C., Variation in pH of Model Secondary Organic Aerosol during Liquid–Liquid Phase Separation. *J. Phys. Chem. A* **2016,** *120*, (18), 2868-2876.
20. Losey, D. J.; Parker, R. G.; Freedman, M. A., pH Dependence of Liquid-Liquid Phase Separation in Organic Aerosol. *J. Phys. Chem. Lett.* **2016**.
21. Boyer, H. C.; Dutcher, C. S., Atmospheric Aqueous Aerosol Surface Tensions: Isotherm-Based Modeling and Biphasic Microfluidic Measurements. *J. Phys. Chem. A* **2017,** *121*, (25), 4733-4742.
22. Boyer, H. C.; Bzdek, B. R.; Reid, J. P.; Dutcher, C. S., Statistical Thermodynamic Model for Surface Tension of Organic and Inorganic Aqueous Mixtures. *J. Phys. Chem. A* **2016,** *121*, (1), 198-205.
23. Ault, A. P.; Axson, J. L., Atmospheric Aerosol Chemistry: Spectroscopic and Microscopic Advances. *Anal. Chem.* **2016,** *89*, (1), 430-452.
24. Agmon, N.; Bakker, H. J.; Campen, R. K.; Henchman, R. H.; Pohl, P.; Roke, S.; Thamer, M.; Hassanali, A., Protons and Hydroxide Ions in Aqueous Systems. *Chem. Rev.* **2016,** *116*, (13), 7642-7672.
25. Saykally, R. J., Air/water interface: Two sides of the acid-base story. *Nat. Chem.* **2013,** *5*, (2), 82-84.
26. Duignan, T. T.; Parsons, D. F.; Ninham, B. W., Hydronium and hydroxide at the air-water interface with a continuum solvent model. *Chem. Phys. Lett.* **2015,** *635*, 1-12.
27. Tse, Y.-L. S.; Chen, C.; Lindberg, G. E.; Kumar, R.; Voth, G. A., Propensity of Hydrated Excess Protons and Hydroxide Anions for the Air–Water Interface. *J. Am. Chem. Soc.* **2015,** *137*, (39), 12610-12616.
28. Vácha, R.; Horinek, D.; Berkowitz, M. L.; Jungwirth, P., Hydronium and hydroxide at the interface between water and hydrophobic media. *Phys. Chem. Chem. Phys.* **2008,** *10*, (32), 4975-4980.
29. Shi, G.-l.; Xu, J.; Peng, X.; Xiao, Z.; Chen, K.; Tian, Y.; Guan, X.; Feng, Y.; Yu, H.; Nenes, A., pH of Aerosols in a Polluted Atmosphere: Source Contributions to Highly Acidic Aerosol. *Environ. Sci. Technol.* **2017**.
30. Murphy, J. G.; Gregoire, P.; Tevlin, A.; Wentworth, G.; Ellis, R.; Markovic, M.; VandenBoer, T., Observational constraints on particle acidity using measurements and modelling of particles and gases. *Faraday Discuss.* **2017**.
31. Nguyen, T. K. V.; Zhang, Q.; Jimenez, J. L.; Pike, M.; Carlton, A. G., Liquid water: Ubiquitous contributor to aerosol mass. *Environ Sci Technol Lett.* **2016,** *3*, (7), 257-263.
32. Rindelaub, J. D.; Craig, R. L.; Nandy, L.; Bondy, A. L.; Dutcher, C. S.; Shepson, P. B.; Ault, A. P., Direct Measurement of pH in Individual Particles via Raman Microspectroscopy and Variation in Acidity with Relative Humidity. *J. Phys. Chem. A* **2016,** *120*, (6), 911-917.
33. Craig, R. L.; Bondy, A. L.; Ault, A. P., Surface enhanced Raman spectroscopy enables observations of previously undetectable secondary organic aerosol components at the individual particle level. *Anal. Chem* **2015,** *87*, (15), 7510-7514.
34. Fu, Y.; Kuppe, C.; Valev, V. K.; Fu, H.; Zhang, L.; Chen, J., Surface-Enhanced Raman Spectroscopy: A Facile and Rapid Method for the Chemical Component Study of Individual Atmospheric Aerosol. *Environ. Sci. Technol* **2017,** *51*, (11), 6260-6267.
35. Kneipp, K.; Wang, Y.; Kneipp, H.; Perelman, L. T.; Itzkan, I.; Dasari, R. R.; Feld, M. S., Single molecule detection using surface-enhanced Raman scattering (SERS). *Physical review letters* **1997,** *78*, (9), 1667.
36. Etchegoin, P. G.; Le Ru, E., A perspective on single molecule SERS: current status and future challenges. *Phys. Chem. Chem. Phys.* **2008,** *10*, (40), 6079-6089.
37. Xu, H.; Bjerneld, E. J.; Käll, M.; Börjesson, L., Spectroscopy of single hemoglobin molecules by surface enhanced Raman scattering. *Phys. Rev. Lett.* **1999,** *83*, (21), 4357.

38. Le Ru, E. C.; Meyer, M.; Etchegoin, P. G., Proof of single-molecule sensitivity in surface enhanced Raman scattering (SERS) by means of a two-analyte technique. *J. Phys. Chem. B* **2006,** *110*, (4), 1944-1948.
39. Kneipp, J.; Kneipp, H.; Wittig, B.; Kneipp, K., One-and two-photon excited optical pH probing for cells using surface-enhanced Raman and hyper-Raman nanosensors. *Nano Lett.* **2007,** *7*, (9), 2819-2823.
40. Pallaoro, A.; Braun, G. B.; Reich, N.; Moskovits, M., Mapping local pH in live cells using encapsulated fluorescent SERS nanotags. *Small* **2010,** *6*, (5), 618-622.
41. Colussi, A. J.; Enami, S.; Yabushita, A.; Hoffmann, M. R.; Liu, W.-G.; Mishra, H.; Goddard III, W. A., Tropospheric aerosol as a reactive intermediate. *Faraday Discuss.* **2013,** *165*, 407-420.
42. Wei, H.; Willner, M. R.; Marr, L. C.; Vikesland, P. J., Highly stable SERS pH nanoprobes produced by co-solvent controlled AuNP aggregation. *Analyst* **2016**.
43. Myriokefalitakis, S.; Nenes, A.; Baker, A. R.; Mihalopoulos, N.; Kanakidou, M., Bioavailable atmospheric phosphorous supply to the global ocean: a 3-D global modeling study. *Biogeosciences* **2016,** *13*, (24), 6519.
44. Anderson, L.; Faul, K.; Paytan, A., Phosphorus associations in aerosols: What can they tell us about P bioavailability? *Mar. Chem.* **2010,** *120*, (1), 44-56.
45. Longo, A. F.; Ingall, E. D.; Diaz, J. M.; Oakes, M.; King, L. E.; Nenes, A.; Mihalopoulos, N.; Violaki, K.; Avila, A.; Benitez-Nelson, C. R., P-NEXFS analysis of aerosol phosphorus delivered to the Mediterranean Sea. *Geophys. Res. Lett.* **2014,** *41*, (11), 4043-4049.
46. Bishnoi, S. W.; Rozell, C. J.; Levin, C. S.; Gheith, M. K.; Johnson, B. R.; Johnson, D. H.; Halas, N. J., All-optical nanoscale pH meter. *Nano Lett.* **2006,** *6*, (8), 1687-1692.
47. Liu, Y.; Yuan, H.; Fales, A. M.; Vo-Dinh, T., pH-sensing nanostar probe using surface-enhanced Raman scattering (SERS): theoretical and experimental studies. *J. Raman Spectrosc.* **2013,** *44*, (7), 980-986.
48. Mandair, G. S.; Morris, M. D., Contributions of Raman spectroscopy to the understanding of bone strength. *Bonekey Rep.* **2015,** *4*.
49. Michota, A.; Bukowska, J., Surface-enhanced Raman scattering (SERS) of 4-mercaptobenzoic acid on silver and gold substrates. *J. Raman Spectrosc.* **2003,** *34*, (1), 21-25.
50. McCaffrey, D. L.; Nguyen, S. C.; Cox, S. J.; Weller, H.; Alivisatos, A. P.; Geissler, P. L.; Saykally, R. J., Mechanism of ion adsorption to aqueous interfaces: Graphene/water vs. air/water. *Proc. Natl. Acad. Sci. U.S.A.* **2017**, 201702760.
51. Campioni, S.; Carret, G.; Jordens, S.; Nicoud, L. c.; Mezzenga, R.; Riek, R., The presence of an air–water interface affects formation and elongation of α-synuclein fibrils. *J. Am. Chem. Soc.* **2014,** *136*, (7), 2866-2875.
52. Guo, X.; Yin, Y.; Tan, Z.; Zhang, Z.; Chen, Y.; Liu, J., Significant Enrichment of Engineered Nanoparticles in Water Surface Microlayer. *Environ Sci Technol Lett.* **2016,** *3*, (10), 381-385.
53. Gabudean, A.; Biro, D.; Astilean, S., Localized surface plasmon resonance (LSPR) and surface-enhanced Raman scattering (SERS) studies of 4-aminothiophenol adsorption on gold nanorods. *J. Mol. Struct.* **2011,** *993*, (1), 420-424.
54. Sun, M.; Huang, Y.; Xia, L.; Chen, X.; Xu, H., The pH-controlled plasmon-assisted surface photocatalysis reaction of 4-aminothiophenol to p, p′-dimercaptoazobenzene on Au, Ag, and Cu colloids. *J. Phys. Chem. C* **2011,** *115*, (19), 9629-9636.
55. Neumann, O.; Urban, A. S.; Day, J.; Lal, S.; Nordlander, P.; Halas, N. J., Solar vapor generation enabled by nanoparticles. *ACS Nano* **2012,** *7*, (1), 42-49.
56. Govorov, A. O.; Richardson, H. H., Generating heat with metal nanoparticles. *Nano Today* **2007,** *2*, (1), 30-38.
57. Fang, Z.; Zhen, Y.-R.; Neumann, O.; Polman, A.; García de Abajo, F. J.; Nordlander, P.; Halas, N. J., Evolution of light-induced vapor generation at a liquid-immersed metallic nanoparticle. *Nano Lett.* **2013,** *13*, (4), 1736-1742.

58. Hogan, N. J.; Urban, A. S.; Ayala-Orozco, C.; Pimpinelli, A.; Nordlander, P.; Halas, N. J., Nanoparticles heat through light localization. *Nano Lett.* **2014,** *14*, (8), 4640-4645.
59. Seinfeld, J. H.; Pandis, S. N., *Atmospheric chemistry and physics: from air pollution to climate change*. John Wiley & Sons: 2016.
60. Milton, D. K.; Fabian, M. P.; Cowling, B. J.; Grantham, M. L.; McDevitt, J. J., Influenza virus aerosols in human exhaled breath: particle size, culturability, and effect of surgical masks. *PLoS Pathog.* **2013,** *9*, (3), e1003205.
61. Bai, C.; Herzfeld, J., Surface Propensities of the Self-Ions of Water. *ACS Cent. Sci.* **2016,** *2*, (4), 225-231.
62. Mishra, H.; Enami, S.; Nielsen, R. J.; Stewart, L. A.; Hoffmann, M. R.; Goddard, W. A.; Colussi, A. J., Brønsted basicity of the air–water interface. *Proc. Natl. Acad. Sci. U.S.A.* **2012,** *109*, (46), 18679-18683.
63. Enami, S.; Hoffmann, M. R.; Colussi, A. J., Proton availability at the air/water interface. *J. Phys. Chem. Lett.* **2010,** *1*, (10), 1599-1604.
64. Baer, M. D.; Kuo, I. F. W.; Tobias, D. J.; Mundy, C. J., Toward a Unified Picture of the Water Self-Ions at the Air-Water Interface: A Density Functional Theory Perspective. *J. Phys. Chem. B* **2014,** *118*, (28), 8364-8372.
65. Beattie, J. K.; Djerdjev, A. M.; Gray-Weale, A.; Kallay, N.; Lutzenkirchen, J.; Preocanin, T.; Selmani, A., pH and the surface tension of water. *J. Colloid Interface Sci.* **2014,** *422*, 54-57.
66. Bjornehohn, E.; Hansen, M. H.; Hodgson, A.; Liu, L. M.; Limmer, D. T.; Michaelides, A.; Pedevilla, P.; Rossmeisl, J.; Shen, H.; Tocci, G.; Tyrode, E.; Walz, M. M.; Werner, J.; Bluhm, H., Water at Interfaces. *Chem. Rev.* **2016,** *116*, (13), 7698-7726.
67. Hub, J. S.; Wolf, M. G.; Caleman, C.; Maaren, P. J.; Groenhof, G.; van der Spoel, D., Thermodynamics of hydronium and hydroxide surface solvation. *Chem. Sci.* **2014,** *5*, (5), 1745-1749.
68. Marsh, A.; Rovelli, G.; Song, Y.-C.; Pereira, K. L.; Willoughby, R. E.; Bzdek, B. R.; Hamilton, J.; Orr-Ewing, A.; Topping, D. O.; Reid, J. P., Accurate representations of the physicochemical properties of atmospheric aerosols: when are laboratory measurements of value? *Faraday Discuss.* **2017**.
69. Lee, J. K.; Kim, S.; Nam, H. G.; Zare, R. N., Microdroplet fusion mass spectrometry for fast reaction kinetics. *Proc. Natl. Acad. Sci. U.S.A.* **2015,** *112*, (13), 3898-3903.
70. Banerjee, S.; Gnanamani, E.; Yan, X.; Zare, R. N., Can all bulk-phase reactions be accelerated in microdroplets? *Analyst* **2017**.
71. Müller, T.; Badu-Tawiah, A.; Cooks, R. G., Accelerated Carbon□ Carbon Bond-Forming Reactions in Preparative Electrospray. *Angew. Chem. Int. Ed.* **2012,** *51*, (47), 11832-11835.
72. Girod, M.; Moyano, E.; Campbell, D. I.; Cooks, R. G., Accelerated bimolecular reactions in microdroplets studied by desorption electrospray ionization mass spectrometry. *Chem. Sci.* **2011,** *2*, (3), 501-510.
73. Fallah-Araghi, A.; Meguellati, K.; Baret, J.-C.; El Harrak, A.; Mangeat, T.; Karplus, M.; Ladame, S.; Marques, C. M.; Griffiths, A. D., Enhanced chemical synthesis at soft interfaces: A universal reaction-adsorption mechanism in microcompartments. *Phys. Rev. Lett.* **2014,** *112*, (2), 028301.
74. Bain, R. M.; Pulliam, C. J.; Cooks, R. G., Accelerated Hantzsch electrospray synthesis with temporal control of reaction intermediates. *Chem. Sci.* **2015,** *6*, (1), 397-401.
75. Hung, H.-M.; Hoffmann, M. R., Oxidation of Gas-Phase SO2 on the Surfaces of Acidic Microdroplets: Implications for Sulfate and Sulfate Radical Anion Formation in the Atmospheric Liquid Phase. *Environ. Sci. Technol.* **2015,** *49*, (23), 13768-13776.
76. Wang, G.; Zhang, R.; Gomez, M. E.; Yang, L.; Zamora, M. L.; Hu, M.; Lin, Y.; Peng, J.; Guo, S.; Meng, J., Persistent sulfate formation from London Fog to Chinese haze. *Proc. Natl. Acad. Sci. U.S.A.* **2016,** *113*, (48), 13630-13635.
77. Ortiz-Montalvo, D. L.; Häkkinen, S. A.; Schwier, A. N.; Lim, Y. B.; McNeill, V. F.; Turpin, B. J., Ammonium addition (and aerosol pH) has a dramatic impact on the volatility and yield of glyoxal secondary organic aerosol. *Environ. Sci. Technol.* **2013,** *48*, (1), 255-262.

78. Han, Y.; Stroud, C. A.; Liggio, J.; Li, S.-M., The effect of particle acidity on secondary organic aerosol formation from α-pinene photooxidation under atmospherically relevant conditions. *Atmos. Chem. Phys* **2016,** *16*, (21), 13929-13944.